

# Contents

<b>I</b>	<b>The Standard Model and its supersymmetric extensions</b>	<b>1</b>
<b>I.1</b>	<b>The Standard Model of particle physics</b>	<b>3</b>
I.1.1	The particle content . . . . .	3
I.1.2	The Lagrangian density . . . . .	4
I.1.3	The Brout-Englert-Higgs mechanism . . . . .	6
I.1.4	Limitations of the Standard Model . . . . .	8
<b>I.2</b>	<b>Supersymmetry</b>	<b>9</b>
I.2.1	The MSSM . . . . .	12
I.2.1.1	The particle content of the MSSM . . . . .	13
I.2.1.2	The Lagrangian density of the MSSM . . . . .	13
I.2.1.3	The phenomenological MSSM . . . . .	15
I.2.2	Supersymmetry breaking . . . . .	15
<b>I.3</b>	<b>Long-lived particles in the MSSM</b>	<b>16</b>
I.3.1	Previous searches for long-lived charged particles . . . . .	16
<b>II</b>	<b>Measurement of the jet transverse-momentum resolution</b>	<b>17</b>
<b>II.1</b>	<b>Introduction</b>	<b>19</b>
<b>II.2</b>	<b>General approach of the resolution measurement using photon+jet events</b>	<b>19</b>
<b>II.3</b>	<b>Datasets and event selection</b>	<b>22</b>
II.3.1	Datasets and triggers . . . . .	23
II.3.2	Simulated samples . . . . .	24
II.3.3	Event selection . . . . .	25
II.3.3.1	Jet selection . . . . .	25
II.3.3.2	Photon selection . . . . .	26
II.3.3.3	Photon+jet event selection . . . . .	27
<b>II.4</b>	<b>Methodology of the measurement</b>	<b>28</b>

27	II.4.1	Validation of the method . . . . .	35
28	<b>II.5</b>	<b>Systematic uncertainties</b>	<b>38</b>
29	<b>II.6</b>	<b>Results</b>	<b>43</b>
30	II.6.1	Comparison to 2011 measurement . . . . .	45
31	II.6.2	Comparison to 2012 dijet measurement . . . . .	47
32	<b>II.7</b>	<b>Discussion and conclusion</b>	<b>48</b>
33	<b>III</b>	<b>A search for highly ionising, short tracks at the CMS detector</b>	<b>51</b>
34	<b>III.1</b>	<b>Motivation</b>	<b>53</b>
35	<b>III.2</b>	<b>General search strategy</b>	<b>55</b>
36	III.2.1	Comparison to earlier searches . . . . .	60
37	<b>III.3</b>	<b>Improved dE/dx measurement for short tracks</b>	<b>63</b>
38	III.3.1	Estimation of the ionisation loss of charged particles . . . . .	63
39	III.3.2	Energy calibration of the silicon pixel tracker . . . . .	66
40	III.3.3	Discrimination of highly-ionising particles . . . . .	71
41	III.3.4	Discrimination improvements . . . . .	72
42	<b>III.4</b>	<b>Simulated samples</b>	<b>76</b>
43	III.4.1	Standard Model background samples . . . . .	76
44	III.4.2	Signal samples . . . . .	77
45	<b>III.5</b>	<b>Event selection</b>	<b>79</b>
46	III.5.1	Datasets and triggers . . . . .	79
47	III.5.2	Selection of signal candidate events . . . . .	81
48	III.5.2.1	Event-based selection . . . . .	81
49	III.5.2.2	Candidate track selection . . . . .	83
50	<b>III.6</b>	<b>Characterisation and estimation of the Standard Model backgrounds</b>	<b>93</b>
51	III.6.1	Fake background . . . . .	94
52	III.6.1.1	Inclusive fake background estimation . . . . .	95
53	III.6.1.2	dE/dx shape of fake background . . . . .	100
54	III.6.2	Leptonic background . . . . .	102
55	III.6.2.1	Inclusive leptonic background estimation . . . . .	105
56	III.6.2.2	dE/dx shape of leptonic background . . . . .	107
57	III.6.3	Background estimation validation . . . . .	108

58	III.6.4	Systematic uncertainties . . . . .	109
59	III.6.4.1	Uncertainty on the fake rate . . . . .	110
60	III.6.4.2	Uncertainty on the $dE/dx$ shape of fake tracks . . . . .	110
61	III.6.4.3	Uncertainty on the leptonic scale factor . . . . .	112
62	III.6.4.4	Uncertainty on the leptonic $dE/dx$ shape . . . . .	113
63	<b>III.7</b>	<b>Optimisation of the search sensitivity</b>	<b>113</b>
64	<b>III.8</b>	<b>Results</b>	<b>117</b>
65	<b>III.9</b>	<b>Interpretation</b>	<b>119</b>
66	III.9.1	Systematic uncertainties of simulated signal samples . . . . .	119
67	III.9.2	Statistical Methods/ Limit setting . . . . .	125
68	III.9.3	Exclusion limits . . . . .	128
69	III.9.4	Comparison to the search for disappearing tracks . . . . .	131
70	<b>III.10</b>	<b>Conclusion and outlook</b>	<b>132</b>



71

## **Part I**

72

# **The Standard Model and its supersymmetric extensions**

73



## I.1 The Standard Model of particle physics

The formulation of a relativistic quantum field theory and of spontaneous symmetry breaking (SSB) by the Brout-Englert-Higgs mechanism, allowed to built a theory which is capable to explain almost all observations of particle physics until today [1]. This theory is known as the Standard Model of particle physics (SM). The existence of its last missing piece, the Higgs boson, could be proven at the LHC in the year 2012 [2, 3].

The Standard Model is a  $SU(3)_C \times SU(2)_L \times SU(1)_Y$  non-abelian gauge theory. “After” spontaneous symmetry breaking, its symmetries are reduced to  $SU(3)_C \times U(1)_{EM}$ . All particles that were found until today are contained in it<sup>1</sup>. Furthermore, it is able to describe three of the four fundamental forces: the strong, weak and electromagnetic force.

In the following, a small introduction to the theory and phenomenology of the Standard Model is given. It is not meant as a complete description. The reader is referred to [4–6], for a thorough and extensive introduction.

### I.1.1 The particle content

It should be first noted, since the Standard Model is a quantum field theory, every field (to be more precise every degree of freedom of a field) can be considered also as a particle and vice versa.

The Standard Model of particle physics contains three different particle types, or three different types of fields. First, there are the so-called “matter particles”, which are all spin 1/2 particles in the SM. Second, the forces are described by spin 1 vector bosons. And finally, in order to give masses to all particles the Standard Model embeds the Higgs boson, a scalar spin 0 particle.

### Fermions in the Standard Model

The fermionic content can be further subdivided into leptons and quarks. In contrast to quarks, leptons are not strongly interacting, thus they only couple electromagnetically and weakly to other particles. Both, the quarks and the leptons are ordered into three different families. Across these families, all quantum numbers are conserved. They only differ by their mass.

---

<sup>1</sup>One can argue, that the right-handed neutrino, which is proven to exist, is not contained. But as at least the left-handed neutrino is embedded, we want to ignore that for a moment.

102 All left-handed particles of each family form a  $SU(2)_L$  doublet, which causes the coupling  
 103 via the weak force. The right-handed partners form  $SU(2)$  singlets, thus, don't couple via  
 104 the weak interaction. As quarks carry one further quantum number, the colour, they are  
 105 additionally grouped into  $SU(3)_C$  triplets.

## 106 Vector bosons in the Standard Model

107 As mentioned before, the vector bosons describe three of the four fundamental forces.  
 108 There is one gauge boson corresponding to every generator of the above mentioned gauge  
 109 groups. For  $U(1)_Y$ , it is the  $B$ -boson, for  $SU(2)_L$ , there are three gauge bosons  $W^{1,2,3}$   
 110 and finally eight gauge bosons  $G^{1\dots 8}$  for  $SU(3)_C$ , which are called gluons. As the  $B$ -field  
 111 and the neutral  $W_\mu^3$ -field can mix, "after" SSB the basis can be changed and lead to the  
 112 well known photon and  $Z$ -boson.

## 113 The Higgs boson

114 A somehow extraordinary role plays the Higgs boson, that was predicted already 50 years  
 115 ago by Peter Higgs [7, 8] and could be proven existent by the LHC experiments CMS and  
 116 Atlas in 2012 [2, 3]. This particle is a consequence of the spontaneous symmetry breaking  
 117 after rotating three of the four degrees of freedom to masses of the  $W$ -and  $Z$ -bosons. It is  
 118 the only known fundamental scalar particle.

119  
 120 An overview of all Standard Model particles and their transformation properties are  
 121 shown in Table I.1.1. If particles transform as singlets under  $SU(2)_L$  or  $SU(3)_C$ , they don't  
 122 couple via the corresponding force. The hypercharges  $Y$  are determined by  $Q = Y + I_3$ ,  
 123 where  $Q$  is the electric charge and  $I_3$  is the third component of the weak isospin with  
 124  $I^a = \sigma^a/2$ ,  $\sigma^a$  being the Pauli matrices.

## 125 I.1.2 The Lagrangian density

126 In particle physics, the probability of a decay or an interaction between particles can  
 127 be calculated with the help of the Lagrangian density. The Lagrangian density of the  
 128 Standard Model is the most general set of Lagrangian terms, that are renormalisable and  
 129 contain all up to date known particles as well as the above mentioned gauge symmetries.



Table I.1.1: All particles contained in the Standard Model and their transformation properties under  $SU(3)_C \times SU(2)_L \times SU(1)_Y$ .

	$SU(3)_C$	$SU(2)_L$	$U(1)_Y$
Fermions:			
$(\nu_L, e_L)^T$	<b>1</b>	<b>2</b>	-1
$e_R$	<b>1</b>	<b>1</b>	-2
$(u_L, d_L)^T$	<b>3</b>	<b>2</b>	$+\frac{1}{3}$
$u_R$	<b>3</b>	<b>1</b>	$+\frac{4}{3}$
$d_R$	<b>3</b>	<b>1</b>	$-\frac{2}{3}$
Vector bosons:			
$B_\mu$	<b>1</b>	<b>1</b>	0
$W_\mu^a$	<b>1</b>	<b>3</b>	0
$G_\mu^a$	<b>8</b>	<b>1</b>	0
Higgs boson: $H$	<b>1</b>	<b>2</b>	-1

130 It is the following:

$$\begin{aligned}
\mathcal{L} = & (D_\mu \Phi)^\dagger (D^\mu \Phi) - \mu^2 \Phi^\dagger \Phi - \frac{\lambda}{4} (\Phi^\dagger \Phi)^2 \\
& + \bar{L}_i^L i \not{D} L_i^L + \bar{e}_i^R i \not{D} e_i^R + \bar{Q}_{ib}^L i \not{D} Q_{ib}^L + \bar{u}_{ib}^R i \not{D} u_{ib}^R + \bar{d}_{ib}^R i \not{D} d_{ib}^R \\
& - \left( Y_{ij}^e \bar{L}_i^L \Phi e_j^R + Y_{ij}^u \bar{Q}_{ib}^L \Phi u_{jb}^R + Y_{ij}^d \bar{Q}_{ib}^L \Phi d_{jb}^R + h.c. \right) \\
& - \frac{1}{4} (B_{\mu\nu} B^{\mu\nu} + W_{\mu\nu}^a W^{a\mu\nu} + G_{\mu\nu}^a G^{a\mu\nu}),
\end{aligned} \tag{I.1.1}$$

131 with  $\not{D} = \gamma_\mu D^\mu$  and the covariant derivative  $D^\mu = \partial^\mu + ig' Y_W B^\mu - ig C_1 I^a W_a^\mu - ig_S C_2 T^a G_a^\mu$ .  
132  $I^a$  and  $T^a$  denote hereby the generators of the  $SU(2)_L$  and  $SU(3)_C$ , respectively. They are  
133 connected to the three Pauli matrices and the eight Gell-Mann matrices by  $I^a = \frac{\sigma^a}{2}$  and  
134  $T^a = \frac{\lambda^a}{2}$ . Adding the hypercharge  $Y_W$  and the third component of the weak isospin result  
135 in the electrical charge  $Q = Y_W + I_3$ . Furthermore, it is  $C_1 = 1$  for doublets and  $C_1 = 0$   
136 for singlets under  $SU(2)_L$ ,  $C_2 = 1$  for triplets and  $C_2 = 0$  for singlets under  $SU(3)_C$ .

137 The first line in Eq. (I.1.1) correspond to the kinetic term of the Higgs field and its  
138 potential. Via this Higgs field, it is possible to give masses to the  $Z$ - and  $W^\pm$ -bosons as well

as the fermions. This will be explained in detail in the following Section I.1.3. The second line describes the kinetic terms of the leptons and quarks. The index  $i$  represents the three different families ( $i = 1, 2, 3$ ). Since they are spin 1/2 particles, they can be described with the help of Dirac spinors. The left-handed leptons and quarks are described as  $SU(2)_L$  doublets,  $L_I^L = (\nu_{eL}, e_L)_i$ ,  $Q_I^L = (u_L, d_L)_i$ , the right-handed as singlets under  $SU(2)_L$   $e_i^R$ ,  $u_i^R$ ,  $d_i^R$ . Quarks carry a further quantum number, the colour, which is indicated by the index  $b$  with  $b = 1, 2, 3$ . Quarks transform as triplets under the  $SU(3)_C$  gauge group. The third line contains the interaction terms between the fermions and the Higgs boson, called Yukawa interactions. These terms lead after SSB to the fermion mass terms, as can be seen later. The last line correspond to the kinetic terms of the gauge fields. These are connected to the field strength tensors by

$$\begin{aligned}
B^{\mu\nu} &\equiv \partial^\mu B^\nu - \partial^\nu B^\mu \\
W^{\mu\nu} &\equiv \partial^\mu W^\nu - \partial^\nu W^\mu - ig [W^\mu, W^\nu] \\
&= \left( \partial^\mu W_i^\nu - \partial^\nu W_i^\mu + g \epsilon_{ijk} W_j^\mu W_k^\nu \right) \frac{\sigma_i}{2} \equiv \frac{\sigma_i}{2} W_a^{\mu\nu} \\
G^{\mu\nu} &\equiv \partial^\mu G^\nu - \partial^\nu G^\mu - ig_S [G^\mu, G^\nu] \\
&= \left( \partial^\mu G_a^\nu - \partial^\nu G_a^\mu + g_S f_{abc} G_b^\mu G_c^\nu \right) \frac{\lambda_a}{2} \equiv \frac{\lambda_a}{2} G_a^{\mu\nu}.
\end{aligned} \tag{I.1.2}$$

The factors  $\epsilon_{ijk}$  and  $f_{abc}$  are hereby the structure constants of the corresponding lie groups. The summation over all indices that appear twice is included.

### I.1.3 The Brout-Englert-Higgs mechanism

An essential ingredient of the Standard Model is the Brout-Englert-Higgs mechanism (BEH mechanism), earlier also called Higgs mechanism. It was developed by Peter Higgs, Robert Brout and François Englert in 1960s [7–12]. Based on a work from Sheldon Glashow [13], Steven Weinberg and Abdus Salam later applied it on a  $SU(2) \times U(1)$  gauge theory [14,15]. By this, a renormalisable theory of the weak and the electromagnetic theory was born. Together with the theory of strong interaction, the formulation of the Standard Model was thus by this time complete.

#### Mass terms of the gauge bosons

Due to the BEH mechanism, it is possible to give masses to the  $W^\pm$ - and Z-bosons. A scalar field  $\Phi$  (Higgs field) is required, which has a non-zero vacuum expectation value. This is possible, when the mass parameter  $\mu$  in front of the bilinear term in line one of Eq. (I.1.1) is smaller than zero and  $\lambda > 0$  at the same time.

The resulting potential of the Higgs field is then the famous “Mexican hat” potential.

Expanding the Lagrangian density around the minimum of  $\Phi = (0, v)$ , the gauge symmetries of  $SU(2)_L \times U(1)_Y$  are spontaneously broken and only a remaining electrical charge conserving symmetry  $U(1)_{EM}$  remains. After an unitary transformation, three of the four degrees of freedom of the Higgs field are absorbed by the gauge fields. Thus, “after” SSB, the part of the Lagrangian containing the scalar field is as follows

$$\mathcal{L}_{\text{Higgs}} = \frac{1}{2} (\partial_\mu h^0)^\dagger (\partial^\mu h^0) - \mu^2 (h^0)^2 + \frac{1}{2} v^2 g^2 W_\mu^- W^{+\mu} + \frac{1}{4} v^2 (g^2 + g'^2) Z_\mu Z^\mu + \text{interaction terms} \quad (\text{I.1.3})$$

One kinetic and one mass term for one of the degrees of freedom of the Higgs fields remains, which is the Higgs boson ( $h^0$ ). Furthermore, three of the four gauge bosons require a mass. The remaining gauge boson, being the photon remains massless because of the conserved  $U(1)_{EM}$  gauge symmetry.

The mass eigenstates of the gauge bosons in Eq. (I.1.3) are obviously different to the interaction eigenstates in Eq. (I.1.1). The diagonalisation of the neutral mass matrices is described by the Weinberg angle  $\theta_W$

$$\begin{pmatrix} A_\mu \\ Z_\mu \end{pmatrix} = \begin{pmatrix} \cos \theta_W & -\sin \theta_W \\ \sin \theta_W & \cos \theta_W \end{pmatrix} \begin{pmatrix} B_\mu \\ W_\mu^3 \end{pmatrix}. \quad (\text{I.1.4})$$

For the charged gauge bosons, the relation between  $W_{1,2}$  and  $W^\pm$  is the following

$$W_\mu^\pm = \frac{1}{\sqrt{2}} [W_\mu^1 \mp W_\mu^2]. \quad (\text{I.1.5})$$

Consequently, the masses of the gauge boson are the following

$$\begin{aligned} M_H &= \sqrt{2} \mu \\ M_W &= \frac{g}{\sqrt{2}} v \\ M_Z &= \frac{1}{\sqrt{2}} v \sqrt{g^2 + g'^2} \\ M_\gamma &= 0. \end{aligned} \quad (\text{I.1.6})$$

The first direct observation of the  $Z$ - and  $W^\pm$ -bosons was made in  $p\bar{p}$ -collisions in the year 1983 at the Super Proton Synchrotron (SPS) at CERN [16, 17]. The experimental values of the masses are  $m_Z = 91.1876 \pm 0.0021 \text{ GeV}$  and  $m_{W^\pm} = 80.385 \pm 0.015 \text{ GeV}$  [18]. Finally, as mentioned several times before, the Higgs boson was found at the LHC in the year 2012 [2, 3]. The mass is measured to  $m_{h^0} = 125.09 \pm 0.21(\text{stat.}) \pm 0.11(\text{sys.}) \text{ GeV}$  [19].

## Mass terms of the fermions

Fermion mass terms cannot be easily inserted into the Lagrangian density in Eq. (I.1.1), since they would violate the imposed gauge symmetries. With the help of the BEH mechanism it is possible to generate fermion mass terms via the Yukawa interactions terms (line three of Eq. (I.1.1)). After spontaneous symmetry breaking, the Yukawa interactions lead to the following mass terms (colour indices are suppressed)

$$\mathcal{L}_{\text{Yukawa}} = - \left( Y_{ij}^e v \bar{e}_i^L e_j^R + Y_{ij}^u v \bar{u}_i^L u_j^R + Y_{ij}^d v \bar{d}_i^L d_j^R + h.c. \right) + \text{interaction terms} \quad (\text{I.1.7})$$

The fermion masses are thus described by the following mass matrices

$$M_{ij}^e = Y_{ij}^e v \quad M_{ij}^u = Y_{ij}^u v \quad M_{ij}^d = Y_{ij}^d v \quad (\text{I.1.8})$$

Since the Standard Model does not contain right-handed neutrinos, there are no gauge invariant Yukawa interactions, that could produce mass terms for neutrinos.

### I.1.4 Limitations of the Standard Model

Despite the great success of the Standard Model, there remain observations and theoretical considerations that cannot be answered within the SM. In the following, the most important of such “limitations” shall be reviewed.

First of all, the Standard Model suffers of the so-called hierarchy problem. By this, the problem is addressed that quadratic divergencies occur in the calculation of the Higgs self-coupling. The appearance of infinities is not uncommon in higher order calculations and happens for all particles. Still, for scalar particles the infinite term is quadratically divergent, which makes a huge difference compared to the logarithmic divergencies for fermion self-energies. When considering the Standard Model valid up to the Planck scale, an extraordinary fine-tuning would be needed to cancel a large bare mass with large counter terms

$$m_{h^0}^{\text{ren } 2} = m_{h^0}^{\text{bare } 2} + \Delta m_{h^0}^2. \quad (\text{I.1.9})$$

to end up with a mass of about 125 GeV. Thus, this renormalisation procedure, even if mathematically possible, is regarded as highly unnatural in physics. The question which is usually imposed is, why is the Higgs mass so small, when there are such massive corrections to the bare mass? A formulation of naturalness was given by t’Hooft in 1977 [20]. He stated, that a small parameter can be regarded only natural, if the symmetries of the theory are enhanced by setting this parameter to zero. In the Standard Model, though,

there is no enhancement of the symmetries of the Lagrangian by setting  $\mu = 0$ , thus the small mass of the Higgs boson compared to the Planck scale is considered as highly unnatural.

A further and probably the most striking shortcoming of the Standard Model is the missing fourth fundamental force, the gravitational force. Within the SM, it is not possible to add renormalisable terms, that can describe the gravitational force. Although, gravity is not important for particle physics at energies that are accessible at current particle colliders (it only becomes important at the Planck scale  $\sim 10^{19}$  GeV), the fact that it cannot be embedded into the Standard Model leads to an understanding of the SM as effective theory, only valid for lower energies. Thus, it is obviously not an ultimate theory and something must be beyond.

Furthermore, in particle physics there is always the wish to describe nature with a theory as simple as possible. This usually implies the effort to embed the Standard Model into a higher symmetry group. To achieve a simplification by unifying the three fundamental forces is usually done within so-called Grand-Unified-Theories (GUTs). Calculating the running of the coupling constants in the Standard Model, the couplings seem to meet at a scale of  $M_{\text{GUT}} \sim 10^{15}$  GeV. Unfortunately, they don't meet exactly. Therefore, a unification is not achievable in the Standard Model under the assumption that there are no new particles up to the GUT scale.

Finally, there is experimental evidence, which cannot be explained within the Standard Model. Astrophysical observations suggest that there is a large amount of dark matter (DM) in the universe, that cannot be explained with the particle content of the Standard Model. Measurements of the velocity curves of galaxies, e. g. M33 [21] show discrepancies between the observed velocities and the predicted velocities by the visible matter. The share of non-visible matter to the total amount of matter in the universe is estimated to be 84% [22]. Unfortunately, there is no suitable (only weakly interacting) candidate within the SM, that can make up the full DM contribution.

In the following Section I.2, a theory is introduced, that can address most of the above mentioned problems. This theory is called Supersymmetry.

## I.2 Supersymmetry

As noted in the last chapter, the Higgs boson mass suffers from quadratic divergencies through radiative corrections. The reason for the quadratic divergencies is due to the

fact, that the Lagrangian density does not contain further symmetries for  $\mu \rightarrow 0$ . This behaviour is typical for scalar particles. For fermions, on the other hand, there is a further symmetry for  $m_f = 0$ . The Lagrangian density becomes invariant under chiral transformations of the form  $\Psi \rightarrow e^{i\vec{\alpha}\frac{\vec{\sigma}}{2}\gamma_5}\Psi$ . Although the mass terms of the fermions break this symmetry, it protects the fermions against large radiative corrections.

Due to these considerations, it seems natural to protect also the scalar mass by an additional symmetry. A work from Golfand and Likhtman in the year 1971 stated that an extension of the Poincaré algebra is possible via fermionic generators [23]. R. Haag, J. Lopuszanski and M. Sohnius finalised these considerations by showing that with the help of fermionic generators a connection between space-time symmetries and internal symmetries is possible [24]. The extensions of a symmetry group by fermionic generators is called Supersymmetry (SUSY). These were the foundation of supersymmetric theories.

In the following, few aspects of supersymmetric theories are discussed. For a detailed introduction the reader is referred to [25–27].

In the subsequent sections, the descriptions is restricted to the case of  $N = 1$  supersymmetry, i.e. there is only one supersymmetric generator and thus only one supersymmetric partner for every particle. A supersymmetric transformation transfers every bosonic state into a fermionic state and vice versa

$$\begin{aligned} Q |\text{boson}\rangle &= |\text{fermion}\rangle \\ Q |\text{fermion}\rangle &= |\text{boson}\rangle. \end{aligned} \tag{I.2.1}$$

The most important (anti-) commutation relations for SUSY algebra with spinors  $Q$  are

$$\begin{aligned} \{Q_\alpha, Q_\beta\} &= \{Q_\alpha^\dagger, Q_\beta^\dagger\} = 0, \\ [Q_\alpha, P_\mu] &= [Q_\alpha^\dagger, P_\mu] = 0, \\ \{Q_\alpha, Q_\alpha^\dagger\} &= 2\sigma_{\alpha\dot{\alpha}}^\mu P_\mu. \end{aligned} \tag{I.2.2}$$

$P_\mu$  denotes hereby the four component generator of translations. Additionally, it is  $\sigma^\mu = (\mathbb{1}, \sigma_i)$  with the Pauli matrices  $\sigma_i$ . From the second relation in (I.2.2) it follows

$$[Q_\alpha, P^2] = [Q_\alpha^\dagger, P^2] = 0. \tag{I.2.3}$$

Equation I.2.3 implies, that particles that are transformed into each other with the generator  $Q$  need to have same eigenvalues of  $P^2$ , thus, also same masses. This impose obviously a problem, since no “scalar electron” was ever found with a mass of 0.51 MeV. This problem will be discussed later.

In Supersymmetry, all particles and their partner particles are described by so-called supermultiplets. Since the generators of the gauge group commute with the generators of supersymmetry, all particles within one supermultiplet have same quantum numbers, besides the spin (as shown in Eq. I.2.3 they have also same masses). In a renormalisable theory, there are two different types of supermultiplets: chiral multiplets, which contain a two-component Weyl spinor and a complex scalar field and vector multiplets with a vector boson and a two-component Weyl spinor. The number of degrees of freedom are thus for chiral multiplets for on-shell particles

$$\begin{aligned} n_f &= 2, \text{ due to the two-component Weyl spinor} \\ n_b &= 2, \text{ due to the complex scalar field,} \end{aligned}$$

and for vector multiplets for on-shell particles

$$\begin{aligned} n_f &= 2, \text{ due to the two-component Weyl spinor} \\ n_b &= 2, \text{ due to the vector field.} \end{aligned}$$

As mentioned before, in a realistic extension of the Standard Model, Supersymmetry cannot be exact, since no supersymmetric particles have been found which have the same masses as their SM partners. This implies, that SUSY must be broken. There are many ideas how the breaking can actually happen. However, since up to now, only little is known about the breaking mechanism, usually further terms which break SUSY explicitly, are added by hand to the Lagrangian density. These terms can parametrise SUSY breaking without the knowledge about the breaking mechanism. One condition is however imposed on the supersymmetry breaking terms: they should not spoil the naturalness of the new theory, i.e. no new quadratic divergencies shall occur due to these terms. Therefore, they are called soft-breaking terms. How they actually look, will be explained in the Section I.2.1.

Finally, it shall be discussed how Supersymmetry can give possible answers to the shortcomings of the Standard Model, discussed in Section I.1.4.

Radiative corrections by fermions always have a factor  $-1$  compared to bosonic corrections. Thus, calculating radiative corrections of the Higgs boson mass in a supersymmetric theory leads in addition to the corrections by SM particles also to further corrections by SUSY particles. If SUSY were exact, the quadratic divergencies  $\Delta m_H^2$  would exactly cancel. However, as argued, SUSY must be broken. The cancellation of quadratic divergencies can therefore only be assured, if the breaking is not too drastic and only logarithmic divergencies remain. To avoid a new source of fine-tuning, the soft-breaking parameters should be of the order  $M_{\text{soft}} \sim 100 \text{ GeV} - 1000 \text{ GeV}$ .

Even though, it is not possible to implement gravity within a supersymmetric extension

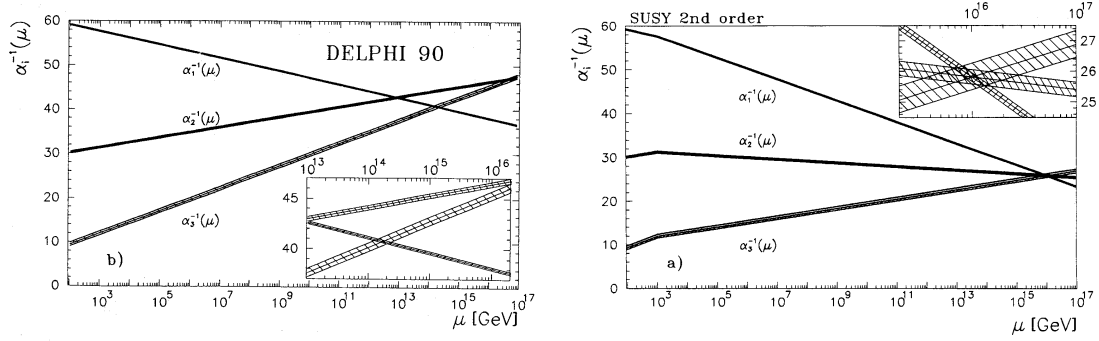


Figure I.2.1: The running of the gauge couplings in the Standard Model (left) and in the minimal supersymmetric extension of the SM (right). Taken from [28].

of the Standard Model, theories that are able to include gravity (string theories) require also Supersymmetry.

The renormalisation group equations change under a supersymmetric extension of the Standard Model. By this, a unification of the gauge couplings at a GUT scale of about  $10^{16}$  GeV is possible, as can be seen in Fig. I.2.1. It can be nicely seen, that all three gauge couplings cross each other within the uncertainties.

Besides these arguments, SUSY can also give an answer to the problem of non-visible matter in the universe. If the conservation of the so-called R-parity is required, the lightest supersymmetric particle (LSP) is stable. If this particle is only weakly interacting, it can serve as a good candidate to explain fully or partially the sources of the relic density. R-parity is a multiplicative quantum number with

$$\begin{aligned} P_R &= 1 && \text{SM particles} \\ P_R &= -1 && \text{SUSY particles.} \end{aligned}$$

If R-parity is conserved, only terms are allowed in the Lagrangian density, that contain an even number of supersymmetric particles. Therefore, no single SUSY particle can decay into only SM particles and thus, the LSP is stable.

### I.2.1 The MSSM

The supersymmetric extension of the Standard Model with a minimal particle content is called the Minimal Supersymmetric Standard Model (MSSM). In the following section, the particle content of the MSSM is introduced.



### I.2.1.1 The particle content of the MSSM

In  $N = 1$  Supersymmetry, every SM particle has exactly one supersymmetric partner particle, which leads to a doubling of the particle content in the MSSM with respect to the SM. Additionally, there is a necessity for a second Higgs doublet. The second doublet is needed to ensure the holomorphicity of the superpotential when also mass terms for the up-type particles shall be created. Furthermore, the MSSM stays only free from anomalies if there is a further Higgs doublet. This leads to the fact, that in the MSSM, there are five Higgs bosons instead of only one as in the SM. The complete particle content of the MSSM is depicted in Tables I.2.1 and I.2.2.

Since in supersymmetric theories only left-handed Weyl spinors appear in the Lagrangian density, the right-handed are described as charge conjugated spinors of the left-handed spinors.

Table I.2.1: Chiral supermultiplets in the MSSM

		spin 0	spin $\frac{1}{2}$	$SU(3)_C, SU(2)_L, U(1)_Y$
squarks/quarks	Q	$(\tilde{u}_L, \tilde{d}_L)$	$(u_L, d_L)$	<b>3, 2, <math>\frac{1}{3}</math></b>
	$\bar{u}$	$\tilde{\bar{u}}_L = \tilde{u}_R^\dagger$	$\bar{u}_L = (u_R)^c$	<b><math>\bar{3}, 1, -\frac{4}{3}</math></b>
	$\bar{d}$	$\tilde{\bar{d}}_L = \tilde{d}_R^\dagger$	$\bar{d}_L = (d_R)^c$	<b><math>\bar{3}, 1, \frac{2}{3}</math></b>
sleptons/leptons	L	$(\tilde{\nu}_{eL}, \tilde{e}_L)$	$(\nu_{eL}, e_L)$	<b>1, 2, <math>-1</math></b>
	$\bar{e}$	$\tilde{\bar{e}}_L = \tilde{e}_R^\dagger$	$\bar{e}_L = (e_R)^c$	<b><math>\bar{1}, 1, 2</math></b>
Higgs/higgsinos	$H_u$	$(H_u^+, H_u^0)$	$(\tilde{H}_u^+, \tilde{H}_u^0)$	<b>1, 2, 1</b>
	$H_d$	$(H_d^0, H_d^-)$	$(\tilde{H}_d^0, \tilde{H}_d^-)$	<b>1, 2, <math>-1</math></b>

### I.2.1.2 The Lagrangian density of the MSSM

In the following only the most important parts of the MSSM Lagrangian density will be described. The reader is again referred to [27] for a complete description of the Lagrangian density.

Table I.2.2: Vector supermultiplets in the MSSM

	spin $\frac{1}{2}$	spin 0	$SU(3)_C, SU(2)_L, U(1)_Y$
gluinos/gluons	$\tilde{g}$	$g$	<b>8, 1, 0</b>
winos/ $W$ -bosons	$\tilde{W}^\pm, \tilde{W}^0$	$W^\pm, W^0$	<b>1, 3, 0</b>
bino/ $B$ -boson	$\tilde{B}$	$B$	<b>1, 1, 0</b>

### 339 The superpotential

340 The superpotential of the MSSM contains the self interaction terms of the Higgs bosons  
 341 and generates the interaction terms of the Higgs bosons with the fermions and their super-  
 342 partners. As already noted, it is very common to assume R-parity conservation. Hence, no  
 343 terms appear in the Lagrangian that would violate lepton or baryon number conservation  
 344 and the lightest supersymmetric particle is stable. Thus, all possible terms are

$$W_{\text{MSSM}} = \mu H_u \cdot H_d - Y_u^{ij} H_u \cdot Q_L^i u_R^{cj} + Y_d^{ij} H_d \cdot Q_L^i d_R^{cj} + Y_e^{ij} H_d \cdot L_L^i e_R^{cj}, \quad (\text{I.2.4})$$

345 with the dot product defined as in [26]

$$A \cdot B = \epsilon^{\alpha\beta} A_\alpha B_\beta = A_1 B_2 - A_2 B_1. \quad (\text{I.2.5})$$

### 346 The soft-breaking Lagrangian density

347 Since Supersymmetry is broken, explicit SUSY breaking terms are added to the Lagrangian  
 348 density. In order not to introduce new sources of quadratic divergencies, only bilinear and  
 349 trilinear terms appear in the soft-breaking Lagrangian

$$\begin{aligned}
 -\mathcal{L}_{\text{soft}}^{MSSM} = & m_{H_u}^2 H_u^\dagger \cdot H_u + m_{H_d}^2 H_d^\dagger \cdot H_d + (B\mu H_u \cdot H_d + h.c.) \\
 & + m_{\tilde{Q}}^2 \tilde{Q}_{Lij}^\dagger \cdot \tilde{Q}_{Lj} + m_{\tilde{u}}^2 \tilde{u}_{Ri}^{c\dagger} \cdot \tilde{u}_{Rj}^c + m_{\tilde{d}}^2 \tilde{d}_{Ri}^{c\dagger} \cdot \tilde{d}_{Rj}^c \\
 & + m_{\tilde{L}}^2 \tilde{L}_{Lij}^\dagger \cdot \tilde{L}_{Lj} + m_{\tilde{e}}^2 \tilde{e}_{Ri}^{c\dagger} \cdot \tilde{e}_{Rj}^c \\
 & + \left( -(A_u Y_u)_{ij} H_u \cdot \tilde{Q}_{Li} \tilde{u}_{Rj}^c + (A_d Y_d)_{ij} H_d \cdot \tilde{Q}_{Li} \tilde{d}_{Rj}^c \right. \\
 & \left. + (A_e Y_e)_{ij} H_d \cdot \tilde{L}_{Li} \tilde{e}_{Rj}^c + h.c. \right) \\
 & + \left( M_1 \tilde{B} \tilde{B} + M_2 \tilde{W}_a \tilde{W}_a + M_3 \tilde{g}_i \tilde{g}_i + h.c. \right)
 \end{aligned} \quad (\text{I.2.6})$$

The first line contains mass terms for the Higgs bosons, the second and third line for the sfermions. In the fourth and fifth line the trilinear couplings between the Higgs bosons and the sfermions appear. Finally, the last line give rise to mass terms for the gauginos.

Because of the soft-breaking terms, the MSSM contains more than 100 free parameters. Constraining the MSSM is thus a difficult task and usually in experimental particle physics, constrained versions of the MSSM or assumptions at the GUT scale are used to report the impact of searches on SUSY. In the following a short introduction of the phenomenological MSSM is given. With its reduced parameter space, it allows to elaborate on long-lived particles in the MSSM in a much easier way.

### I.2.1.3 The phenomenological MSSM

The phenomenological MSSM (pMSSM) imposes constraints that are reasonable in the sense to fulfil current observations and still keep the phenomenological richness of the MSSM [29]. The following assumptions are imposed (in [29] more detailed information about these assumptions can be found):

- No new sources of CP violation,
- No flavour changing neutral currents,
- First and second generation universality.

These assumption reduce the number of SUSY parameters to only 19. The remaining free parameters are the following:

- $\tan \beta$  (the ratio of the vacuum expectation values of the two Higgs doublets)
- $M_A$  (the mass of the pseudo-scalar Higgs boson)
- $\mu$  (the Higgs mass parameter)
- $M_1, M_2, M_3$  (bino, wino and gluino mass parameters, respectively)
- $m_{\tilde{q}}, m_{\tilde{l}}, m_{\tilde{u}}, m_{\tilde{d}}$  and  $m_{\tilde{e}}$  (the first and second generation mass parameters)
- $m_{\tilde{Q}}, m_{\tilde{L}}, m_{\tilde{t}}, m_{\tilde{b}}$  and  $m_{\tilde{\tau}}$  (the third generation mass parameters)
- $A_t, A_b$  and  $A_\tau$  (third generation trilinear couplings).

## I.2.2 Supersymmetry breaking

As already noted, the mechanism of supersymmetry breaking is unknown. There exists however, several ideas how to spontaneously break supersymmetry. All mechanism have

379 in common that they need to happen at high energies in a hidden sector. “Messenger”  
380 particles are introduced which mediate the breaking to the TeV scale. This, however,  
381 implies that supersymmetry breaking is a question of high-energy physics and one can  
382 always parametrise the breaking by the soft breaking terms introduced in Section I.2.1.2.  
383 The most popular breaking mechanism is gravity mediated Supersymmetry breaking [?]  
384 and gauge-mediated supersymmetry breaking [?].

## 385 **I.3 Long-lived particles in the MSSM**

- 386 • Mechanism of long lifetimes

### 387 **I.3.1 Previous searches for long-lived charged particles**

388

## **Part II**

389

### **Measurement of the jet transverse-momentum resolution**

390



## II.1 Introduction

The determination and quantification of the quality of the jet transverse-momentum measurement is of crucial interest for many analyses with jet final states, e. g. the measurement of the dijet cross section [30] or  $t\bar{t}$  production cross sections [31]. Also searches for physics beyond the standard model with missing transverse momentum,  $\cancel{p}_T$ , in the final state need a good knowledge of  $\cancel{p}_T$  originating from wrongly measured jets [32–34]. For analyses relying on information from simulation it is very important to correct the simulated resolution to the resolution actually present in data. Therefore, scale factors will be presented to adjust the resolution in simulation to the resolution of the real detector.

In the following sections, a data-based method to measure the jet  $p_T$  resolution in  $\gamma + \text{jet}$  events will be presented. A similar method was already accomplished in earlier analyses [35, 36] of 7 TeV data. It is further developed here and applied to  $19.7 \text{ fb}^{-1}$  of  $\sqrt{s} = 8 \text{ TeV}$  data.

The method is based on the transverse-momentum balance in the  $\gamma + \text{jet}$  system. It takes advantage of the high resolution of the electromagnetic calorimeter and hence the excellent measurement of the photon energy and momentum. Without initial and final state radiation, the photon and the jet are balanced in the transverse plane. Thus, measuring the photon  $p_T$  with high accuracy leads to an estimate of the true jet transverse momentum offering a possibility to quantify the resolution of jet  $p_T$  measurements.

## II.2 General approach of the resolution measurement using photon+jet events

The jet transverse-momentum resolution is defined as the standard deviation of the jet transverse-momentum response distribution with the response defined as the ratio of the reconstructed to the generator-level jet transverse momentum

$$\mathcal{R} = \frac{p_T^{\text{reco. jet}}}{p_T^{\text{gen. jet}}}. \quad (\text{II.2.1})$$

For each reconstructed jet, the underlying generator-level jet is hereby found by matching the closest generator-level jet to the reconstructed jet with  $\Delta R = \sqrt{(\Delta\phi)^2 + (\Delta\eta)^2}$  with a maximal value of  $\Delta R_{\max} = 0.25$ . Furthermore, the transverse momentum of the generator-level jet is defined as the sum of all particles' transverse momenta from the hadronisation that are clustered into the jet cone. Throughout the following sections, the jet transverse-momentum resolution will be abbreviated JER<sup>1</sup>. The mean of the response distribution will be referred to as jet energy scale (JES).

Figure II.2.1 shows a response distribution for jets in the barrel region. The core of the response distribution shows the typical Gaussian behaviour whereas the tails deviate from that functional form. Physical reasons for the low response tail are inter alia semi-leptonic decays of heavy quarks where the neutrino cannot be detected and the reconstructed transverse momentum of the jet is too small. This effect is visible in Fig. II.2.1 because the neutrinos are included into the generator-level jet. Some instrumental effects, such as a non-linear response of the calorimeter, inhomogeneities of the detector material and electronic noise can contribute to both tails, others, like dead calorimeter channels only contribute to the left tail. The resolution is therefore determined using only the core of the distribution to avoid the coverage of non-Gaussian tails. The resolution is thus defined as the standard deviation of the 99% truncated response histogram divided by the mean of the histogram:

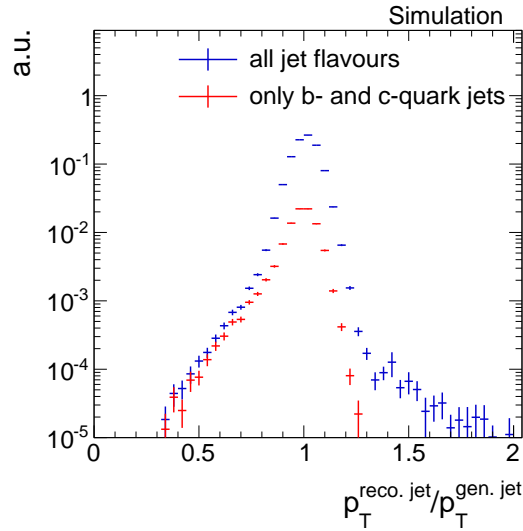


Figure II.2.1: Normalised number of events over  $p_T^{\text{reco. jet}}/p_T^{\text{gen. jet}}$  from a simulated  $\gamma + \text{jet}$  sample. The contribution by c- and b-quark jets is shown in red, which cause almost fully the left tail originating from semi-leptonic decays.

<sup>1</sup>This abbreviation is a historical relic from experiments where the momentum of jets were only measured in the calorimeters and therefore JER referred to jet energy resolution.



$$\sigma_{\text{JER}} = \frac{\sigma_{99\%}}{\mu_{99\%}}.$$

The determination of the 99% range of the histogram is done in several steps. First the mean of the core is found via a Gaussian fit to the histogram in a  $2\sigma$  range<sup>2</sup>. This procedure is done in three iteration steps. Then, a symmetric interval around this mean is determined with its integral equal to 99% of the integral of the full histogram. The division by the mean aims to make the resolution independent of the absolute scale (= mean) of the response distribution. It is done because response distributions with a scale smaller than one are typically narrower while distributions with scales larger than one are broader. However, since after the application of the jet energy corrections the scale is very close to one, this is only a tiny effect.

The evaluation of the response distribution as reconstructed over generator-level jet transverse momentum (Eq. (II.2.1)) is only possible for simulated events where generator-level information is accessible. A determination of the resolution in data, however, has to rely on a different approach.

The main idea of a resolution measurement using  $\gamma$ +jet events is based on the transverse-momentum balance of the  $\gamma$  + jet system and the excellent electromagnetic calorimeter resolution (which was estimated between 1.4% and 3.8% in the barrel region for photons for  $\sqrt{s} = 8$  TeV data [37]).

In Fig II.2.2, all tree-level processes contributing to an event topology with one photon and one jet in the final state are depicted. Due to momentum conversation, the jet and the photon are back to back in the transverse plane, and therefore,  $\vec{p}^\gamma = -\vec{p}^{\text{jet}}$ . Because of the good resolution of the electromagnetic calorimeter, photon momenta can be very well measured and thus can serve as an excellent estimator for the true jet momentum.

Unfortunately, such clean events are very rare processes, and usually, the momentum balance is spoiled by initial and final state radiation, which lead to further jets in the event (see Fig. II.2.3). However, in order to select events that are balanced to a large extent, a lower bound on the angular distance in the transverse plane between the photon and the jet

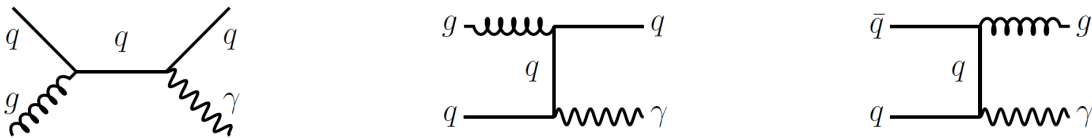


Figure II.2.2: Tree-level Feynman diagrams of processes at the LHC in  $pp$ -collisions with one photon and one jet in the final state.

<sup>2</sup>The  $2\sigma$  range is defined as the range  $[\mu - 2\sigma, \mu + 2\sigma]$ .



Figure II.2.3: Tree-level Feynman diagrams with initial and final state radiation.

461 with the highest transverse momentum (leading jet) is required:  $\Delta\Phi(1^{\text{st}} \text{ jet}, \gamma) > 2.95 \text{ rad.}$

462 Additionally, the variable

$$\alpha \doteq \frac{p_{\text{T}}^{2^{\text{nd}} \text{ reco. jet}}}{p_{\text{T}}^{\gamma}}$$

463 is defined as a measure of further jet activity in an event. It is, however, not sufficient  
 464 to require only an upper bound on  $\alpha$ . Instead, the jet transverse-momentum resolution is  
 465 measured in bins of  $\alpha$  (with  $\max(\alpha) = 0.2$ ), and the extrapolated value to zero further jet  
 466  $p_{\text{T}}$  ( $\alpha = 0$ ) is taken as the measured resolution of the jet  $p_{\text{T}}$  in the absence of further jets.

467

468 Measuring the transverse momentum of the photon instead of taking the generator-level  
 469 jet  $p_{\text{T}}$  leads to the fact that the measured resolution consists out of two parts

$$\frac{p_{\text{T}}^{\text{reco. jet}}}{p_{\text{T}}^{\gamma}} = \underbrace{\frac{p_{\text{T}}^{\text{reco. jet}}}{p_{\text{T}}^{\text{gen. jet}}}}_{\text{intrinsic}} \cdot \underbrace{\frac{p_{\text{T}}^{\text{gen. jet}}}{p_{\text{T}}^{\gamma}}}_{\text{imbalance}}.$$

470 The intrinsic part is the resolution of interest which is independent of further jets in the  
 471 event whereas the imbalance is strongly dependent on  $\alpha$ .

472 To extract the intrinsic resolution out of the measured one, the residual imbalance  $q$   
 473 (the imbalance at  $\alpha = 0$ ) is subtracted from the total resolution in the limit of vanishing  
 474 additional jet activity. Since this information is only available from simulation, the mea-  
 475 sured resolution in data is corrected by the residual imbalance taken from the simulated  
 476 dataset.

477 To account for differences in the jet transverse-momentum resolution for different true  
 478 jet  $p_{\text{T}}$  and different jet pseudorapidity regions, the measurement of the resolution is done  
 479 in  $p_{\text{T}}^{\gamma}$  bins and bins of  $|\eta|$  of the leading jet.

## II.3 Datasets and event selection

The measurement of the jet transverse-momentum resolution is carried out with  $\gamma + \text{jet}$  data recorded during the year 2012 at a centre-of-mass energy of  $\sqrt{s} = 8 \text{ TeV}$  at the CMS experiment. The datasets and triggers that are exploited for this measurement are introduced in the following Section II.3.1. The measured resolution in data is compared to the resolution in simulated samples. These are introduced in Section II.3.2. In order to select  $\gamma + \text{jet}$  events that are well suited for the resolution measurement, an event selection is applied on top. This event selection is described in Section II.3.3.

### II.3.1 Datasets and triggers

This analysis exploits several triggers which were active during the year 2012 at the CMS experiment. Because of the high production cross section of  $\gamma + \text{jet}$  events, especially for low photon  $p_T$ , almost all of these triggers were highly prescaled, i.e. only a fraction of events were actually recorded when the triggers fired. All triggers that are utilised in this measurement are listed in Table II.3.1 together with their recorded luminosity. The triggers rely on level one (L1) on single-photon triggers, such as L1SingleEG12 and

Table II.3.1: Single-photon triggers together with the recorded luminosity taking the prescales of the triggers into consideration.

Trigger	Luminosity [fb <sup>-1</sup> ]
HLT_Photon30_CaloIdVL_IsoL	0.0029
HLT_Photon50_CaloIdVL_IsoL	0.0607
HLT_Photon75_CaloIdVL_IsoL	0.123
HLT_Photon90_CaloIdVL_IsoL	0.373
HLT_Photon135	13.77
HLT_Photon150	19.71

L1SingleEG30. The L1 triggers require at least one photon that is above a certain  $p_T$  threshold, e. g. 12 GeV or 30 GeV. The high-level triggers require a photon with a certain  $p_T$  (as indicated in the name) and, in case of thresholds below 135 GeV also additional quality and isolation criteria. All triggers with threshold below 150 GeV were prescaled.

The events that are selected by the above mentioned triggers are contained in the datasets listed in Table II.3.2.

Table II.3.2: Single-photon data samples used for the resolution measurement with the contained integrated luminosity.

Dataset	Luminosity [ $\text{fb}^{-1}$ ]
/Photon/Run2012A-22Jan2013-v1/AOD	0.876
/SinglePhoton/Run2012B-22Jan2013-v1/AOD	4.412
/SinglePhoton/Run2012C-22Jan2013-v1/AOD	7.055
/SinglePhotonParked/Run2012D-22Jan2013-v1/AOD	7.354

### II.3.2 Simulated samples

In order to compare the measured resolution in data to the resolution in simulation, a single-photon sample simulated with PYTHIA6 is used. This sample is generated flat in the photon  $p_T$  to have a good statistical precision also for the high photon  $p_T$  region. In order to recover a physical  $p_T$  spectrum, all simulated events are reweighted. Figure II.3.1 shows the photon  $p_T$  spectrum in simulation before and after the reweighting.

All simulated samples come with a pileup scenario which does not necessarily match the pileup scenario in data. To match the measured distribution of primary vertices, the events are weighted according to their number of primary vertices. Because almost all of the used triggers are differently prescaled, the distributions of primary vertices differ among the various events triggered by the corresponding trigger. Thus the reweighting has to be done separately for the events falling in the photon  $p_T$  range of the several triggers (see Table II.3.3). A comparison between the number of primary vertices can be found in Appendix ?? for all triggers.

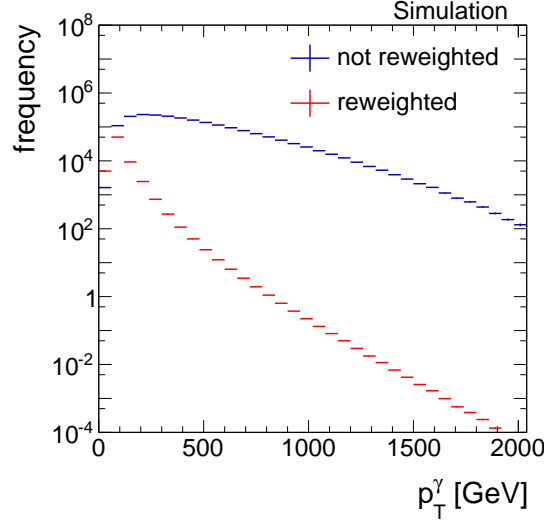


Figure II.3.1: The photon  $p_T$  spectrum before (blue) and after (red) reweighting.

### II.3.3 Event selection

Events are reconstructed with the particle-flow reconstruction algorithm, which uses information of all detector components to reconstruct individual particles [38]. In the following, the selection of well reconstructed jets and photons will be explained as well as the event selection of  $\gamma + \text{jet}$  events.

#### II.3.3.1 Jet selection

Particles belonging to a jet are clustered with the Anti- $k_t$  jet clustering algorithm with a radius of  $R=0.5$  [39]. Furthermore, all reconstructed jets undergo a so-called “charged hadron subtraction” (CHS) which removes hadrons that are likely caused by pileup events.

To select clean  $\gamma + \text{jet}$  events, it is required that the leading jet meets the following requirements (these criteria correspond to a ‘tight ID’ in [40, 41]):

- Neutral hadron fraction  $< 0.90$
- Neutral electromagnetic fraction  $< 0.90$
- Number of constituents  $> 1$

And for jets in the pseudorapidity range  $|\eta| < 2.4$ :

- Charged hadron fraction  $> 0$
- Charged hadron multiplicity  $> 0$
- Charged electromagnetic fraction  $< 0.99$

These selection cuts ensure a selection efficiency of around 99% and a noise rejection efficiency of 99.98% [40]. To mitigate effects from pileup, the first and second jet are required to have a transverse momentum greater 10 GeV.

### II.3.3.2 Photon selection

Concerning the photon, a maximal pseudorapidity of the photon of  $|\eta^\gamma| < 1.3$  is demanded to exploit the high resolution of the ECAL in the barrel region.

Furthermore, the resolution is determined for different ranges in photon  $p_T$  to avoid mixing of different prescales of the various triggers. In Table II.3.3 the applied binning is shown with the respective triggers contributing to each  $p_T^\gamma$  bin.

Table II.3.3: Photon  $p_T$  bins and corresponding triggers.

$p_T^\gamma$ -bins	Trigger
36 GeV	HLT_Photon30_CaloIdVL_IsoL_v*
60 GeV	HLT_Photon50_CaloIdVL_IsoL_v*
88 GeV	HLT_Photon75_CaloIdVL_IsoL_v*
105 GeV	HLT_Photon90_CaloIdVL_IsoL_v*
149 GeV	HLT_Photon135_v*
165 GeV	HLT_Photon150_v*

QCD-multijet events constitute an important background to the  $\gamma$ +jet events: A photon can be faked by a  $\pi^0$  decaying into two close-by photons. Therefore, a very clean selection of the photons is necessary to suppress this background. The following variables are used (see [?] for further explanation of the variables):

- $\frac{H}{E}$  : The ratio of the measured energy in the hadronic calorimeter over the energy measured in the electromagnetic calorimeter. For photons, this is supposed to be very small as they deposit their energy predominantly in the ECAL.
- $\sigma_{i\eta i\eta}$ : The energy weighted spatial width of the photon energy deposition. The electromagnetic shower of a photon has a small lateral size resulting in small  $\sigma_{i\eta i\eta}$  for prompt photons while showers from fake photons, e.g.  $\pi^0 \rightarrow \gamma\gamma$  have a larger lateral size.

- **Jurassic ECAL isolation:** This isolation criterion uses the information of reconstructed hits “RecHits” (coming from the local reconstruction of the digital signals) in a cone around the photon supercluster of  $R=0.4$ . Those are summed up and an upper criterion is identified to discriminate against background which is typically spatially broader.
- **Tower-based HCAL isolation:** The isolation criterion requires the energy deposited in all HCAL towers around the photon in cone of  $R=0.4$  to be small compared to the photon’s energy.
- **Hollow cone track isolation:** Requires absence of high-energetic tracks around the photon.
- **Pixel seed veto:** In order to reduce the background from electrons and positrons, the absence of a pixel-seed in the pixel tracker along the photons trajectory is required.

The upper and lower bounds that are set on these observables can be found in Table II.3.4.

Table II.3.4: Upper and lower bounds for all photon isolation criteria in the barrel ( $|\eta^\gamma| < 1.4442$ ).

	Barrel
$\frac{H}{E}$	$< 0.05$
$\sigma_{i\eta i\eta}$	$< 0.013$
ECAL isolation	$< 4.2 \text{ GeV} + 0.0060 \cdot p_T^\gamma$
HCAL isolation	$< 2.2 \text{ GeV} + 0.0025 \cdot p_T^\gamma$
Track Isolation	$< 2.0 \text{ GeV} + 0.0010 \cdot p_T^\gamma$
Pixel seed veto	yes

### II.3.3.3 Photon+jet event selection

Besides the mentioned requirements concerning the objects’ attributes, two further criteria related to the event topology are crucial for this analysis:

571 An upper threshold on  $\Delta\Phi$  between the leading jet and the photon and a maximal value  
 572 for  $\alpha$

573 •  $\Delta\Phi(1^{\text{st}} \text{ jet}, \gamma) > 2.95 \text{ rad}$

574 •  $\frac{p_{\text{T}}^{2^{\text{nd}} \text{ jet}}}{p_{\text{T}}^{\gamma}} < 0.20.$

575 These requirements are important to suppress events with too much further hadronic  
 576 activity.

577 A summary of all selection criteria can be found in Appendix ??.

578

579 Finally, the leading jet pseudorapidity interval bounds need to be chosen in order to  
 580 account for resolution differences in different detector regions. This is done according  
 581 to [42] with the following binning

$$\begin{aligned} |\eta^{1^{\text{st}} \text{ jet}}| &= 0.0 - 0.5 & |\eta^{1^{\text{st}} \text{ jet}}| &= 1.1 - 1.7 \\ |\eta^{1^{\text{st}} \text{ jet}}| &= 0.5 - 1.1 & |\eta^{1^{\text{st}} \text{ jet}}| &= 1.7 - 2.3. \end{aligned}$$

582 The binning in the  $p_{\text{T}}^{\gamma}$  dimension is chosen according to the trigger thresholds for  
 583  $p_{\text{T}}^{\gamma} < 165 \text{ GeV}$  and ensures sufficient statistical precision for  $p_{\text{T}}^{\gamma} > 165 \text{ GeV}$

$$\begin{array}{lll} p_{\text{T}}^{\gamma} = 36 - 60 \text{ GeV} & p_{\text{T}}^{\gamma} = 149 - 165 \text{ GeV} & p_{\text{T}}^{\gamma} = 200 - 300 \text{ GeV} \\ p_{\text{T}}^{\gamma} = 60 - 88 \text{ GeV} & p_{\text{T}}^{\gamma} = 165 - 176 \text{ GeV} & p_{\text{T}}^{\gamma} = 300 - 400 \text{ GeV} \\ p_{\text{T}}^{\gamma} = 88 - 105 \text{ GeV} & p_{\text{T}}^{\gamma} = 176 - 200 \text{ GeV} & p_{\text{T}}^{\gamma} > 400 \text{ GeV} \\ p_{\text{T}}^{\gamma} = 105 - 149 \text{ GeV} & p_{\text{T}}^{\gamma} = 300 - 400 \text{ GeV}. & \end{array}$$

## 584 II.4 Methodology of the measurement

585 The basic methodology of measuring the jet transverse-momentum resolution by exploiting  
 586 the  $p_{\text{T}}$  balance in  $\gamma + \text{jet}$  events and extrapolating the result to small  $\alpha$ , that was already  
 587 used in earlier analyses [35, 36], is extended in this measurement in order to explicitly  
 588 distinguish the case of parton radiation in different event hemispheres.

589 As already described in Chapter II.2, the idea behind a resolution measurement with  
 590  $\gamma + \text{jet}$  events is the usage of the photon  $p_{\text{T}}$  instead of the true jet  $p_{\text{T}}$ . This results in a



591 twofold contribution to the measured response, the intrinsic response and the imbalance:

$$\frac{p_T^{\text{reco. jet}}}{p_T^\gamma} = \underbrace{\frac{p_T^{\text{reco. jet}}}{p_T^{\text{gen. jet}}}}_{\text{intrinsic}} \cdot \underbrace{\frac{p_T^{\text{gen. jet}}}{p_T^\gamma}}_{\text{imbalance}}. \quad (\text{II.4.1})$$

592 Taking the photon  $p_T$  as true jet  $p_T$  estimator instead of the generator jet  $p_T$ , and thus  
 593 measuring the response defined as  $p_T^{\text{reco. jet}}/p_T^\gamma$ , results in a different shape of the response  
 594 function as shown in Fig. II.4.1. The figure compares the intrinsic response, the imbalance,  
 595 and the measured total response in simulation.

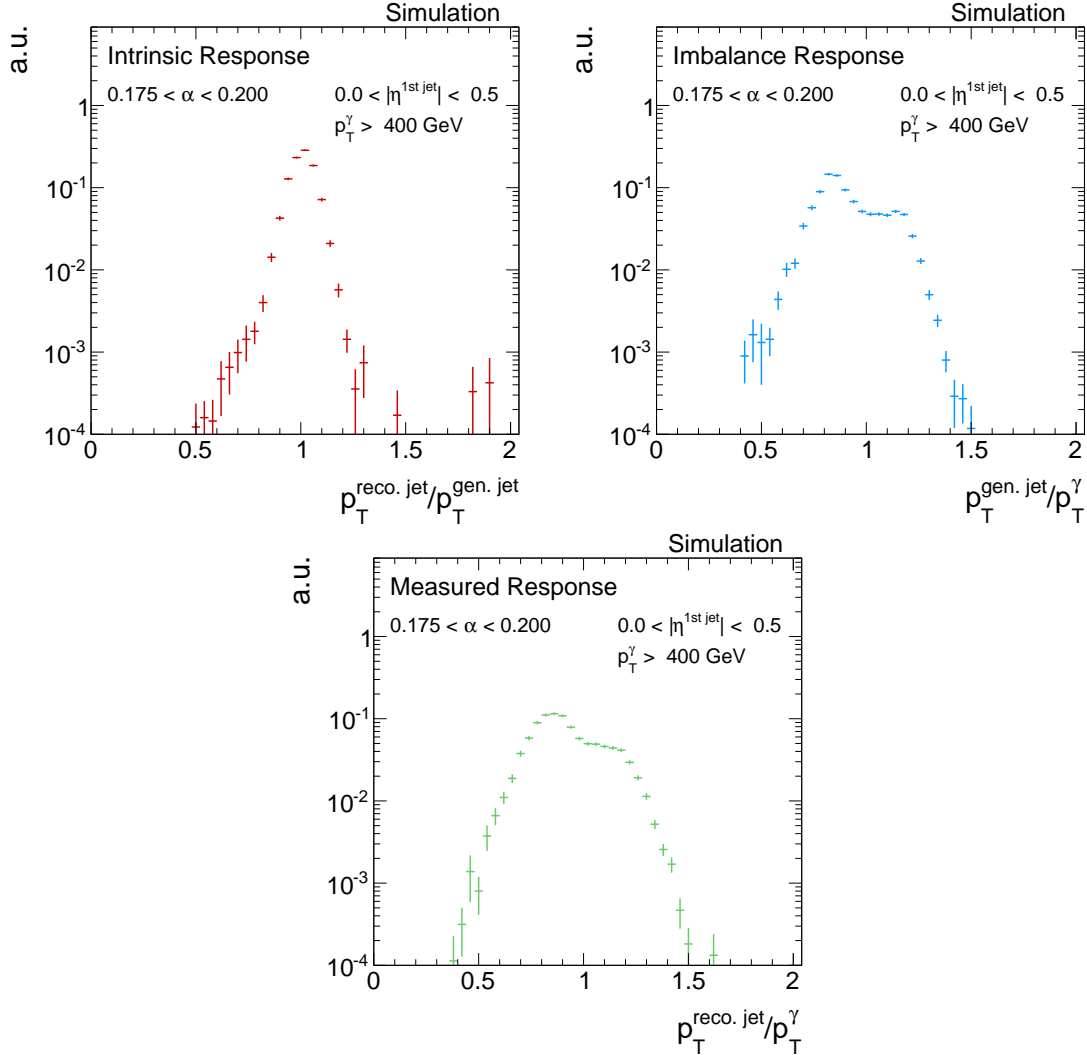


Figure II.4.1: The two different contributions, intrinsic (top left) and imbalance (top right), to the measured response (bottom) (cf. Eq. (II.4.1)) in simulated events.

The clear difference between the intrinsic response and the imbalance is the double peak structure of the latter one. The measured response is a convolution of the two contributions, where the double peak is consequentially less pronounced.

The occurrence of two peaks is caused by the hard selection in  $\Delta\phi$  which forces the second jet to be either close to the photon or close to the leading jet due to  $p_T$  conservation. The possibility of an energetic second jet perpendicular to the leading jet-photon axis which is balanced by a third jet is very unlikely due to the decreasing jet multiplicity in QCD-multijet events. The double peak structure is less pronounced for small second jet  $p_T$  (small  $\alpha$ ) where the  $\Delta\phi$  requirement does not have such a strong effect in rejecting events with a second jet perpendicular to the photon leading jet axis (see Fig. II.4.2).

These two different contributions (second jet in photon/leading jet hemisphere) result in two separate response distribution. A schematic sketch of the two contributions is shown in Fig. II.4.3.

The mathematical definitions of the hemispheres are as follows:

$$\text{Hemisphere} = \begin{cases} \text{Jet,} & \Delta\Phi(1^{\text{st}} \text{ jet}, 2^{\text{nd}} \text{ jet}) < \Delta\Phi(\gamma, 2^{\text{nd}} \text{ jet}), \\ \text{Photon,} & \text{else.} \end{cases} \quad (\text{II.4.2})$$

The two response distributions coming from the different event topologies are separately evaluated. First, the resolution is determined for each of the configurations (cf. Fig. II.4.4), and then, the weighted mean of the two contributions is calculated.

As can be seen in Fig. II.4.4, events containing a second jet in the leading jet hemisphere lead to a response histogram with mean smaller one, while events with a second jet in photon direction result in a distribution with mean larger one. The former occurs more frequently because it contains jets from final and initial state radiation, while the latter

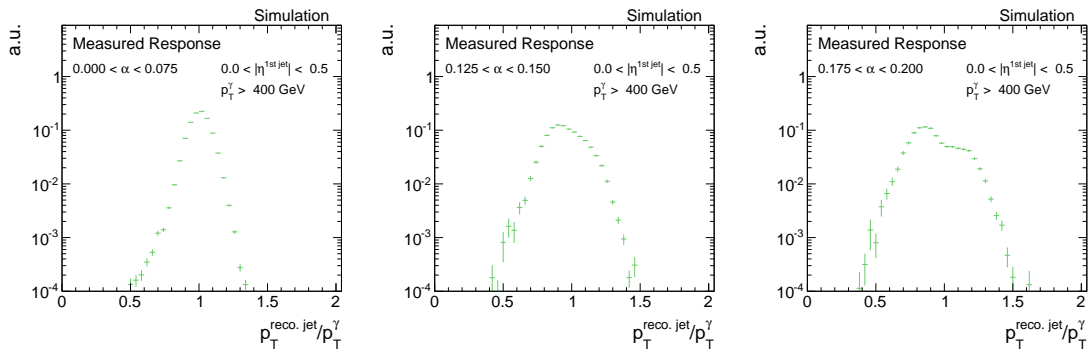


Figure II.4.2: The measured response  $p_T^{\text{reco, jet}}/p_T^\gamma$  in simulation for FIXME :  $p_T^\gamma < 400$  GeV for three different  $\alpha$  ranges: 0.0 – 7.5% (left), 12.5 – 15.0% (middle) and 17.5 – 20.0% (right). It can be seen that the double peak structure gets less pronounced for low  $\alpha$  values.

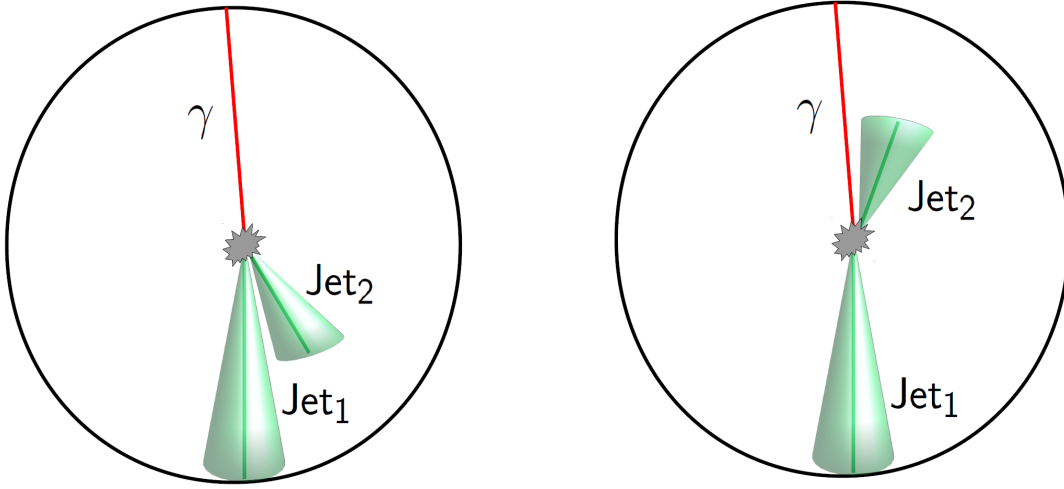


Figure II.4.3: A schematic sketch of the two different event topologies where the second jet is in the leading jet (left) or the photon hemisphere (right)

617 mainly consists only from initial state radiation.

618 The intrinsic part of the resolution for a given photon  $p_T$  bin is independent of secondary

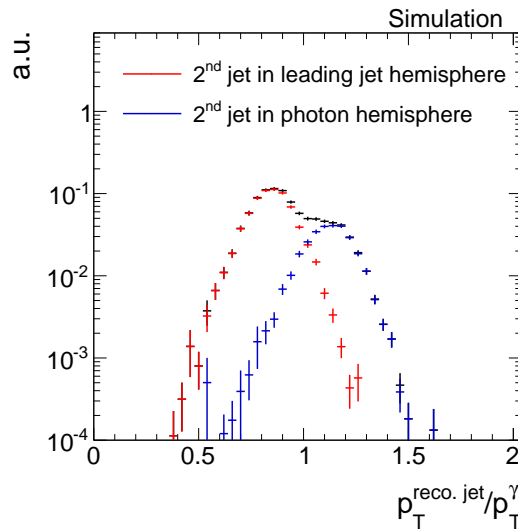


Figure II.4.4: The measured response with the two contributions visualised. Events with a second jet in photon hemisphere (red) lead to a mean response larger one, while events with a second jet in the leading jet hemisphere (green) have a mean smaller one.

jet  $p_T$  and thus can be considered as constant in terms of  $\alpha$

$$\sigma_{\text{intrinsic}}(\alpha) = c. \quad (\text{II.4.3})$$

This is not true for the imbalance part. It was found empirically that the  $\alpha$  dependence of the imbalance can be described by a linear function

$$\sigma_{\text{imbalance}}(\alpha) = q + m \cdot \alpha \quad (\text{II.4.4})$$

Folding two independent Gaussian functions results in a quadratic addition of the corresponding standard deviations  $\sigma_{\text{intr.}} \oplus \sigma_{\text{imb.}}$ .

$$\sigma_{\text{total}}(\alpha) = \sqrt{c^2 + q^2 + 2qm \cdot \alpha + m^2 \cdot \alpha^2}. \quad (\text{II.4.5})$$

In Fig. II.4.5, the  $\alpha$  dependence of the imbalance, the intrinsic resolution, and the total resolution is shown for two exemplary  $p_T^\gamma$  regions in simulated events. The measured intrinsic resolution and imbalance for various  $\alpha$  values are fitted with functions (II.4.3) and (II.4.4), respectively. The measured total resolution (black dots) is fitted with function (II.4.5). Here, only  $c$  and  $m$  are free parameters, whereas  $q$  is fixed to the value obtained from the imbalance fit. All contributions are well described by their fit functions. The grey line is the total resolution with the analytic expression of function (II.4.5) with the

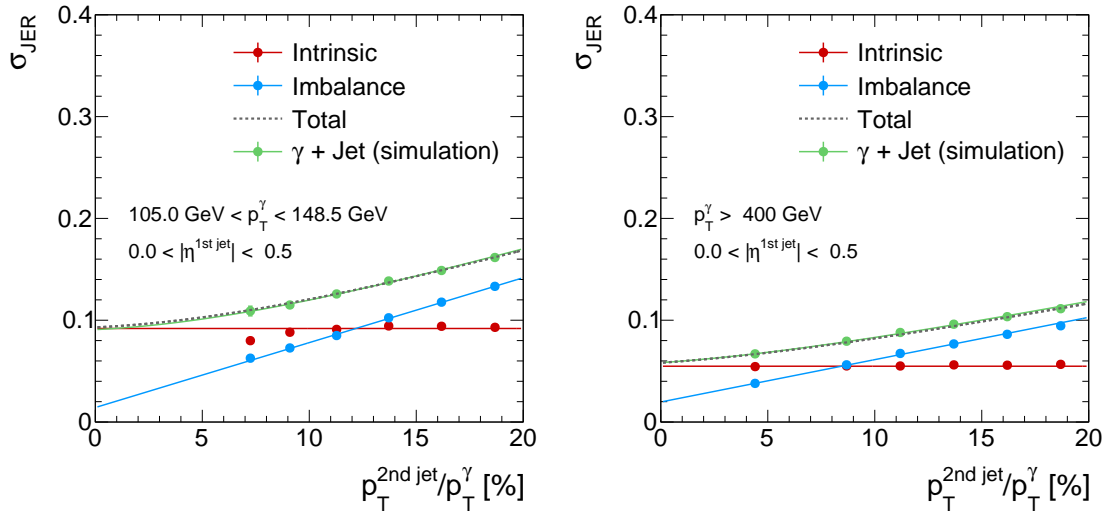


Figure II.4.5: The alpha dependency of the various parts of the resolution in the simulated events for  $83 \text{ GeV} < p_T^\gamma < 99 \text{ GeV}$  (left) and  $400 \text{ GeV} < p_T^\gamma$  (right). The total resolution (grey dotted line) is the addition in quadrature of the imbalance (blue line) and the intrinsic (red line) fit functions. It can be compared to the measured pseudo data (green dots/line).

parameters set to the fit values of the intrinsic and the imbalance fit.

It is apparent that the imbalance is not zero for  $\alpha = 0$ . This has two reasons. First and most important, only the photon and the parton are balanced in the transverse plane. But since the transverse momentum of a jet is defined as the sum of all particles' transverse momenta that are clustered into the jet cone, the jet  $p_T$  can be lower than the  $p_T$  of the original parton. This effect is called out-of-cone showering and leads to a residual imbalance between the photon  $p_T$  and the generator-level jet  $p_T$  at  $\alpha = 0$ . Second, also the photon  $p_T$  can be wrongly measured and spoil the residual imbalance  $q$ .

These two effects lead to a small discrepancy between the measured resolution (black) and the intrinsic resolution (red) also for zero second jet  $p_T$ . To correct for this effect,  $q$  is fixed to the value obtained from fitting the imbalance part of the resolution (Eq. (II.4.4)) and then only the fit parameter  $c$  is taken as the relevant resolution from the fit. Also for measured data,  $q$  is fixed to the value obtained from simulation. Figure II.4.6 shows the residual imbalance for two exemplary  $|\eta^{1\text{st jet}}|$  bins. It is almost stable and around 2% over the whole photon  $p_T$  range.

In Fig. II.4.7, the fitted intrinsic resolution in simulation is shown in the different photon  $p_T$  bins for two different  $|\eta^{1\text{st jet}}|$  regions. The resolution improves for increasing photon  $p_T$ . For the  $|\eta^{1\text{st jet}}| < 0.5$  region, the resolution is approximately 10% for  $p_T^\gamma \approx 100$  GeV and decreases to values around 6% for  $p_T^\gamma \approx 500$  GeV. The increasing statistical uncertainties for low photon  $p_T$  arise through the requirement of a maximal  $\alpha$  and a minimal  $p_T$  of the second jet. This reduces the numbers of events in the low photon  $p_T$  bins. For events with  $p_T^\gamma \lesssim 50$  GeV, it is not possible at all to fulfil both requirements at the same time.

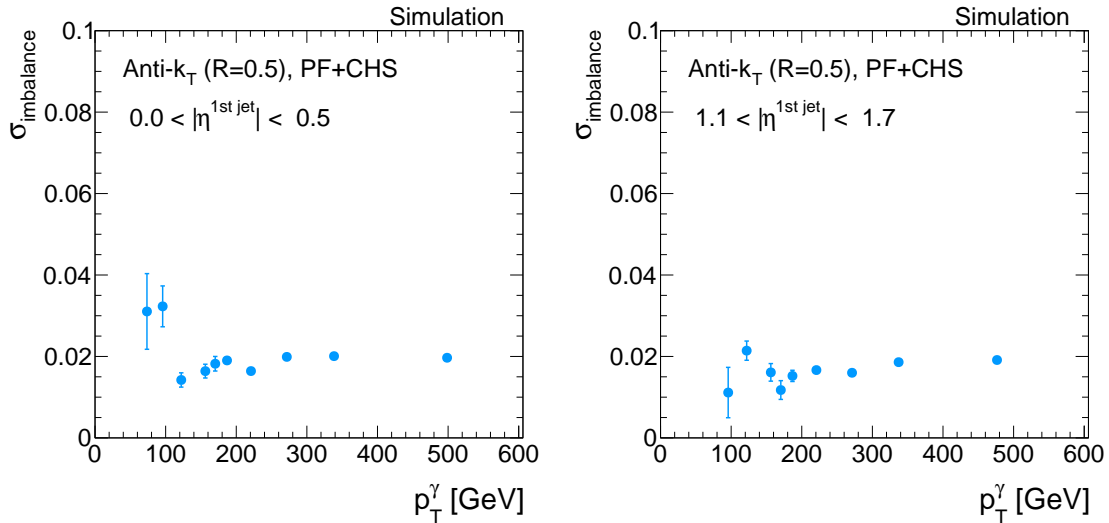


Figure II.4.6: Imbalance for  $|\eta^{1\text{st jet}}| < 0.5$  (left) and  $1.1 < |\eta^{1\text{st jet}}| < 1.7$  (right) in simulation.

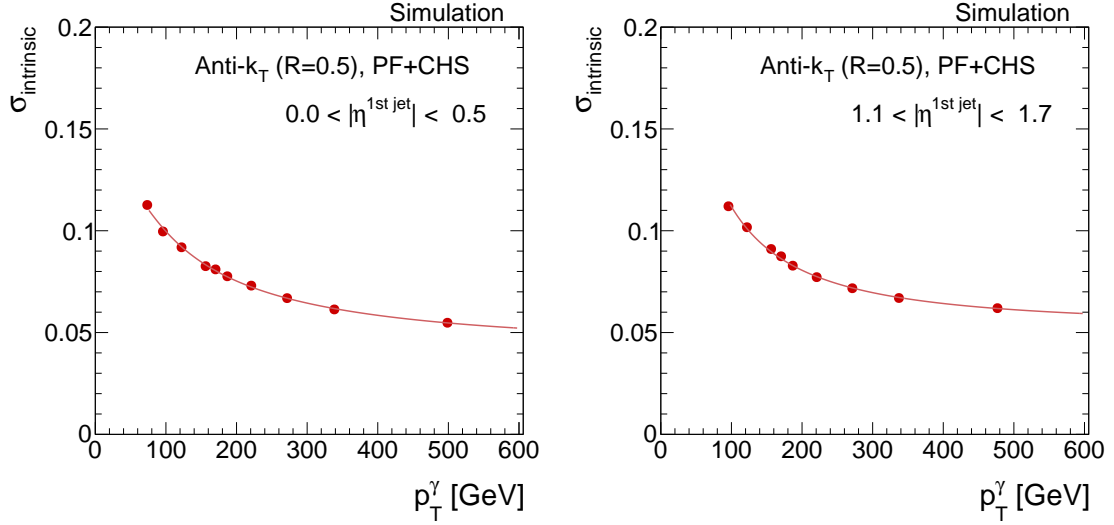


Figure II.4.7: Intrinsic resolution for  $|\eta^{1\text{st jet}}| < 0.5$  (left) and  $1.1 < |\eta^{1\text{st jet}}| < 1.7$  (right) in simulation.

653 The extrapolated intrinsic resolutions for the various photon  $p_T$  are fitted with the  
 654 following function

$$\sigma_{\text{JER}} = \sqrt{\text{sgn}(N) \cdot \frac{N}{p_T} + S^2 \cdot p_T^{M-1} + C^2} \quad (\text{II.4.6})$$

655 which was introduced for particle flow jets in [35]. It is an extended fit function compared  
 656 to the usual calorimeter resolution parametrisation to account for the higher resolution  
 657 due to tracking information.

658 Finally, in order to measure data-to-simulation scale factors  $\rho_{\text{res}}$  for the jet transverse-  
 659 momentum resolution, the measured resolution in data is divided by the resolution in  
 660 Monte Carlo simulation (MC)

$$\rho_{\text{res}} = \frac{\sigma_{\text{JER}}^{\text{data}}}{\sigma_{\text{JER}}^{\text{MC}}} \quad (\text{II.4.7})$$

661 It was found empirically, that this ratio is independent of  $p_T^\gamma$ , and can be fitted with a  
 662 constant. Thus, to account for differences in the data-to-simulation ratio for different  
 663 pseudorapidity ranges of the jet, the measurement of the scale factors is only done in bins  
 664 of  $|\eta^{1\text{st jet}}|$ .

665 How to adjust finally the jet transverse-momentum resolution in simulation to the mea-  
 666 sured resolution in data is well described in [42].

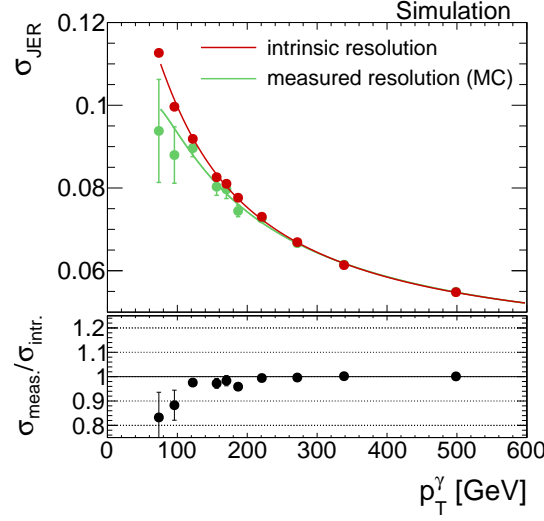


Figure II.4.8: Consistency check of the method: Comparison between the “measured” resolution evaluated with Eq. (II.4.5) and the intrinsic resolution from Eq. (II.4.3) in simulation.

### II.4.1 Validation of the method

The method is validated with simulated events. The bias of the method is shown in Fig. II.4.8 for the barrel region. It is evaluated as the ratio of the predicted intrinsic resolution by fitting Eq. (II.4.5) with  $q$  fixed to the value obtained by Eq. (II.4.4) over the intrinsic resolution directly obtained from the intrinsic response distribution  $p_T^{\text{reco. jet}}/p_T^{\text{gen. jet}}$ . The result is in good agreement with the expectation to better than 5% above 100 GeV and better than 1% above 200 GeV. Only for small  $p_T$ , larger deviations are observed, which are systematically lower than zero (up to 15%).

The residual bias of the method for small  $p_T^\gamma$  is stemming from two effects: First, the binning in  $p_T^\gamma$  and the momentum balance between the photon and the first two jets lead to a dependency of the first jet  $p_T$  on the second jet  $p_T$  and therefore alpha: For a fixed  $p_T^\gamma$ , the  $p_T$  of the first jet gets smaller for larger  $p_T^{2\text{nd jet}}$  in events where the second jet is in the leading jet hemisphere (see Fig. II.4.3), leading to a dependency of  $p_T^{1\text{st jet}} \propto -p_T^{2\text{nd jet}}$ . This effect is directly opposite for events with a second jet in the photon hemisphere. In these events, the first jet  $p_T$  gets larger for larger  $p_T^{2\text{nd jet}}$  and thus  $p_T^{1\text{st jet}} \propto p_T^{2\text{nd jet}}$  for fixed  $p_T^\gamma$ . As the resolution of the jet improves with higher jet  $p_T$  (see Fig. II.4.7), a dependency of the leading jet  $p_T$  on the second jet  $p_T$  directly leads to a dependency of the intrinsic resolution on the second jet  $p_T$ . In principle, as the effect is opposite for events in the different hemispheres, it should cancel out, when taking the weighted mean of the two hemisphere resolutions. But as the topology of a second jet in the leading jet hemisphere is much more frequent, a residual upward trend in the intrinsic resolution vs.

$\alpha$  is conserved.

The second source of the residual bias arises from the alpha definition  $\alpha = p_T^{2^{\text{nd jet}}}/p_T^\gamma$ . Because of the inclusion of  $p_T^\gamma$  in  $\alpha$  with  $\alpha \propto 1/p_T^\gamma$ , the high photon  $p_T$  events accumulate in the low alpha regions. As the selected events are almost balanced, a high  $p_T^\gamma$  is associated with a high jet  $p_T$ , thus also the high jet  $p_T$  events accumulate in the low alpha bins, leading to an upward trend in the intrinsic resolution vs.  $\alpha$ . This behaviour can be seen in the intrinsic resolution in Fig. II.4.5, where a small increase of the resolution to high  $\alpha$  can be seen. By fitting a horizontal line to the intrinsic resolution, this effect is averaged out. But the measured resolution with an additional free parameter can adopt this increase and result, therefore, in a y-intercept which is too small. For high photon  $p_T$  bins, this effect is less pronounced, as the slope of  $\text{JER}(p_T^\gamma)$  (see Fig. II.4.5) flattens out.

However, this is not of concern here, because the results of the measurement will be presented as resolution scale factors ( $\rho_{\text{res}}$ ), defined as the resolution measured in data divided by the resolution measured in Monte Carlo simulation (see Eq. (II.4.7)). Hence, a possible bias in the separate resolution measurements for data and simulation should cancel out. To prove this hypothesis, the simulated dataset is smeared with input values  $\rho_{\text{res}} = 1.1$  in all  $|\eta^{1^{\text{st jet}}}|$  bins. As done to determine the data-to-simulation ratio, the relative difference of the resolution measured in the smeared and in the non-smeared dataset is fitted with a constant over the photon  $p_T$  range. The resulting scale factors  $\rho_{\text{res}}$  should reproduce the input value of  $\rho_{\text{res}} = 1.1$ .

In Fig. II.4.9, the comparison of the input and output values is shown. In all  $|\eta^{1^{\text{st jet}}}|$  bins, the measurement of the scale factors reproduces the input factors within the statistical uncertainties. The deviation of the measured scale factors to the input value is less than 0.9% in all four  $|\eta^{1^{\text{st jet}}}|$  bins. Thus, the method is expected to hold also for the determination of the data-to-simulation ratio.

After the characterisation and estimation of the associated systematic uncertainties of the jet transverse-momentum resolution measurement with  $\gamma + \text{jet}$  events, the results of the measurement on  $\sqrt{s} = 8 \text{ TeV}$  data will be presented.



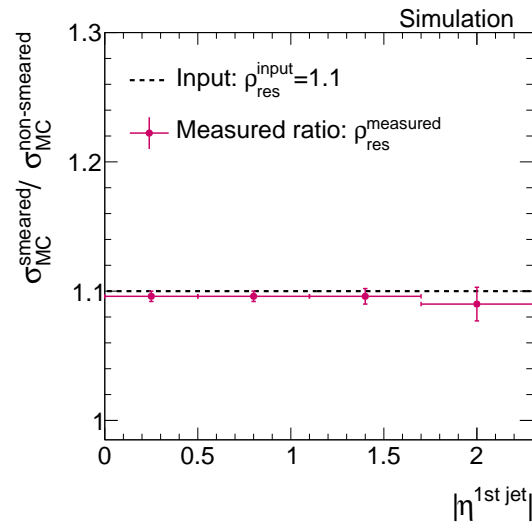


Figure II.4.9: Comparison of the resolution ratio  $\sigma_{\text{JER}}^{\text{smeared MC}} / \sigma_{\text{JER}}^{\text{non-smeared MC}}$  measured in simulated events with the input smearing factor  $\rho_{\text{res}} = 1.1$  in all four  $|\eta^{1\text{st jet}}|$  bins.

## II.5 Systematic uncertainties

Many systematic uncertainties of the jet transverse-momentum resolution measurement cancel out when focusing on the data-to-simulation ratio  $\sigma_{\text{JER}}^{\text{data}}/\sigma_{\text{JER}}^{\text{MC}}$ . In the following subsections, only uncertainties relevant for this ratio will be discussed.

For the final uncertainty, the single uncertainties are added in quadrature, resulting in relative uncertainties between 2.3% to 6.3% for the lowest and highest  $|\eta^{\text{1st jet}}|$  bin, respectively.

An overview of all systematic uncertainties can be found in Table II.5.1.

Table II.5.1: All relative systematic uncertainties on the data-to-simulation ratio  $\sigma_{\text{JER}}^{\text{data}}/\sigma_{\text{JER}}^{\text{MC}}$  listed by sources for the different  $|\eta^{\text{jet}}|$  bins.

	$ \eta^{\text{jet}} $			
	0.0 - 0.5	0.5 - 1.1	1.1 - 1.7	1.7 - 2.3
<b>Multijet contamination</b>	+2.0%	+2.0%	+2.3%	+2.5%
	−2.0%	−2.0%	−2.3%	−2.5%
<b>Simulation of flavor composition</b>	+0.9%	+0.9%	+0.8%	+0.6%
	−0.9%	−0.9%	−0.8%	−0.6%
<b>Simulation of out-of-cone showering</b>	+0.5%	+2.8%	+3.6%	+5.7%
	−0.5%	−2.8%	−3.6%	−5.7%
<b>Jet energy scale</b>	+0.6%	+0.6%	+0.6%	+0.7%
	−0.5%	−0.6%	−0.6%	−0.6%
<b>Pileup reweighting</b>	+0.1%	+0.1%	+0.1%	+0.2%
	−0.1%	−0.1%	−0.2%	−0.2%
<b>Total</b>	+2.3%	+3.6%	+4.4%	+6.3%
	−2.3%	−3.6%	−4.4%	−6.3%

## Uncertainty on the contamination with QCD-multijet events

Although the photon selection is very strict (see Section II.3.3), due to the huge QCD-multijet cross section, a countable fraction of dijet events can survive the selection with a jet misidentified as photon. This happens, when e.g. a jet hadronises to a  $\pi^0$  that decays to two photons which is sometimes not distinguishable from the isolated photon of a  $\gamma$ +jet event for the detector.

In principle, those dijet events have the same topology as  $\gamma$ +jet events. The two leading jets are also balanced apart from initial and final state radiation. Therefore, the method is generally expected to hold. A worsening of the resolution because of background contamination is only expected due to the mismeasurement of the  $p_T$  of the jet misidentified as photon, because only the energy of the  $\pi^0$  is counted and not the full energy. Another aspect is the different flavor composition of a QCD-multijet sample. Due to the different production mechanism, QCD-dijets are predominantly initiated by gluons while the leading jet in  $\gamma$  + jet events often stems from a light quark, cf. Fig. II.2.2. The number of particles after hadronisation is typically larger for gluon jets, hence the single particles are less energetic and out-of-cone showering is more pronounced. Since in this analysis the residual imbalance  $q$  is taken from the simulation where only a  $\gamma$ +jet sample is considered, it is not expected to accurately describe the residual imbalance in the data sample where also dijet events occur.

To investigate the impact of QCD-multijet contamination, a QCD-multijet sample, enriched in jets with a large electromagnetic fraction, is added to the  $\gamma$  + jet sample and weighted according to the cross section. Since the QCD-multijet sample has very large event weights leading to high statistical uncertainties in the measured jet transverse-momentum resolution, some selection criteria ( $\alpha < 0.4$  and  $\Delta\Phi > 2.7$ ) are relaxed in order to increase the statistical precision of the uncertainty estimation. Additionally, a rougher binning in  $\alpha$ ,  $p_T^\gamma$  and  $|\eta^{1\text{st jet}}|$  is applied.

The residual imbalance  $q$  of the resolution measurement including the QCD-multijet sample is fixed to the residual imbalance determined from the  $\gamma$  + jet only analysis to account for a possible error in the evaluation of the  $\sigma_{\text{JER}}^{\text{data}}/\sigma_{\text{JER}}^{\text{MC}}$  ratio where data is only compared to a  $\gamma$  + jet sample.

In Fig. II.5.1, the resolution measured when using both the  $\gamma$ +jet and the QCD-multijet sample is compared to the resolution measured only with the  $\gamma$ +jet sample. It can be seen, that the resolution is worse for low  $p_T^\gamma$  when considering QCD-multijet contamination.

The impact on the data-to-simulation ratio is estimated by adding the QCD-multijet sample on top of the  $\gamma$  + jet sample and redoing the evaluation of the scale factors. The resulting uncertainties vary between 2.0 – 2.5% for the different  $|\eta^{1\text{st jet}}|$  regions (cf. Table II.5.1).

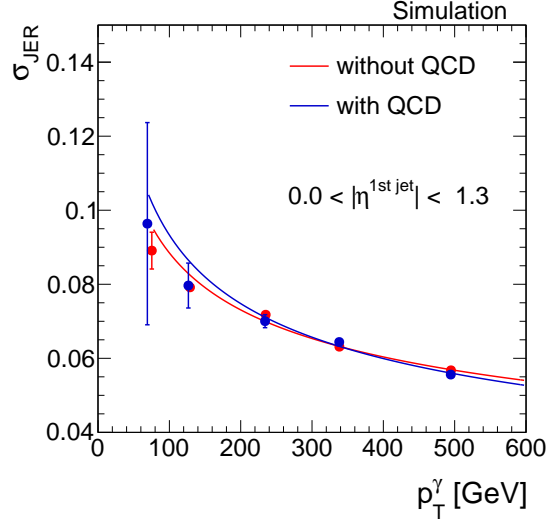


Figure II.5.1: The jet transverse-momentum resolution measured in simulation for  $|\eta^{1\text{st jet}}| < 1.3$  with (blue) and without (green) a QCD-multijet sample added to the  $\gamma + \text{jet}$  sample.

## Uncertainty on the flavor composition in simulation

A possible difference among the resolution of different jet flavors (caused by e.g. more pronounced out-of-cone showering of gluon jets) should in principle not play a role for the data-to-simulation scale factors  $\rho_{\text{res}}$  as long as the flavor composition of the data and simulation samples is the same.

To account for possible discrepancies in the flavor composition between data and simulation, the gluon and quark flavor fractions of the simulated sample are varied by 10%.

To estimate the effect of different flavour compositions, the resolution in simulation is separately evaluated for quarks ( $\sigma_{\text{JER}}^{\text{quarks}}$ ) and gluons ( $\sigma_{\text{JER}}^{\text{gluons}}$ ). There are various definitions used in the CMS collaboration how to assign the underlying generator-level quark/gluon flavor to a jet. In this measurement the so-called “algorithmic” flavor definition is used which classifies b- or c-jets from gluon splitting as b- or c-quarks (see Appendix ?? for more details on this definition).

Figure II.5.3 shows the differences in the resolution for all flavors separately for  $|\eta^{1\text{st jet}}| < 1.3$ . The composition in the simulated PYTHIA  $\gamma + \text{jet}$  sample is around 60% light quarks and 20% to 35% gluons (see Fig. II.5.2). The missing fraction is mainly made up out of charm quarks.

The resolution for gluon and light quark jets is comparable for small  $p_{\text{T}}^{\gamma}$  and gets larger for high  $p_{\text{T}}^{\gamma}$ . Since the transverse momentum of neutrinos is counted into the generator-level jet  $p_{\text{T}}$ , the resolution of charm and bottom quarks is therefore shifted to larger resolution values (left part of Fig. II.5.3). This is not the case, if the neutrino  $p_{\text{T}}$  is not

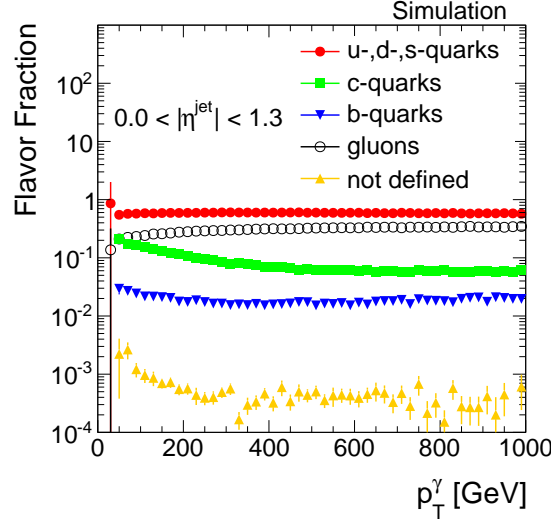


Figure II.5.2: The flavor composition in the  $\gamma + \text{jet}$  sample in the barrel region of the detector. The “algorithmic” flavor definition is used (see Appendix ?? for more details).

783 added to the generator-level jet  $p_T$ , as can be seen in Fig II.5.3 (right). However, for the  
 784 here presented measurement is does not play a role whether the neutrino  $p_T$  is or is not  
 785 added to the generator-level jet  $p_T$ , because in case it is not included into the intrinsic  
 786 response the long right tail of the response function for b- and c-quarks is then transferred

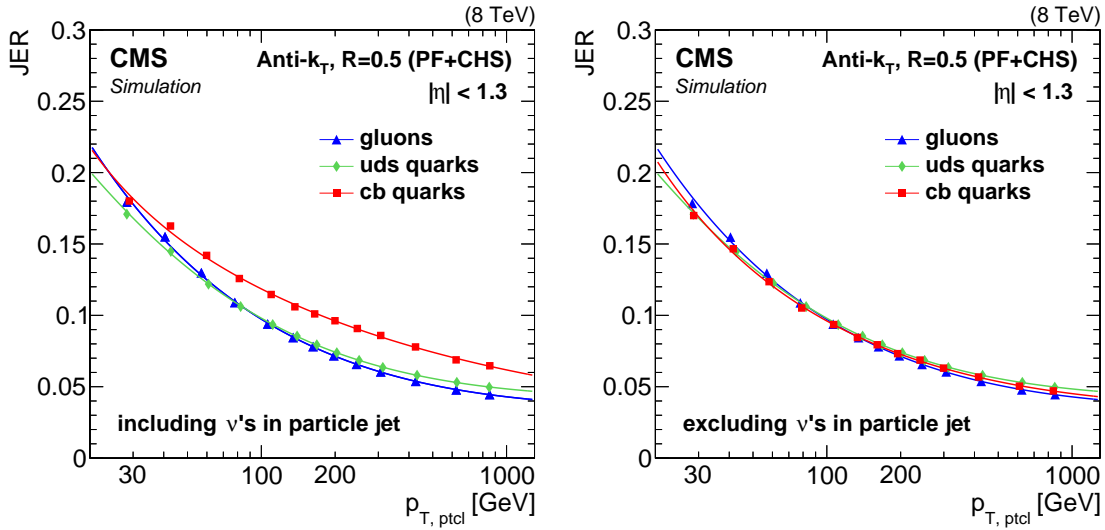


Figure II.5.3: The intrinsic resolution  $\sigma_{\text{intr.}}$  for  $|\eta^{\text{1st jet}}| < 1.3$  for different jet flavors with (left) and without (right) including the neutrinos in the generator-level jet. Here, JER refers to  $\sigma_{\text{intr.}}$ , and  $p_{T,\text{ptcl}}$  to the generator-level jet  $p_T$ .

to the imbalance response. Thus, the right tail of b- and c-quarks does anyway enter the jet transverse-momentum resolution measurement with  $\gamma + \text{jet}$  events, either in the intrinsic or in the imbalance response.

The weighted mean of the quark and the gluon resolution is then taken to estimate the resolution for different flavor compositions, such that the flavor fractions are varied by 10%. Finally, the constant fit to the data-to-simulation ratio  $\sigma_{\text{JER}}^{\text{data}}/\sigma_{\text{JER}}^{\text{MC}}$  is reevaluated, leading to a final systematic uncertainty between 0.6 – 0.9%.

## Uncertainty on the simulation of out-of-cone showering

Another source of uncertainty is the use of information from Monte Carlo simulation by determining the residual imbalance  $q$  from the simulated  $\gamma + \text{jet}$  sample (Eq. (II.4.5)).

Since it cannot be expected that out-of-cone showering is well modelled in simulation, possible differences between real and simulated out-of-cone showering are estimated by the evaluation of the ratio  $\sigma_{\text{JER}}^{\text{data}}/\sigma_{\text{JER}}^{\text{MC}}$  using different jet radii of the jet reconstruction algorithm.

For the primary analysis, jets reconstructed by the Anti- $k_t$  algorithm with a radius of  $R = 0.5$  are used (AK5-jets). In order to evaluate the systematic uncertainty on the out-of-cone showering simulation, the measurement of  $\rho_{\text{res}}$  redone with jets reconstructed with a jet radius of  $R = 0.7$  (AK7-jets).

The data-to-simulation ratio is in all  $|\eta^{\text{1st jet}}|$  bins larger for AK7-jets, resulting in uncertainties between 0.5 – 5.7%. The uncertainty on the simulation of out-of-cone showering is thereby the largest systematic uncertainty of this measurement.

## Uncertainty on the jet energy scale

A further uncertainty arises from the correction of the jet energy scale. The transverse momentum of each jet is corrected in order to have uniform response over the full  $\eta^{\text{jet}}$ , and  $p_{\text{T}}^{\text{jet}}$  range [43]. In simulation, it is additionally corrected to account for data-simulation differences. The latter correction can be a important for the evaluation of the data-to-simulation ratio  $\rho_{\text{res}}$ . Thus, the uncertainties on the correction factors that are only applied to the simulated samples are varied up and down within their  $1\sigma$ -uncertainties.

The effect of the jet  $p_{\text{T}}$  variation on the data-to-simulation ratio is of minor importance and range between 0.5 – 0.7%.

## Uncertainty on the pileup reweighting

Finally, an uncertainty due to the adjustment of the simulated events to the pileup distribution in data is evaluated.

To account for this uncertainty, the effect of a 5.0% up- and downward variation of the minimum-bias cross section (69.4 mb) on the resolution is evaluated, following the recommended procedure from [?]. The resulting uncertainties are almost negligible and range between 0.1 – 0.2%.

## II.6 Results

The data-to-simulation resolution scale factors  $\rho_{\text{res}}$  are determined in  $19.7 \text{ fb}^{-1}$  of  $pp$ -collision data at  $\sqrt{s} = 8 \text{ TeV}$  with the methodology described in Chapter II.4. In each  $\alpha$ -,  $p_{\text{T}}^{\gamma}$ - and  $|\eta^{1\text{st jet}}|$ -bin, the width of the 99% truncated response histogram is determined in simulation and data. Afterwards, the extrapolation to zero additional jet activity is carried out, by fixing the imbalance  $q$  in simulation and in data to the value extracted from the imbalance extrapolation in simulation. Exemplary extrapolations for the imbalance and the total resolution in data and simulation are shown in Fig. II.6.1.

The full set for each  $p_{\text{T}}^{\gamma}$  and  $|\eta^{1\text{st jet}}|$  bin can be found in Appendix ??.

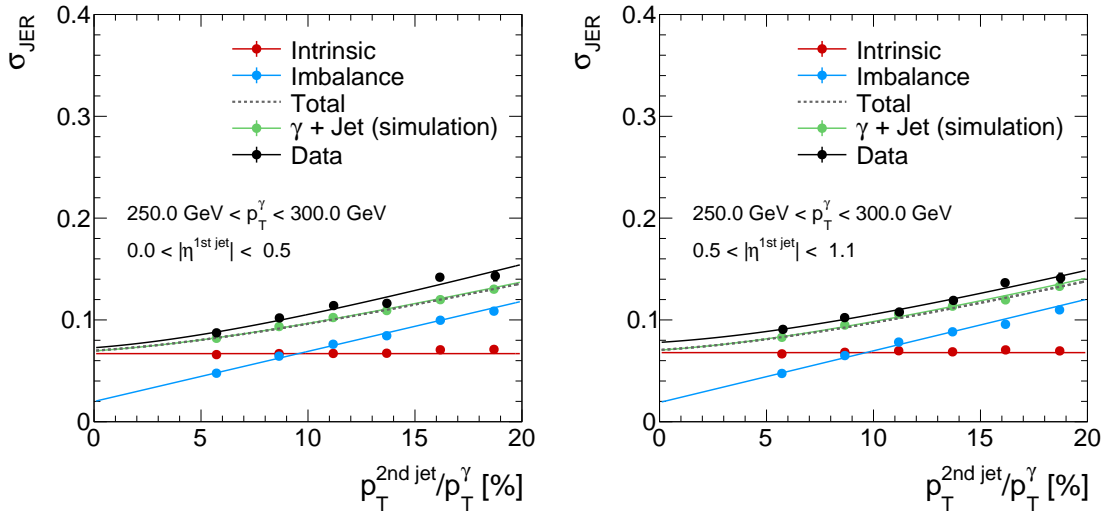


Figure II.6.1: Two examples of the alpha dependency of the measured jet transverse-momentum resolution in data (black dots), in simulation (green dots) and of the intrinsic (red dots) and the imbalance (blue dots) part of the resolution in simulated events. All resolutions are fitted with the corresponding functions introduced in Chapter II.4 (Eqs. (II.4.3)- (II.4.5)). The total resolution (grey dotted line) is the addition in quadrature of the imbalance (blue line) and the intrinsic (red line) fit functions.

Finally, the extracted resolutions in data and simulation in every  $p_T^\gamma$  bin are divided  
and a horizontal fit is applied to this ratio

$$\frac{\sigma_{\text{JER}}^{\text{data}}}{\sigma_{\text{JER}}^{\text{MC}}} (p_T^\gamma) .$$

In Fig. II.6.2, the results for all four  $|\eta^{1\text{st jet}}|$ -ranges are depicted. The  $\chi^2/\text{NDF}$ -values for  
the four fits vary between 0.23 and 2.53. Thus, a horizontal fit is justified, and one value  
for every  $|\eta^{1\text{st jet}}|$ -bin will be reported.

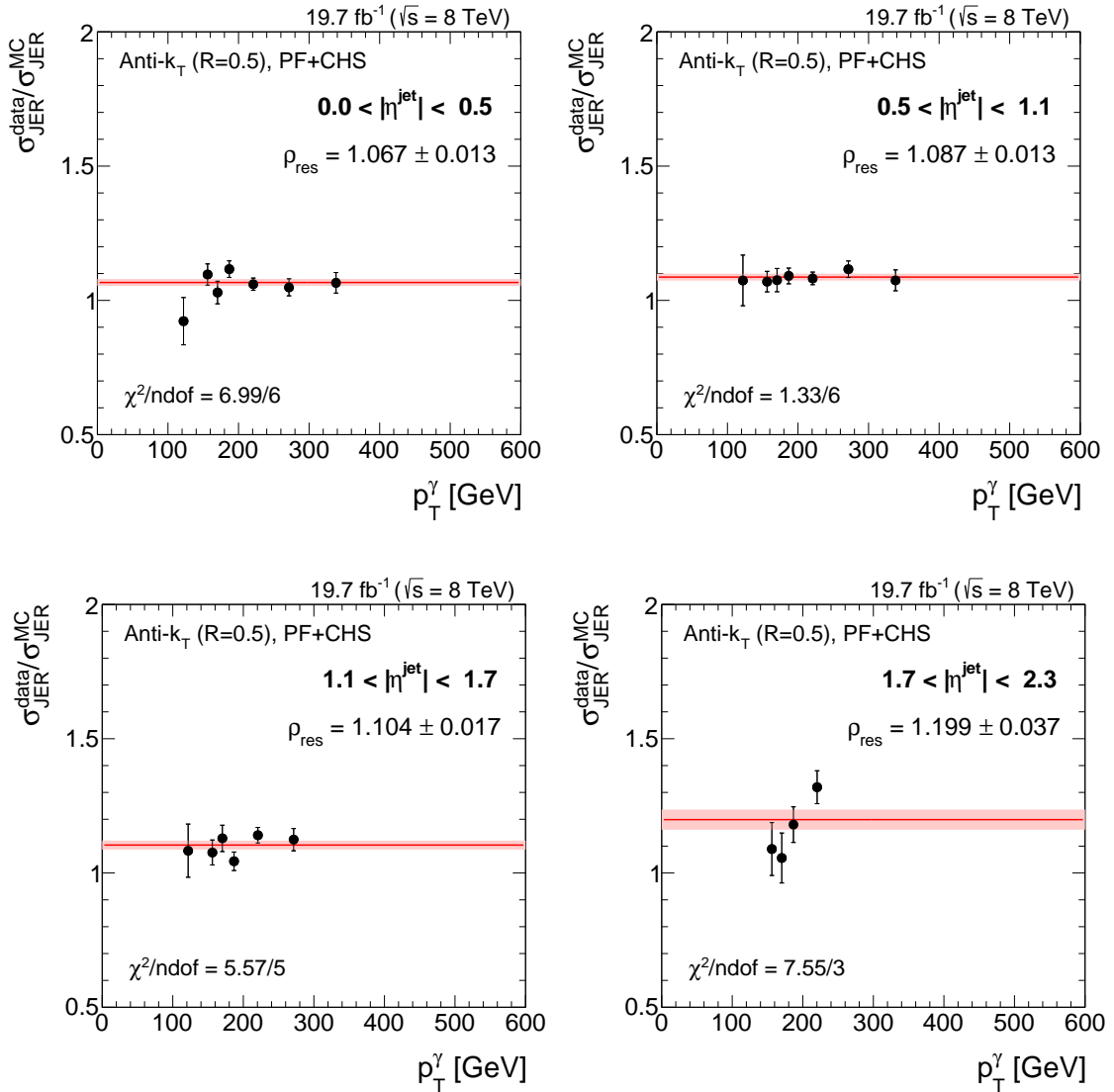


Figure II.6.2: Data-to-simulation resolution ratios (black dots), fitted with a horizontal line (red line) for four different  $|\eta^{\text{jet}}|$ -ranges. The fit uncertainties are depicted with light red error bands.



Table II.6.1: Data-to-simulation resolution scale factors  $\rho_{\text{res}}$  with statistical and systematic uncertainties.

$ \eta^{\text{jet}} $	$\rho_{\text{res}}$	stat.	sys.
0.0 – 0.5	1.067	$\pm 0.013$	$^{+0.025}_{-0.024}$
0.5 – 1.1	1.087	$\pm 0.013$	$^{+0.039}_{-0.039}$
1.1 – 1.7	1.104	$\pm 0.017$	$^{+0.049}_{-0.049}$
1.7 – 2.3	1.199	$\pm 0.037$	$^{+0.075}_{-0.075}$

All fit results are greater than one which means that the resolution in data is in all bins worse compared to the resolution in simulation. The values of the fits range from 1.067 (for the first  $\eta^{\text{jet}}$ -bin) to 1.199 (for the last  $\eta^{\text{jet}}$ -bin).

The systematic uncertainties are evaluated as described in the previous chapter. The single uncertainties are taken as upper and lower boundary of the 68% uncertainty band and are added in quadrature to get the total systematic uncertainty. Table II.6.1 summarises the data-to-simulation ratio results determined with data collected during the year 2012 with their statistical and systematic uncertainties. The visualised result can be found in Fig. II.6.3.

Though the  $\gamma + \text{jet}$  analysis is known to be capable to produce highly precise results, the systematic uncertainties are still dominating. This is mainly caused by the uncertainty on the simulation of out-of-cone showering. The statistical limitation of this analysis is due to the collected data at the CMS detector. The number of simulated events is roughly eight times larger.

### II.6.1 Comparison to 2011 measurement

A comparison of the data-to-simulation resolution scale factors  $\rho_{\text{res}}$  between this analysis and the results of 2011 which were determined from a dijet data sample [42] can be found in Fig. II.6.4.

It can be seen, that throughout the whole  $\eta^{\text{jet}}$ -range the data-to-simulation are systematically larger for the result in 2011.

Comparing the precision of both measurements, the  $\gamma + \text{jet}$  analysis is for all  $\eta$ -bins more precise than the analysis done with dijet events. This is due to the smaller systematic

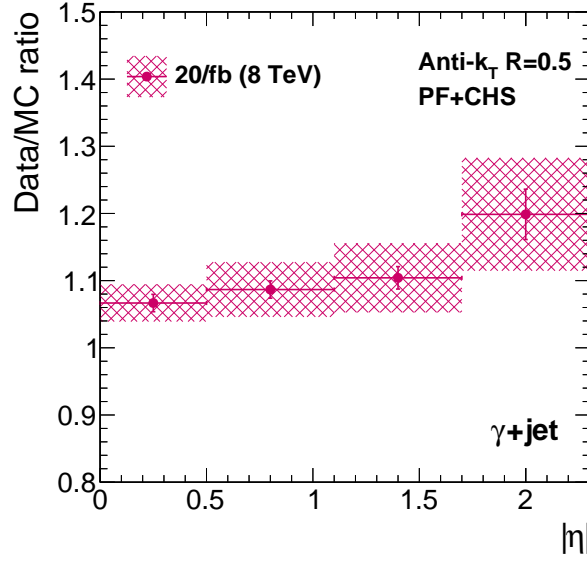


Figure II.6.3: The measured data-to-simulation resolution ratio in  $\gamma + \text{jet}$  events using data recorded in the year 2012. The red band depicts the total uncertainty whereas the error bars show the statistical uncertainty only.

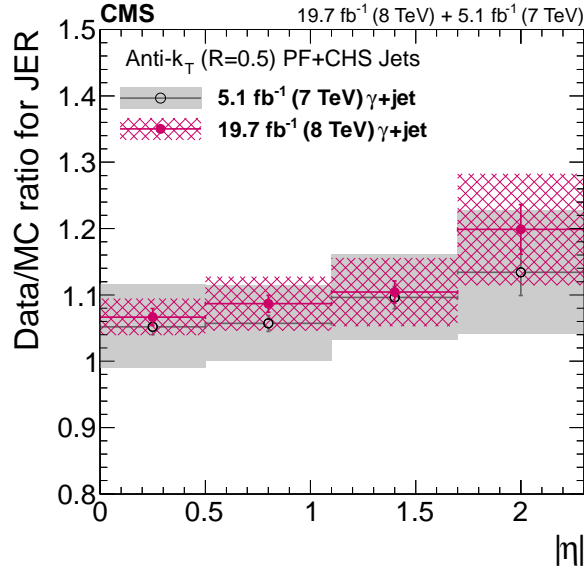


Figure II.6.4: FIXME (update this plot): Data-to-simulation jet  $p_T$  resolution ratio determined from  $\gamma + \text{jet}$  events from 2012 compared to dijet results from 2011. The grey and magenta bands correspond to the full uncertainties, whereas the error bars depict the statistical uncertainties only.

uncertainties of the  $\gamma + \text{jet}$  analysis which compensates for the better statistical precision of the QCD-multijet sample due to the large cross section.

### II.6.2 Comparison to 2012 dijet measurement

In 2012, also a jet  $p_T$  resolution measurement was conducted with the help of dijet events [43, 44]. A comparison of the here presented measurement using  $\gamma + \text{jet}$  events to the measurement with dijet events can be found in Fig. II.6.5. Both measurements are compatible within their uncertainties. It can be seen that the statistical precision is much better for the measurement with QCD-multijet events because of the larger cross section. The systematic uncertainties are of comparable size for small pseudorapidity bins and are larger for high  $|\eta^{\text{jet}}|$  in the  $\gamma + \text{jet}$  measurement. This is due to the uncertainty on the simulation of the out-of-cone showering. This uncertainty plays a smaller role in the dijet measurement (between 0.4% and 1.5%) as the effect by out-of-cone showering partly cancels out in case of two balanced jets.

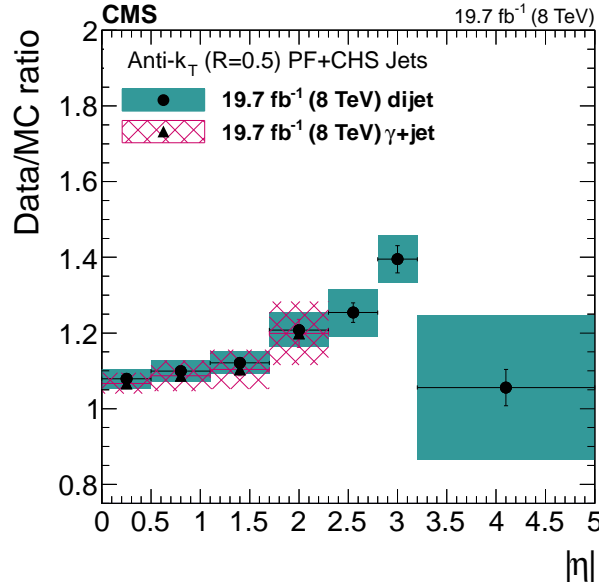


Figure II.6.5: FIXME: Data-to-simulation jet  $p_T$  resolution ratio determined from  $\gamma + \text{jet}$  events from 2012 compared to dijet results from 2012. The blue and magenta bands correspond to the full uncertainties, whereas the error bars depict the statistical uncertainties only.

## II.7 Discussion and conclusion

The difference between data and simulation of the jet-transverse momentum resolution is an important input for many analyses at CMS, among them searches for physics beyond the Standard Model using QCD-multijet events, e. g. [32].

In the here presented analysis, the first measurement of the data-to-simulation resolution ratio  $\sigma_{\text{JER}}^{\text{data}}/\sigma_{\text{JER}}^{\text{MC}}$  using  $\gamma + \text{jet}$  events with  $19.7 \text{ fb}^{-1}$   $pp$ -collision data at  $\sqrt{s} = 8 \text{ TeV}$  collected in 2012 at the CMS detector was carried out. For this purpose, the methodology introduced in [35, 36] was further developed. To take account of the double peak structure when applying an exclusive binning in the variable  $\alpha$  which measures the additional jet activity in the event, the event selection explicitly distinguishes the case of parton radiation in the leading jet/photon hemispheres. This change in methodology is introduced for the first time by this measurement.

The resolution in data is found to be systematically larger than in simulation throughout the investigated  $\eta^{\text{jet}}$  plane. A possible  $p_{\text{T}}^{\gamma}$  dependence of the resolution scale factors  $\rho_{\text{res}}$  is not visible. Thus, the ratio is parametrised with a constant per  $\eta^{\text{jet}}$ -bin.

The relative difference of the data resolution ranges from  $\sim 7\%$  to  $\sim 20\%$  for  $|\eta^{\text{jet}}|$  between  $0.0 - 0.5$  and between  $1.7 - 2.3$ , respectively, with total statistical and systematic uncertainties between  $3\%$  and  $8\%$ .

The here presented measurement serves as a cross-check measurement to the jet  $p_{\text{T}}$  resolution ratio result using dijet events [43, 44]. Both measurements are compatible within their statistical and systematic uncertainties.

For a future measurement, a reduction of the uncertainties is desirable. Since the systematic uncertainty is still dominating, most notably the uncertainty on the simulation of out-of-cone showering, an improved evaluation of the out-of-cone showering uncertainty could significantly improve the precision of the data-to-simulation ratio  $\sigma_{\text{JER}}^{\text{data}}/\sigma_{\text{JER}}^{\text{MC}}$ . A better evaluation can be possibly achieved by a better understanding, whether the difference of  $\rho_{\text{res}}$  using clustered jets within a radius of  $0.7$  and  $0.5$  is only originating from out-of-cone showering effects. Since the simulation of out-of-cone showering should in principal only enter the result by the residual imbalance  $q$ , an overestimation by the here presented method might be possible.

Furthermore, an increase in the statistical precision is desirable to allow for the coverage of the measurement of the resolution scale factors in the high pseudorapidity regions which

908 has not been possible so far.



909

## **Part III**

910

# **A search for highly ionising, short tracks at the CMS detector**

911





## III.1 Motivation

Supersymmetry is able to offer solutions to many unexplained phenomena in astrophysics and can solve many of the shortcomings of the Standard Model of particle physics (see Section ??). While SUSY has been studied at previous particle colliders including Tevatron and LEP [45, 46], the LHC with its high centre-of-mass energy offers a unique opportunity to investigate SUSY models with high sparticle masses that were not accessible in previous experiments.

Therefore, a variety of searches were hunting for SUSY during Run I of the LHC in 2011 and 2012. Proton-proton collision data from the CMS and ATLAS experiments were analysed with a strong focus on the search for SUSY in the strong production sector (e.g. [32, 33, 47]). As a consequence, wide, previously unexplored regions of SUSY parameter space are already excluded. However, due to the unknown mechanism of supersymmetry breaking, the most general parametrisation of the Minimal Supersymmetric Standard Model (MSSM) introduces over 100 new parameters and thus opens up an incredibly large phenomenological space. Therefore, SUSY models can lead to a plethora of possible signatures at particle colliders, many of which could not - or not fully - be explored.

A very interesting signature occurs when sparticles live long enough to travel through a part or the whole detector before decaying. This is possible for SUSY models with compressed spectra, in which a sparticle can be long-lived because of phase-space suppression (see Section ??). In Supersymmetry, such a mass-degeneracy naturally occurs if the wino mass parameter ( $M_2$ ) is smaller than the bino ( $M_1$ ) and higgsino ( $\mu$ ) mass parameters. In this case, the lightest chargino ( $\tilde{\chi}_1^\pm$ ) and the lightest neutralino ( $\tilde{\chi}_1^0$ ) are both wino-like and their mass gap is fully determined by higher loop corrections (see Section ??). Therefore, they are almost mass-degenerate and the chargino is long-lived.

Such scenarios can be very interesting from a cosmological perspective as the wino-like lightest supersymmetric particle,  $\tilde{\chi}_1^0$ , can serve as a plausible Dark Matter candidate [48, 49]. While it is not possible to explain the full relic density with thermally produced wino-like neutralinos for  $m_{\tilde{\chi}_1^0} \lesssim 3 \text{ TeV}$ , neutralinos can still be the dominant part if they are non-thermally produced via the decay of an almost decoupled particle [50, 51]. Additionally, these scenarios are well motivated by Supersymmetric models with anomaly-mediated SUSY breaking (AMSB) [52, 53], where the LSP is almost always the wino-like lightest neutralino and the mass gap between the neutralino and chargino is typically between 140 MeV and 200 MeV [54].

SUSY scenarios with nearly mass-degenerate particles have two distinctive phenomenological properties that require a very different search strategy compared to general SUSY searches. First, because of the mass-degeneracy, the remaining decay product (e. g. a pion) is very soft in  $p_T$ , making it hard to detect. Since the other decay product, the neutralino, is only weakly interacting, it is very difficult to identify charginos via their decay products. Second, as the chargino is long-lived, it may traverse several detector layers before decaying. Thus, there is the possibility of reconstructing the chargino itself, e. g. as a reconstructed track in the tracker system.

Despite the exotic signatures of supersymmetric models with nearly mass-degenerate  $\tilde{\chi}_1^\pm$  and  $\tilde{\chi}_1^0$ , current CMS searches are already sensitive over a very broad range of lifetimes. The exclusion power of existing SUSY searches can be assessed by interpreting their results in terms of the fraction of excluded parameter points in the phenomenological MSSM (see Section ?? for an introduction to the pMSSM). The results of such a study which has been performed in [55] are shown in Figure III.1.1. It can be seen that general SUSY searches (blue area) are sensitive to shorter chargino lifetimes ( $c\tau \lesssim 10$  cm). Due to technical reasons<sup>1</sup>, the general SUSY searches were never interpreted in the context of SUSY models with longer chargino lifetimes. Two existing searches, the search for long-lived charged particles [56] and the search for disappearing tracks [55] focus on long and intermediate chargino lifetimes, respectively. These two searches (purple and red areas) are sensitive to chargino lifetimes of  $c\tau \gtrsim 35$  cm. Taken together, the existing searches exclude a large fraction of pMSSM points at different chargino lifetimes. However, there is a gap between the general SUSY searches and the search for disappearing tracks that is not accessible by any of the existing searches.

The here presented analysis aims at targeting this gap by optimising the search strategy for charginos with intermediate lifetimes of  $10 \text{ cm} \lesssim c\tau \lesssim 40 \text{ cm}$ . The targeted optimisation strategy is a combination of the strategies used in the search for long-lived charged particles [56] and the search for disappearing tracks [55]. While in [56], the high ionisation losses of hypothetical new massive particles is exploited, it does not take into account whether its reconstructed track is disappearing. In [55], the disappearance of the track is utilised but it does not incorporate the large ionisation losses into the search. Additionally, neither of the search does take into account the possibly very short tracks of early decaying charginos.

Thus, the here presented search is the first analysis at CMS combining the two signature

---

<sup>1</sup>The pMSSM interpretation relied on the use of fast simulation techniques which are not capable of simulating charginos with lifetimes  $c\tau > 1$  cm.

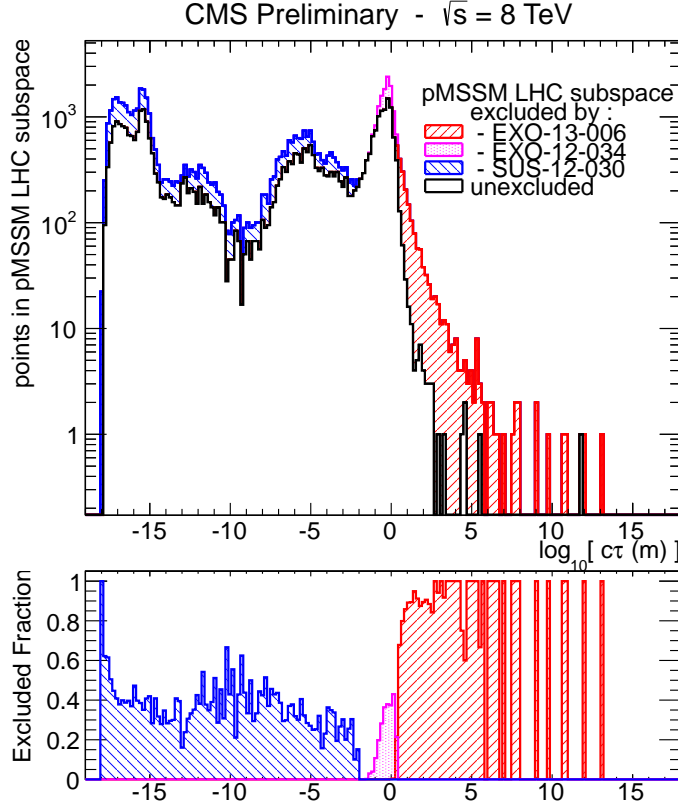


Figure III.1.1: The number of excluded pMSSM points at 95% C.L. (upper part) and the fraction of excluded pMSSM points (bottom part) vs. the chargino lifetime for different CMS searches. Red area: the search for long-lived charged particles [56], Purple area: the search for disappearing tracks [55], Blue area: a collection of various general SUSY searches [57] The black line indicates the unexcluded pMSSM parameter points. The sampling of the parameter space points was done according to a prior probability density function which takes pre-LHC data and results from indirect SUSY searches into account (see [58] for further details). Taken from: [59].

983 properties that are highly distinctive for charginos with intermediate lifetimes: first, the  
 984 characteristically high ionisation losses of heavy charginos; second, short reconstructed  
 985 tracks due to chargino decays early in the detector.

986 The associated challenges and the general search strategy of this analysis will be pre-  
 987 sented in the next section.

## III.2 General search strategy

At the LHC, there are several possible chargino production channels. Chargino pairs can be produced through a photon or a  $Z$ -boson exchange. The chargino then decays via a virtual  $W$ -boson to the lightest neutralino and a fermion pair (e.g. a pion). This process is illustrated in the Feynman diagram in Fig. III.2.1. Other possible chargino pair production channels include the exchange of a supersymmetric Higgs boson or a  $t$ -channel squark exchange (Fig. III.2.2).

Apart from pair production, charginos can be produced via the chargino neutralino production channel. On tree-level, there exist two production mechanisms: the  $s$ -channel  $W$ -boson exchange and the  $t$ -channel squark exchange (Fig. III.2.3).

Alternatively, charginos can be produced via strong production modes, i.e. in cascade decays of new heavy particles, such as gluinos or squarks. In the here presented search, the focus is, however, put on the electroweak production channels: chargino-pair and chargino-neutralino production.

When searching for supersymmetric models with long-lived  $\tilde{\chi}_1^\pm$ , the strategy is of course highly dependent on the actual lifetime of the chargino. For long lifetimes, the chargino

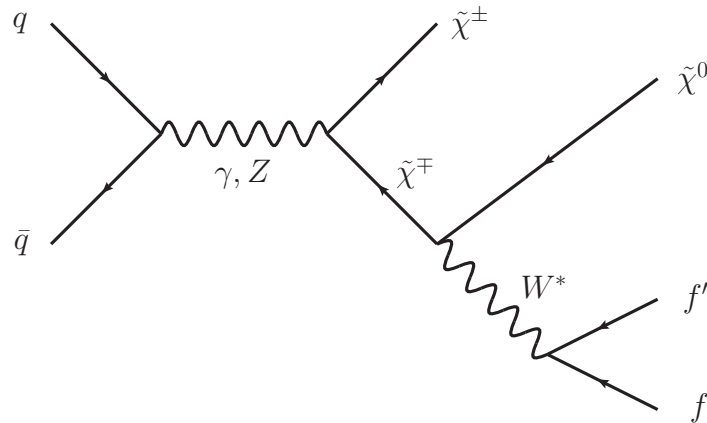


Figure III.2.1: Feynman diagram of chargino pair production via gamma or  $Z$ -boson exchange and the subsequent decay via a virtual  $W$ -boson.

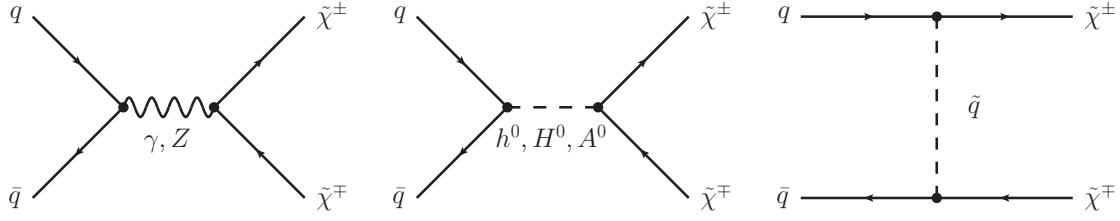


Figure III.2.2: Main tree-level diagrams for chargino pair production.

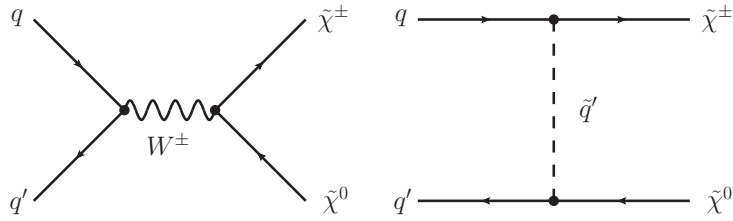


Figure III.2.3: Main tree-level diagrams for chargino neutralino production.

can reach the muon chambers and can be reconstructed as a muon even despite a longer time-of-flight [60]. For lower lifetimes, the chargino can already decay inside the detector (e. g. the tracker), and can hence not be reconstructed as a muon but leads to an isolated, potentially disappearing track in the tracker. The detector signatures of these two scenarios are visualised in Fig. III.2.4, where simulated chargino-chargino events are shown in a cross-sectional view of the CMS detector. In the left picture of Fig. III.2.4, both charginos are reconstructed as muons, which can be seen in the energy deposition in the muon chambers. In the middle and right pictures both charginos have a lower lifetime of  $c\tau = 0.5\text{ m}$  and thus are only visible as tracks in the tracker, where both trajectories end inside the silicon strip tracker. Since this analysis targets a search for Supersymmetry with charginos of lifetimes between  $c\tau \approx 10\text{ cm} - 40\text{ cm}$ , the charginos decay rather early in the detector, even in the inner layers of the tracker. Thus, the signature of chargino events consists of isolated, short tracks and the signatures of the decay products, i. e. of a neutralino and a fermion pair.

In case of R-parity conservation, one of the chargino decay products, the neutralino, is stable and weakly interacting, thus traversing the detector without leaving any further signature.

The signature of the other decay product, the fermion pair, can in principle be used to select chargino events. However, for mass-degenerate charginos, it can be very hard or even impossible to detect these fermions as will be explained in detail in the next paragraph.

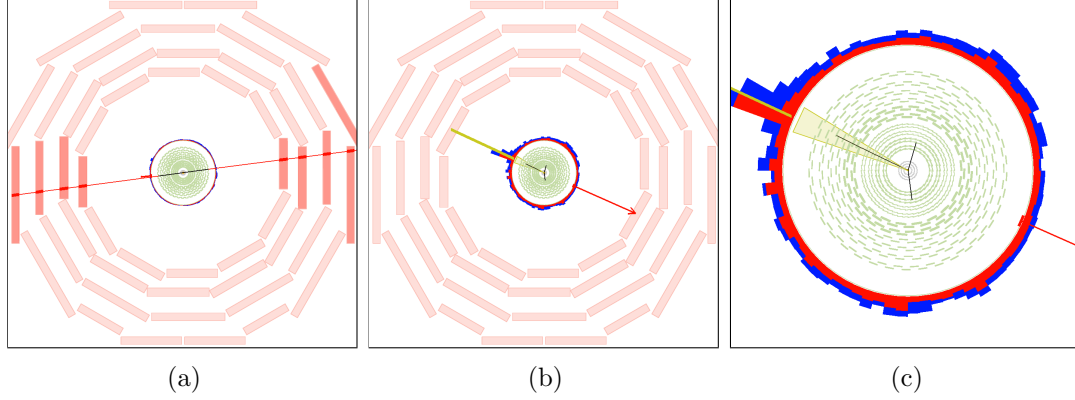


Figure III.2.4: Visualisation of possible signatures of a chargino pair produced with a lifetime of  $c\tau = 10$  m (a) and a lifetime of  $c\tau = 0.5$  m (b and c). The muon chambers are the outer layers of the detector and are depicted as red boxes. The black lines represent the reconstructed chargino tracks. The right picture is a zoom of the picture in the middle. Here, only the cross-section of the tracker (green wavy lines for the strip and grey lines for the pixel) is displayed. The red arrow shows the missing transverse energy in the event. The red (blue) towers correspond to the energy deposition in the ECAL (HCAL).

First of all, the fermionic decay product (e. g. a pion) can usually not be reconstructed because it does not origin from the primary vertex. Secondly, it is very low in momentum because of the mass-degeneracy between  $\tilde{\chi}_1^\pm$  and  $\tilde{\chi}_1^0$ . The typical momentum of a pion originating from a chargino to neutralino decay in the  $\tilde{\chi}_1^\pm$  rest frame is of the order

$$p_\pi \sim \sqrt{\left(m_{\tilde{\chi}_1^\pm} - m_{\tilde{\chi}_1^0}\right)^2 - m_\pi^2}. \quad (\text{III.2.1})$$

For a mass gap between  $\tilde{\chi}_1^\pm$  and  $\tilde{\chi}_1^0$  of  $\Delta m = 150$  MeV, the pt distribution of the resulting pion peaks at  $\sim 100$  MeV and ends at  $p_T \sim 400$  MeV (Fig. III.2.5).

If the transverse momentum of a particle is very low, the particle trajectory is much more bended compared to a particle with higher  $p_T$  (see Fig. III.2.6 for illustration). Due to this bending, the track reconstruction efficiency of particles with a transverse momentum below 1 GeV decreases rapidly, reaching around 40% for isolated pions with a  $p_T$  of 100 MeV [61]. Furthermore, for pions that are not produced in the primary vertex, this reconstruction efficiency will be even smaller. It is therefore impossible to rely on a reconstruction of the fermionic chargino decay products in this analysis.

In summary, since an early decaying chargino is not reconstructed as a PF particle, the event signature of a chargino-pair or a chargino-neutralino event consists only of one (or two) - potentially - disappearing track. Such a signature is very difficult to detect,

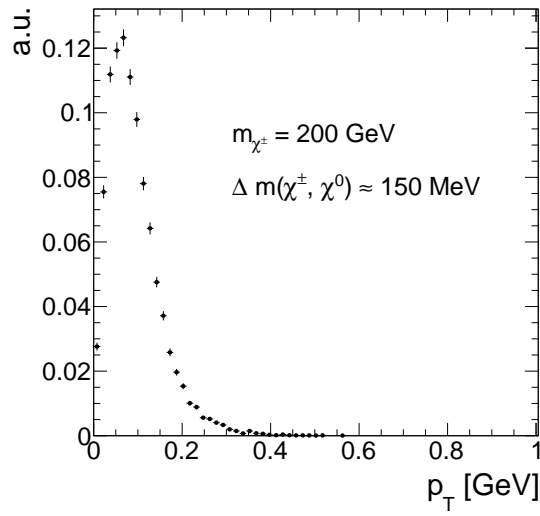


Figure III.2.5: Transverse momentum distribution of pions coming from chargino decay into a neutralino with a mass gap of 150 MeV.

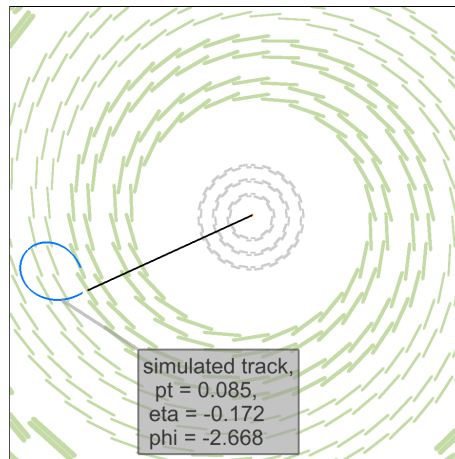


Figure III.2.6: Cross-sectional view of the tracker (silicon strip (silicon pixel) tracker layers are illustrated with green (grey) lines) and a simulated chargino track (black line) decaying to a pion (bended blue line) with a  $p_T$  of  $\sim 85$  MeV and a neutralino (not visible).

especially since CMS doesn't offer a dedicated track trigger so that triggering on the chargino track is impossible.

In order to search for such signatures, one therefore needs to trigger on other, less obvious properties of chargino events. This analysis takes advantage of higher order contributions to the Feynman diagrams shown in Figs. III.2.2 and III.2.3, resulting in initial state radiation (ISR). If the initial quarks radiate a high  $p_T$  gluon, the resulting jet can be detected and can offer a possibility to search for events with nothing more than isolated tracks. Furthermore, the non-detection of the chargino's decay products plus a high  $p_T$  ISR jet lead to missing transverse energy (MET) in the event. Exploiting these two circumstances, it is possible to detect chargino-pair or chargino-neutralino events with the help of Jet+MET triggers.

Since Jet+MET triggers are not very specific for chargino events, it is important to identify further track properties that can be used to select chargino candidates. One distinctive property of charginos compared to SM particles is their high mass. Therefore, charginos can be identified by selecting high  $p_T$  tracks. Furthermore, the energy loss per path length ( $dE/dx$ ) depends quadratically on the particle's mass for low velocities ( $0.2 < \beta\gamma < 0.9$ ):

$$\left\langle \frac{dE}{dx} \right\rangle = K \frac{m^2}{p^2} + C \quad (\text{III.2.2})$$

Therefore,  $dE/dx$  constitutes a very nice discriminating variable for massive particles like charginos against SM particles. The selection of chargino events in this analysis thus relies on the selection of isolated high  $p_T$  tracks with high  $dE/dx$  values.

If the chargino decays before it has crossed the full pixel and strip detector, the associated track is disappearing. For low lifetimes, the tracks can be very short and can have only a few hits in the detector. In order to reconstruct a particle's trajectory, a minimum of three hits are required since defining a helical path requires five parameters (see [61]). A specific challenge for this analysis is hence the combination of searching for short tracks and utilising the measurement of the energy deposition of the chargino. For very short tracks, eventually only passing the first couple of layers of the whole tracker system, the pixel tracker information becomes very important. Therefore, an accurate energy measurement in the pixel system is of great importance to this analysis. However, no other CMS analysis has used the energy information of the pixel tracker so far. This analysis thus requires a thorough study of the quality of the pixel energy calibration and, potentially, a recalibration in case the pixel energy calibration is not sufficient.

### III.2.1 Comparison to earlier searches

As already mentioned before, there are two analyses at CMS at  $\sqrt{s} = 8$  TeV with  $20 \text{ fb}^{-1}$  data that search for intermediate lifetime charginos, the search for long-lived charged



particles [56] and the search for disappearing tracks [55]. The here presented analysis aims at achieving an increase in sensitivity towards shorter lifetimes compared to the earlier analyses in a twofold way. First, the selection is optimised for the inclusion of very short tracks. Second, the inclusion of the variable  $dE/dx$  is used to increase the search sensitivity compared to [55].

In [56], a minimum number of eight hits were required for every track, whereas [55] required a minimum of seven hits. This can be very inefficient for shorter lifetimes, where most of the charginos already decay shortly after the pixel tracker. In Fig. III.2.7 (left), the normalised distribution of the number of measurements ( $N_{\text{hits}}$ ) of chargino tracks is shown. It can be seen, that  $N_{\text{hits}}$  peaks at the minimal possible value needed for track reconstruction of  $N_{\text{hits}} = 3$  for lower lifetimes. For a lifetime of  $c\tau = 50$  cm, a second peak at  $\sim 17$  hits appears corresponding to the number of measurements when crossing all pixel barrel (3) and strip inner and outer barrel (6 from stereo and 8 from normal) layers. However, a notable fraction of  $\sim 40\%$  of chargino tracks still has a number of measurements of  $N_{\text{hits}} < 8$ .

It should be also mentioned, that the track reconstruction efficiency is sufficient for short chargino tracks, such that a loosening of the  $N_{\text{hits}}$  requirement is expected to be really improving the signal acceptance. The track reconstruction efficiency for different chargino decay points is depicted in Fig. III.2.7 (right). For very short tracks ( $N_{\text{hits}} = 3$ ) the efficiency is still around 20%.

Additionally, the search for disappearing tracks which targets models with charginos decaying inside the tracker did not make use of the high energy deposition of heavy particles. Although this variable was indeed used in the search for long-lived charged particles, this search was not optimised for intermediate lifetimes (e.g. no explicit muon veto on the selected tracks was required). Thus, it shows less sensitivity compared to the disappearing track search in the lifetime region between  $35 \text{ cm} \lesssim c\tau \lesssim 100 \text{ cm}$  (see Fig. III.1.1).

To conclude, the general search strategy of the here presented analysis is to unite the strategies of [56] and [55] and to lower the strong selection on the number of hits in these analyses in order to get an optimised selection for lifetimes around  $10 \text{ cm} \lesssim c\tau \lesssim 40 \text{ cm}$ .

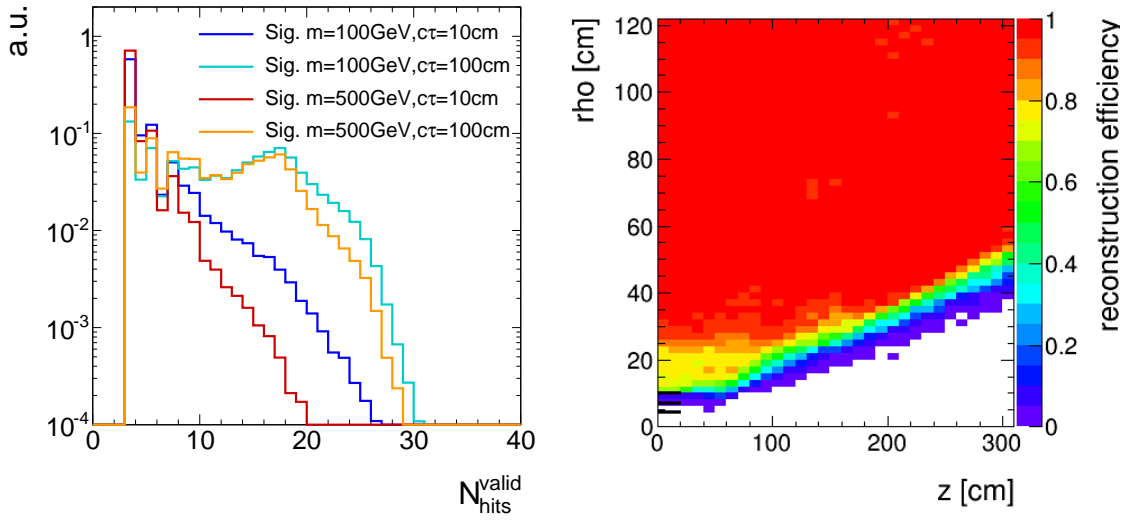


Figure III.2.7: Left: Number of measurements in the tracker system  $N_{\text{hits}}$  for four different signal lifetimes. Right: Probability to reconstruct a track ( $z$ ) in dependency of the chargino's decay point ( $x$  and  $y$ ). More information on the generation of the simulated signal samples can be found in Section III.4.2.

### III.3 Improved $dE/dx$ measurement for short tracks

As already pointed out in the previous chapter, the inclusion of the pixel energy measurements can increase the sensitivity when searching for short and highly ionising tracks. While the energy measurements in the silicon strip detector have already been calibrated as part of the search for long-lived charged particles [56], no complete calibration has been done for the pixel silicon tracker so far. To increase the discrimination power of  $dE/dx$  for short tracks, such a calibration procedure is therefore conducted within this PhD thesis.

The CMS tracker system provides a measurement of the particle's energy loss for each hit in the tracker. This is done by the detection of the number of electrons produced by the ionisation of the silicon. A detailed introduction to the CMS tracker system and the energy measurement can be found in Section ??.

How to combine the single energy measurements for each tracker hit into one track  $dE/dx$  estimator that can be used for analysis purposes will be explained in the following Section III.3.1. The pixel energy calibration is then described in Section III.3.2. How to discriminate SM particles and beyond SM particles with the help of a  $dE/dx$  measurement is discussed in Section III.3.3, followed by an exploration of how the inclusion of the pixel energy measurements in the  $dE/dx$  estimates leads to a better discrimination between Standard Model particles and long-lived charginos (Section III.3.4).

#### III.3.1 Estimation of the ionisation loss of charged particles

Energy losses for moderately relativistic charged particles travelling through matter are mostly caused by ionisation effects. The mean energy loss per path length can be described with the Bethe formula [62]:

$$\left\langle \frac{dE}{dx} \right\rangle = K z^2 \frac{Z}{A} \frac{1}{\beta^2} \left[ \frac{1}{2} \ln \frac{2m_e c^2 \beta^2 \gamma^2 T_{\max}}{I^2} - \beta^2 - \frac{\delta(\beta\gamma)}{2} \right]. \quad (\text{III.3.1})$$

It is a function of the atomic number ( $Z$ ), the atomic mass ( $A$ ) of the absorber, and the mean excitation energy ( $I$ ) which is 173 eV for silicon [63].  $T_{\max}$  represents the maximum energy transfer in a single collision. The relevant particle's properties are the velocity ( $\beta$ ), the Lorentz factor ( $\gamma$ ) and the charge ( $z$ ) of the incident particle. The density correction  $\delta(\beta\gamma)$  reduces the mean energy loss at high energies because of polarisation effects of the material. The factor  $K$  is constant and is 0.307 in units of  $\text{MeV mol}^{-1} \text{cm}^2$ . The Bethe

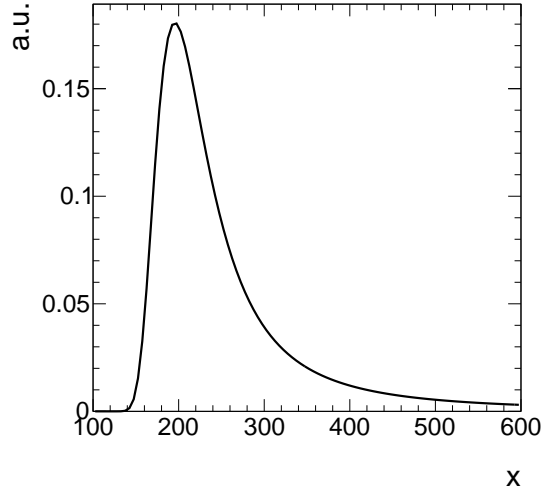


Figure III.3.1: Illustration of the shape of a Landau distribution. Parameters were chosen as  $\mu = 200$  and  $\sigma = 20$ .

1137 formula is valid if the main energy loss originates from ionisation effects, i. e. in a region  
1138 between  $0.1 \lesssim \beta\gamma \lesssim 1000$ .

1139 Even if widely used, the mean energy loss is a quantity which is “ill-defined experimen-  
1140 tally and is not useful for describing energy loss by single particles” [18]. The problem is  
1141 caused by the underlying probability distribution of one single  $dE/dx$  measurement (this  
1142 will be named  $\Delta E/\Delta x$  throughout the following sections), which can be parametrised by  
1143 a Landau distribution [64]

$$p(x) = \frac{1}{\pi} \int_0^\infty e^{-t \log t - xt} \sin(\pi t) dt. \quad (\text{III.3.2})$$

1144 The Landau distribution has no free parameters. Its most probable value is around 0.222.  
1145 However, it is possible to introduce artificially a different most probable value and a width  
1146 (at half maximum) with  $x \rightarrow \frac{x - \text{MPV}}{\sigma} - 0.222$ . The Landau distribution is a highly asym-  
1147 metric distribution with a long tail towards the right end (see Fig. III.3.1). Theoretically  
1148 it extends to infinite energies, however in nature the maximal deposited energy is of course  
1149 limited by the particle’s full energy.

1150 Because of its strong asymmetry, measurements of the mean energy loss per path length  
1151  $\langle dE/dx \rangle$  with only a few single measurements are easily fluctuating towards high values.  
1152 This makes the use of the mean energy loss described by the Bethe formula for the discrim-  
1153 ination of new heavy particles problematic, because fluctuations to high values reduce the  
1154 discrimination power against massive particles which release in general higher amounts of  
1155 energy in matter.

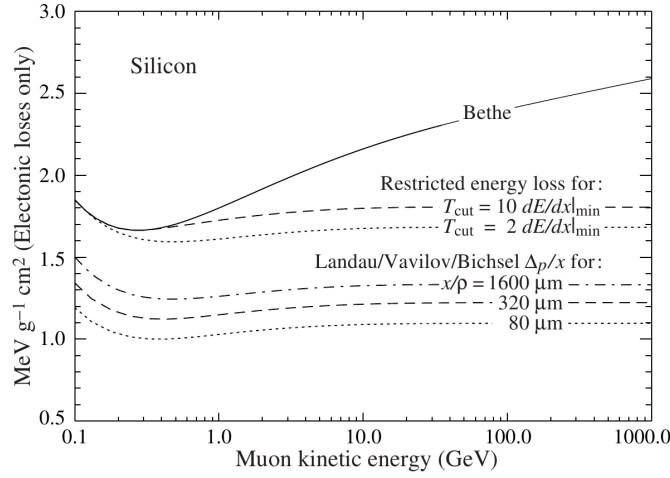


Figure III.3.2: Comparison between the Bethe mean energy loss, restricted energy loss and the most probable energy loss described by the Landau-Vavilov-Bichsel function for muons for different values of absorber thickness of silicon. Taken from [18].

A much better observable is the most probable value (MPV) of the Landau distribution. The MPV is much more stable compared to the mean and is not as easily fluctuating to higher  $dE/dx$  values. The most probable energy loss of a charged particle,  $\Delta_p$ , can be described by the Landau-Vavilov-Bichsel equation [65]:

$$\Delta_p = \xi \left[ \ln \frac{2m_e c^2 \beta^2 \gamma^2}{I} + \ln \frac{\xi}{I} + j - \beta^2 - \delta(\beta\gamma) \right], \quad (\text{III.3.3})$$

with  $\xi = (K/Z)\langle Z/A \rangle (x/\beta^2)$ . The thickness of the absorber  $x$  appears explicitly in the Landau-Vavilov-Bichsel equation making the most probable energy loss per path length  $\Delta_p/dx$  logarithmically dependent on  $x$ . A comparison between the Bethe mean energy loss  $\langle dE/dx \rangle$  and the most probable energy loss  $\Delta_p/dx$  for muons is shown in Fig. III.3.2.

Particles such as muons are minimally ionising in silicon for  $\beta\gamma \sim 3 - 4$ . For higher momenta the deposited energies increase again reaching a plateau at around  $\beta\gamma \sim 100$ . However, new heavy charged particles would mainly be unrelativistic because of their high mass and would therefore deposit much higher energies in the detector. This makes  $dE/dx$  a very well discriminating variable. Thus, the energy loss per path length can be used to discriminate between SM particles and new heavy charged particles due to the different velocity distributions.

As said before, the most probable energy loss is much more stable compared to the

1174 Bethe mean energy loss. Still, combining only a few measurements of  $\Delta E/\Delta x$  can also  
 1175 lead for  $\Delta_p/dx$  to large fluctuations towards high  $dE/dx$  values. In order to estimate  
 1176 experimentally the most probable  $dE/dx$  value from only a few energy measurements,  
 1177 several “estimators” can be used that suppress a potential bias towards the high end  
 1178 without introducing a bias towards lower values [66]. One of the estimators for determining  
 1179 a track’s  $dE/dx$  is the harmonic-2 estimator

$$I_{h2} = \left( \frac{1}{N} \sum_{i=1}^N (\Delta E_i / \Delta x_i)^{-2} \right)^{-1/2}, \quad (\text{III.3.4})$$

1180 where  $\Delta E_i / \Delta x_i$  corresponds to the  $\Delta E$  and  $\Delta x$  measurement in the  $i$ th hit of the track.  
 1181 This estimator is known to be robust and is not easily biased by large fluctuations in  
 1182  $\Delta E/\Delta x$  because of the suppression by the power of minus two [66].

### 1183 III.3.2 Energy calibration of the silicon pixel tracker

1184 During Run I in 2012, the pixel silicon detector was continuously subjected to an energy  
 1185 calibration, a so-called gain calibration. Every pixel was calibrated to the same response,  
 1186 so that the whole pixel tracker should have been well inter-calibrated [67]. Unfortunately,  
 1187 due to various reasons, such as the imperfect constancy of the reference signal, or radiation  
 1188 and temperature induced changes, the energy calibration could not ensure a fully calibrated  
 1189 pixel tracker.

1190 This imperfection of the gain calibration can be seen in Fig. III.3.3, where the mean of  
 1191 the harmonic-2 estimator for all tracks  $\langle I_{h2} \rangle$  over the full data-taking period in 2012 is  
 1192 shown. Four different steps can be spotted. The first and the third steps correspond to  
 1193 changes in the settings of the tracker due to irradiation. The second and fourth step are  
 1194 induced by associated adjustments in the online gain calibration. Unfortunately, although  
 1195 the gain calibration was adjusted (even with some delay), it was not able to ensure a  
 1196 constant energy response of the pixel tracker over time. The variations of the  $dE/dx$   
 1197 measurement over time of around 15% are too large to use  $dE/dx$  without a further  
 1198 calibration.

1199 The following sections explain the method of the gain calibration of the pixel silicon  
 1200 tracker which is conducted for this analysis. It is splitted into two sections. The first  
 1201 section is dedicated to the gain inter-calibration of the pixel tracker which ensures a ho-  
 1202 mogeneous energy response of all tracker modules. In the second section, the absolute gain  
 1203 calibration is discussed. This calibration step is needed to ensure that the measurement  
 1204 of the energy release of a particle is actually translated to the correct physical value.

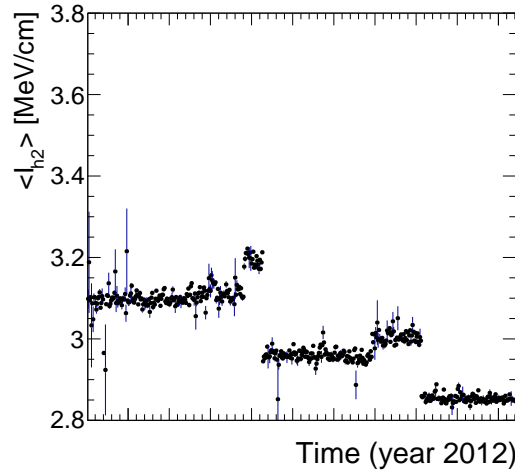


Figure III.3.3: Mean of all track's  $dE/dx$  (harmonic-2 estimator) over the full year 2012. Only pixel hits are taken into account. Every data point corresponds to one run.

### Inter-calibration of gain

The main goal of the gain calibration is to get a uniform response in the ionisation energy loss  $dE/dx$  over the full data taking period in 2012. To also ensure a uniform response over all modules within one time step, an additional inter-calibration on module level is carried out. The inter-calibration can in principle be done on various levels: the highest granularity would be a calibration on pixel level, followed by a calibration on read-out-chip (ROC) level and then on module-level. Lower granularities in descending order are rings (modules with same z-position) and finally layers (3 layers in the barrel and 4 disks in the endcap). It is verified that all pixels and all ROCs (on one module) are well inter-calibrated, such that the inter-calibration is finally done module-wise.

The gain calibration of the pixel silicon tracker is carried out with the help of minimally ionising particles (MIPs). MIPs in this context are not defined as particles at the minimum of the Bethe formula, but more generally as particles located at or near the plateau of the  $dE/dx$  distribution vs. momentum (see Fig. III.3.2). This approach ensures that all particles deposit similar amounts of energy so that the variation due to different momenta is minimised.

MIPs are selected by a momentum selection of  $p > 2$  GeV. Additionally, only tracks with at least eight hits and a  $\chi^2/\text{n.d.o.f.} < 3$  are used to ensure a high-quality track reconstruction. A sample containing around 50 million “minimum bias” events is used for calibration. The “minimum bias” sample was specifically recorded for tracker calibration purposes.

For every module in the pixel tracker (there are 1440 modules in total), a distribution of the energy loss per path length  $\Delta E/\Delta x$  is built. The measurement of  $\Delta E/\Delta x$  is done in ADC counts per mm. ADC counts are a measure for the deposited charge after digitisation. Figure III.3.4 shows an example distribution for one module. The underlying Landau distribution can be nicely seen. To extract the MPV for every module a fit to the core distribution is performed. The fit is not only done with a Landau but a Landau convoluted with a Gaussian function to be closer to the experimentally observed energy spectrum. This also increases the fit performance and the stability of the fit. The path length  $\Delta x$  is calculated with

$$\Delta x = d_{\text{module}_i} \cdot \cos(\phi_{\text{track}}), \quad (\text{III.3.5})$$

where  $d_{\text{module}_i}$  is the thickness of module  $i$  and  $\phi_{\text{track}}$  is the relative angle of the particle's trajectory to the normal axis of the module. With the measured MPV extracted from the fit, an inter-calibration factor is calculated for every module

$$c_{\text{inter}} = \frac{\text{MPV}_{\text{target}} [\text{ADC/mm}]}{\text{MPV} [\text{ADC/mm}]} = \frac{300 \cdot 265 \text{ ADC/mm}}{\text{MPV} [\text{ADC/mm}]}. \quad (\text{III.3.6})$$

The factor  $300 \cdot 265 \text{ ADC/mm}$  is in principal an arbitrary number since the final response is adjusted by the absolute gain calibration described in the next section. However, it is chosen such that the measured calibration factors are close to one. The calibration factor

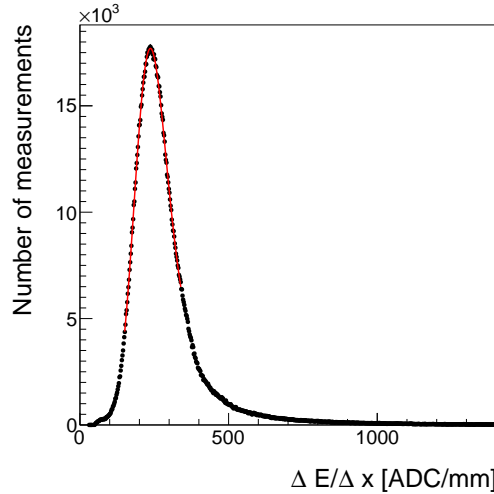


Figure III.3.4: An example of the  $\Delta E/\Delta x$  distribution measured in ADC count per mm for one module of the CMS pixel tracker. A Landau convoluted with a Gaussian is fitted to the core of the distribution in an iterative procedure.



can then be used to scale every single measurement in a module to a calibrated  $\Delta E/\Delta x$  measurement

$$\left(\frac{\Delta E}{\Delta x}\right)_{\text{calibrated}} = c_{\text{inter}} \cdot \left(\frac{\Delta E}{\Delta x}\right)_{\text{uncalibrated}} \quad (\text{III.3.7})$$

The determination of the calibration factor is done for every of the five time steps, shown in Fig. III.3.3 independently, in order to get rid of the time dependency. The outcome of the application of the calibration factors to the single energy measurements in the pixel tracker can be seen in Fig. III.3.5. The variation over time is indeed eliminated, resulting in a maximal time variation of less than  $\sim 1\%$ .

Additionally, the same procedure is carried out for a corresponding simulated data sample to ensure the inter-calibration of the pixel modules on all simulated samples.

### Absolute calibration of gain

As a final step, the targeted MPV being  $\text{MPV}_{\text{target}} = 300 \cdot 265 \text{ ADC/mm}$  needs to be translated to a meaningful physical quantity given in physical units (e.g. MeV/cm). That means, that the charge measurement in ADC counts needs to be converted to the real energy release from a particle. The relation between  $\Delta E$  in ADC counts and the energy loss in eV is given by

$$\Delta E [\text{eV}] = c_{\text{inter}} \cdot \Delta E [\text{ADC}] \cdot \frac{N_e}{\text{ADC}} \cdot 3.61 \text{ eV}, \quad (\text{III.3.8})$$

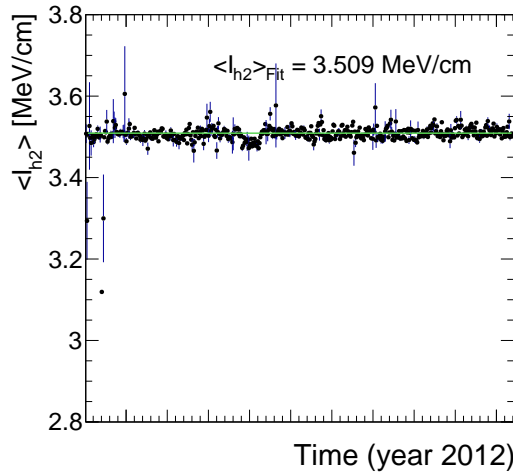


Figure III.3.5: Mean of all track's  $dE/dx$  (harmonic-2 estimator) over the full year 2012 after applying the calibration factors, resulting in an average  $dE/dx$  of 3.51 MeV/cm. Only pixel hits are taken into account. Every data point corresponds to one run.

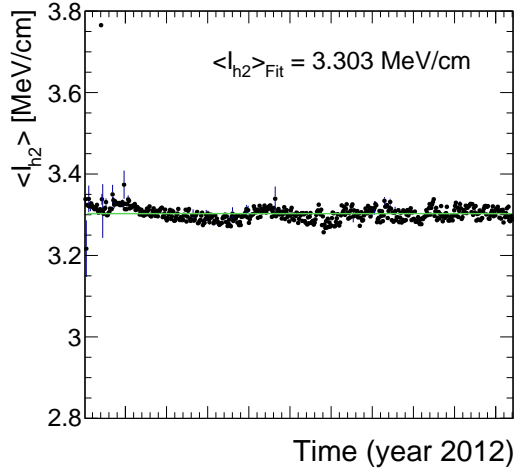


Figure III.3.6: Mean of all track's  $dE/dx$  (harmonic-2 estimator) measured in the silicon strip detector over the full year 2012. The average most probable  $dE/dx$  is  $I_{h2} = 3.303$  MeV/cm. Every data point corresponds to one run.

where  $N_e/\text{ADC}$  is the number of electrons which correspond to one calibrated ADC count and 3.61 eV is the mean energy needed to create one electron-hole pair in silicon at  $-10^\circ\text{C}$ . Such an absolute gain calibration can be done with the help of several methods (all explained in [66]). The absolute calibration of the silicon pixel tracker can rely on the already conducted absolute calibration of the silicon strip detector. In [66], the absolute gain calibration was done with the help of the most probable energy release per path length of muons, theoretically described by the Landau-Vavilov-Bichsel formula in Eq. (III.3.3). To calibrate the pixel tracker to the correct energy loss per path length it is therefore sufficient to determine one calibration factor to relate the average  $dE/dx$  of all tracks in the pixel tracker as shown in Fig. III.3.5 to the average measured  $dE/dx$  in the strip tracker, shown in Fig. III.3.6 by

$$c_{\text{absolute}} = \frac{\langle dE/dx_{\text{strip}} \rangle}{\langle dE/dx_{\text{pixel}} \rangle} = \frac{3.303}{3.509} = 0.941. \quad (\text{III.3.9})$$

This factor is then applied on top of  $c_{\text{inter}}$  for all pixel modules.

Finally, an absolute calibration factor needs to be determined for the simulated samples, where the simulated pixel tracker is calibrated to the average  $dE/dx$  of the silicon strip measured in data.

### III.3.3 Discrimination of highly-ionising particles

As mentioned before, it is difficult to find a robust estimator for the most probable energy loss of a particle, if only a few measurements of  $\Delta E/\Delta x$  along the particle's trajectory are available. The harmonic-2 estimator  $I_{h2}$  was already introduced in Section III.3.1 in Eq. (III.3.4). It is known to be a robust estimator not easily affected by large fluctuations in  $\Delta E/\Delta x$ . However, it was shown in [66] that a better discrimination between SM particles and possible new heavy particles can be achieved when using likelihood techniques, i. e. determining the probability that the set of all  $\Delta E/\Delta x$  belonging to one track is actually compatible with the hypothetical probability distribution of a MIP.

That a measured sample has been drawn from a specific distribution can be tested with the co-called Smirnov-Cramér-von Mises test [68, 69]. It is deduced from the integral of the squared difference of a measured distribution to a hypothesis distribution, and leads to a test statistics of [66]

$$I_s = \frac{3}{N} \cdot \left( \frac{1}{12N} + \sum_{i=1}^N \left[ P_i - \frac{2i-1}{2N} \right]^2 \right), \quad (\text{III.3.10})$$

where  $N$  is the total number of energy measurements and  $P_i$  is the cumulative probability that a MIP would release a  $\Delta E/\Delta x$  equal or smaller than the measured  $\Delta E/\Delta x$  with all  $P_i$  arranged in increasing order.

However, this test statistics is not sensitive to the sign of the difference between the measured and the theoretical distribution. It can therefore not distinguish between incompatibilities due to variations towards higher or lower energy deposits compared to the hypothesis distribution. Thus it is not suitable for the discrimination between MIPs and heavy new particles by  $dE/dx$ . A so-called Asymmetric Smirnov-Cramér-von Mises discriminator was developed in [66] which is only sensitive to incompatibilities to the MIP hypothesis towards higher energy depositions

$$I_{as} = \frac{3}{N} \cdot \left( \frac{1}{12N} + \sum_{i=1}^N \left[ P_i \cdot \left( P_i - \frac{2i-1}{2N} \right)^2 \right] \right). \quad (\text{III.3.11})$$

A value of  $I_{as}$  close to zero indicates good compatibility with the MIP hypothesis, whereas a value close to one indicates bad compatibility because of unexpectedly high energy losses.

The underlying probability  $P_i$  of the energy release for a given path length in the pixel tracker is extracted from the same “minimum bias” sample used for the pixel energy calibration. In total 28 different templates each for a different given path length are created. In Fig. III.3.7 the probability distribution template for the pixel tracker in data and simulation is shown. The corresponding templates for the energy release in the silicon strip detector were already built by [66].

A comparison between the energy release by MIPs ( $I_{\text{as}}$ ) in data and simulation for high-quality tracks with  $p > 5 \text{ GeV}$  and  $|\eta| < 2.1$  can be found in Fig. III.3.8.

$dE/dx$  shows good agreement in data and simulation for  $I_{\text{as}} < 0.1$ . For larger values,  $I_{\text{as}}$  shows a larger decrease in simulation than in measured data. For this reason a data-based approach for analyses exploiting  $dE/dx$  information is needed.

### III.3.4 Discrimination improvements

The goal of including the pixel energy information is to increase the discrimination power of  $I_{\text{as}}$  between background and signal tracks, especially for shorter lifetimes. In Fig. III.3.9 (left), a comparison of the shapes of the energy release by MIPs and by signal tracks in simulation is shown (details about the simulated samples can be found in the next section Section III.4.2). It can be seen, that the  $I_{\text{as}}$  distributions of the signal models show a larger tail towards  $I_{\text{as}} = 1$ , whereas the  $I_{\text{as}}$  of the background is rapidly falling.

In the right part of Fig. III.3.9, a comparison of the  $I_{\text{as}}$  distributions of four different signal models is shown. Charginos with longer lifetimes have a more pronounced tail

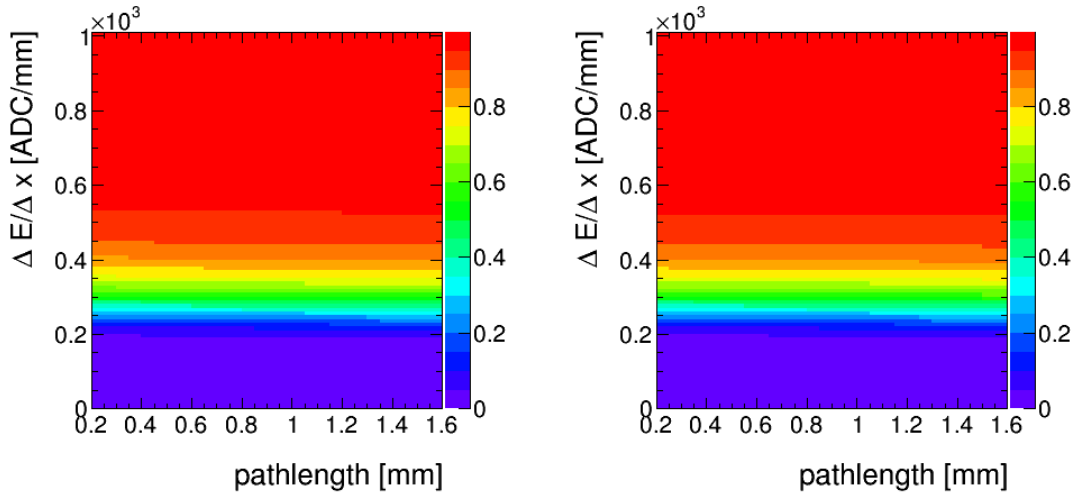


Figure III.3.7: Cumulative probability for a MIP to release a  $\Delta E/\Delta x$  (y-axis) vs. the pathlength (x-axis) in data (left) and simulation (right) for the pixel tracker based on the “minimum bias” sample.

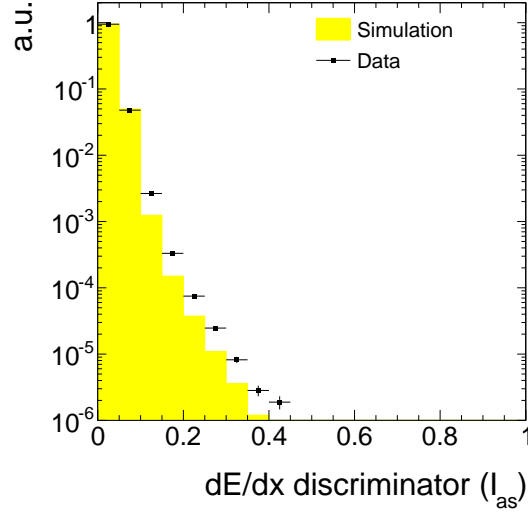


Figure III.3.8: Normalised  $I_{as}$  distribution for MIPs from the minimum bias sample in data and simulation for high-quality (high purity as defined in [70], a minimum number of eight hits and no missing inner and middle hits) tracks with  $p > 5 \text{ GeV}$  and  $|\eta| < 2.1$ .

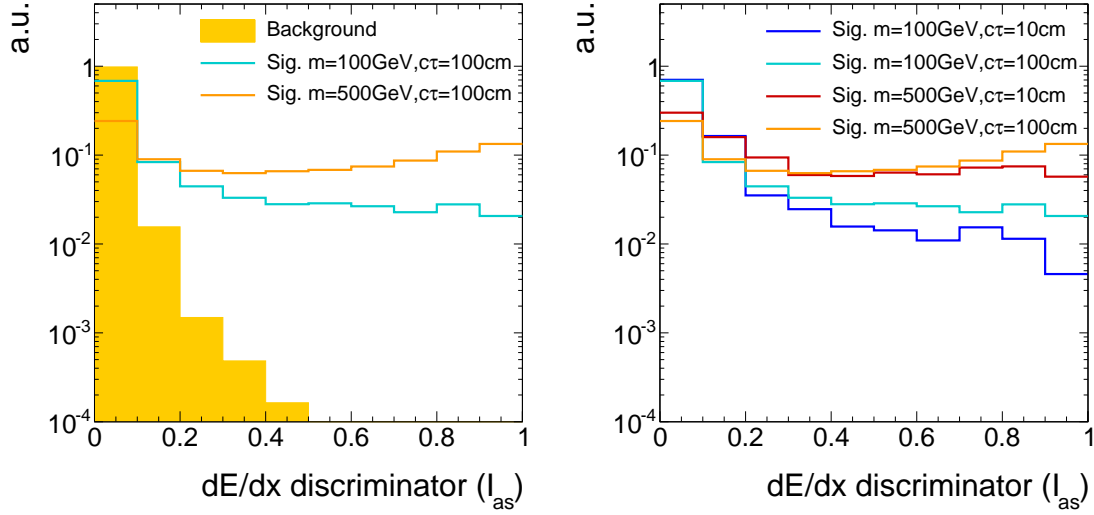


Figure III.3.9: Normalised  $I_{as}$  distribution for simulated background and signal tracks (left) and for four different signal models (right) for high-purity tracks (as defined in [70]) with  $p_T > 10 \text{ GeV}$  and  $|\eta| < 2.1$ . For the illustration of the background tracks' spectrum simulated  $t\bar{t}$ +jets events are used (more information about this sample is given in Chapter III.4).

toward  $I_{\text{as}} = 1$ . This can be understood with the help of Eq. (III.3.3), where the influence of the velocity ( $\beta$ ) on the ionisation loss can be seen. The velocity distribution of the charginos is mostly affected by the mass of the chargino. However, also for charginos with same mass, the velocity is higher in average for shorter lifetimes. This is caused by the fact, that for shorter lifetimes (e.g.  $c\tau = 10\text{cm}$ ), already a sizable fraction of the charginos decay before reaching the tracker system. The probability of reaching the detector increases for higher velocities because of the boost, which can be clearly seen at the survival probability

$$P(t) = e^{-\frac{t}{\gamma\tau}}. \quad (\text{III.3.12})$$

This means that the track reconstruction/selection lead to a biased average  $\beta$  for shorter lifetimes which in turn lead to lower values of  $I_{\text{as}}$ .

The  $I_{\text{as}}$  distribution is not only influenced by the velocity of a particle but also by the number of hits of a track. The number of measurements in the tracker system defines the influence of single fluctuations in  $\Delta E/\Delta x$  on the  $I_{\text{as}}$  discriminator, because of the long right tail of the Landau distribution. A low number of hits, therefore, leads to higher  $I_{\text{as}}$  values. This effect is also visible in Fig. III.3.9 (right). The small surplus for lower lifetimes between 0.1 and 0.2 is caused by the smaller number of measurements for earlier decaying charginos.

Finally, the impact of the additional  $\Delta E/\Delta x$  information from the pixel tracker on the selection efficiency of signal and background tracks is quantified. Figure III.3.10 shows the signal selection efficiency against the background selection efficiency for different selection cuts in  $I_{\text{as}}$ , once including the pixel information and once without it. The background selection efficiency is estimated with simulated  $W$ +jets events but was additionally checked on simulated  $t\bar{t}$ +jets and QCD-multijet events (further information about the simulated samples can be found in the next Chapter III.4). No significant difference between these processes in the background selection efficiency was observed.

The signal selection efficiency and the background suppression depend on the mass and the lifetime of the charginos. The improvement of the discriminating power is much more pronounced for higher chargino masses.

It can be seen that the inclusion of the pixel information increases the background suppression for a given signal efficiency throughout the investigated signal models. This background suppression improvement is most pronounced for very tight cuts on  $I_{\text{as}}$  up to a factor of 20 and even more and still considerable for looser selections with signal efficiencies of around 40% (factor of 10).

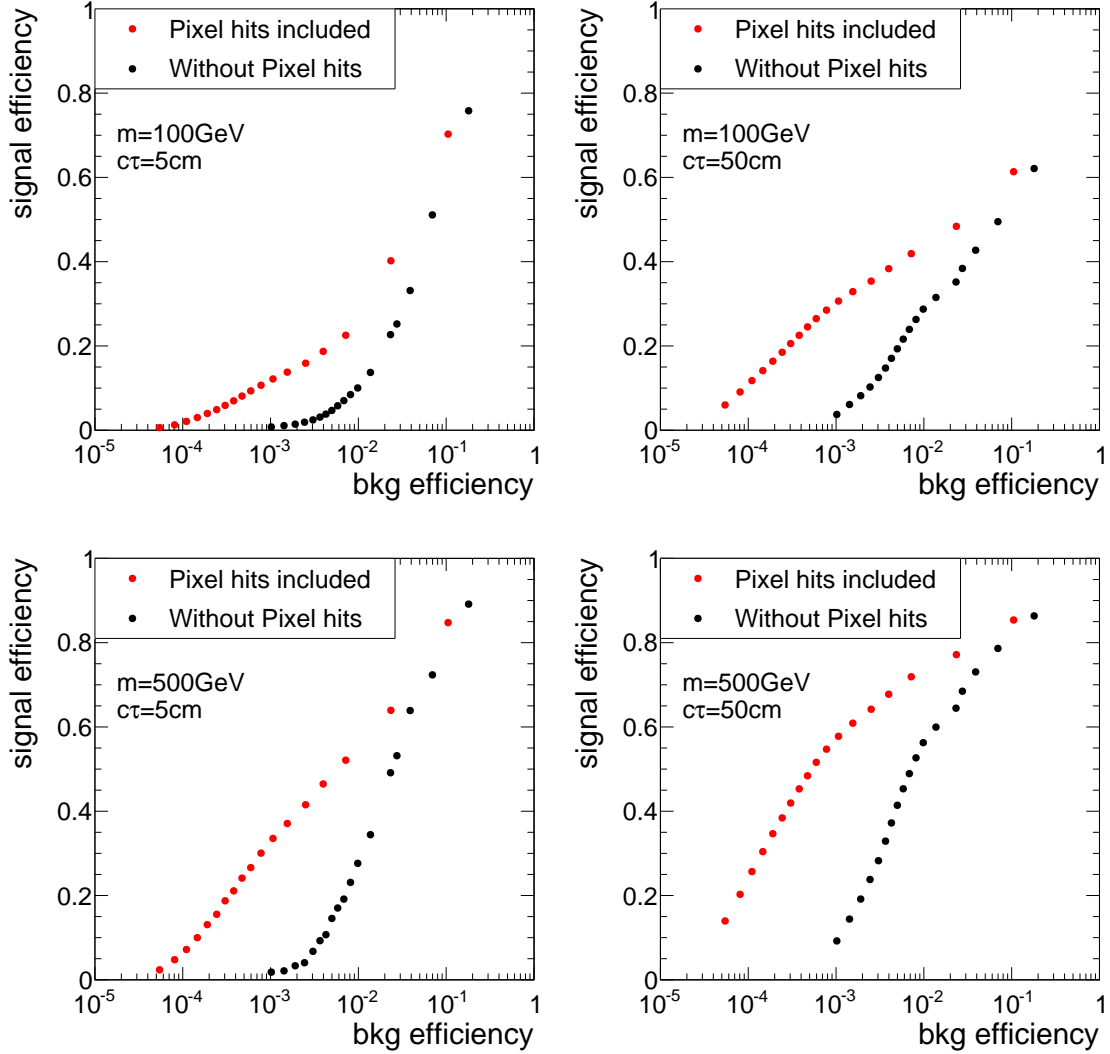


Figure III.3.10: Signal selection efficiency vs. background selection efficiency with (red) and without (black) pixel information. Each point corresponds to one selection cut in  $I_{\text{as}}$ . The figure is based on a simulated  $W + \text{jets}$  sample and a simulated signal sample with chargino-chargino production, both subject to a selection of high-quality tracks (without a selection on  $N_{\text{hits}}$ ) with  $p_T > 10 \text{ GeV}$ .

## III.4 Simulated samples

In order to design the search and to study background and signal characteristics, this analysis relies on simulated SM and SUSY datasets. An extensive introduction to the techniques and tools required for the simulation of SM and beyond SM processes can be found in Section ??.

The following two sections present an overview of the SM (Section III.4.1) and SUSY samples (Section III.4.2) used in this search. All samples are reweighted to match the measured distribution of primary vertices per event in data. Additionally, event weights are applied to ensure the same ISR spectrum in simulation as in data.

### III.4.1 Standard Model background samples

To investigate the sources of background, various simulated SM samples are used. Since this analysis aims at making use of  $dE/dx$ , a special data format of the simulated samples, the so-called RECO format, is required. Unfortunately, not all SM processes are available in this specific format making it impossible to compare the total number of events in simulation and real data. This, however, does not constitute a serious problem since this analysis will finally use data-based background estimation methods. The simulated SM datasets can still be used to compare the shapes of important distributions in simulation and data.<sup>1</sup> Still, the most important SM background sample including  $W$  + jets events is available. Due to the intrinsic missing energy in  $W$  + jets events it constitutes the major background to the presented search (see Section III.6 for further details on the backgrounds).

In Table III.4.1 all available SM samples used in this analysis are listed. The matrix-elements of the  $W$  + jets,  $t\bar{t}$  + jets and  $Z \rightarrow \ell\bar{\ell}$  + jets samples are generated using MADGRAPH 5 [71]. For the QCD sample PYTHIA6 [72] is used for generation. All samples are then passed to PYTHIA 6 to simulate the hadronisation and the showering. The interactions between the particles and the detector material is simulated using GEANT4 [73, 74].

Due to the size of the samples (between 5 and 70 TB per sample) a reduction is required

---

<sup>1</sup>For example, the simulated  $Z \rightarrow \nu\bar{\nu}$  + jets sample that can contribute to the background of this search via fake tracks is not available in RECO format. However, as the shape of important observables of fake tracks is independent of the underlying process, this background can be studied with a simulated  $W$  + jets sample.



Table III.4.1: Available Standard Model background samples containing  $\Delta E/\Delta x$  information that are used for background estimation studies.

Process	Generator	Cross section [pb]	$\mathcal{O}^{\text{cross section calculation}}$
$W + \text{jets}$	MADGRAPH 5	36703.2	NNLO [75]
$t\bar{t} + \text{jets}$	MADGRAPH 5	245.8	NNLO [76]
$Z \rightarrow \ell\bar{\ell} + \text{jets}$ ( $\ell = e, \mu, \tau$ )	MADGRAPH 5	3531.9	NNLO [75]
QCD ( $50 \text{ GeV} < \hat{p}_T < 1400 \text{ GeV}$ )	PYTHIA 6	9374794.2	LO

in order to limit the storage space requirements. This is achieved by selecting only events which contain at least one jet with a minimum transverse momentum of  $p_T > 60 \text{ GeV}$ .

In addition, further simulated samples not containing the energy information are used (so-called AOD samples). Because of their much smaller size, these samples are available in full size. They are needed to study the background inclusively in the variable  $dE/dx$ .

### III.4.2 Signal samples

For the investigation of a possible SUSY signal, events containing either chargino pair production  $q\bar{q} \rightarrow \tilde{\chi}_1^\pm \tilde{\chi}_1^\mp$  or chargino neutralino production  $q\bar{q} \rightarrow \tilde{\chi}_1^\pm \tilde{\chi}_1^0$  are simulated within this thesis. The simulation of the samples is done as described in Section III.4.1 for the  $W + \text{jets}$  sample. However, a special treatment for long-lived particles is required for this analysis. In order to get a correct detector simulation of the energy loss of long-lived particles that decay after the beam pipe, the decay of the chargino cannot be simulated within MADGRAPH or PYTHIA but needs to be simulated within GEANT4. The decay mode of the chargino is also specified within GEANT4 to a neutralino plus pion decay,  $\tilde{\chi}_1^\pm \rightarrow \tilde{\chi}_1^0 \pi^\pm$ .

To reduce the required computing sources, the simulation is only done for a few lifetimes (1 cm, 5 cm, 10 cm, 50 cm, 100 cm, 1 000 cm and 10 000 cm). The lifetime is hereby not controlled by changing the mass gap between the chargino and the neutralino but is independently specified within GEANT4. In order to scan in a high resolution over the lifetime space, other lifetimes are generated using lifetime reweighting. The weight for

each event depends on the individual proper lifetime of the chargino and is given by

$$w = \prod_{i=1}^n \frac{\tau^{\text{gen}}}{\tau^{\text{target}}} \cdot \exp \left[ t_i \cdot \left( \frac{1}{\tau^{\text{gen}}} - \frac{1}{\tau^{\text{target}}} \right) \right], \quad (\text{III.4.1})$$

where  $n$  is the number of charginos in the event,  $\tau^{\text{gen}}$  is the generated mean lifetime in the particle's rest frame and  $t_i$  is the individual proper lifetime of the chargino. The targeted mean lifetime is given by  $\tau^{\text{target}}$ . A derivation of this formula can be found in Appendix ??.

Using this reweighting procedure a good coverage of the lifetime space can be achieved with lifetimes of  $1 \text{ cm} \leq c\tau \leq 10^4 \text{ cm}$ . Figure III.4.1 shows the exponential distribution of the individual proper lifetime of the charginos after the reweighting of a simulated sample with  $c\tau^{\text{gen}} = 50 \text{ cm}$  to a lifetime of  $c\tau^{\text{target}} = 10 \text{ cm}$ . It can be seen that the reweighting procedure does indeed reproduce the targeted lifetime of 10 cm.

All samples are generated for different masses of the chargino, but always almost mass-degenerate to the lightest neutralino. The mass gap between chargino and neutralino is set to 150 MeV and, as said before, is hereby disentangled to the chargino lifetime for the simulation of the signal samples. However, since this analysis does not make use of the decay products of the chargino and the mass gap is for all simulated lifetimes of a similar small size, the choice of the mass gap does not affect the signal prediction. Six different masses from 100 GeV to 600 GeV are simulated. This leads to a total number of 42 signal samples. In Table III.4.2, the cross sections at  $\sqrt{s} = 8 \text{ TeV}$  for  $\tilde{\chi}_1^\pm \tilde{\chi}_1^\mp$  and  $\tilde{\chi}_1^\pm \tilde{\chi}_1^0$

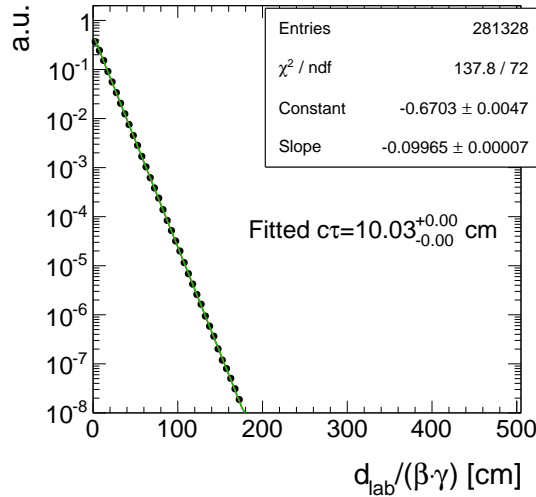


Figure III.4.1: Normalised distribution of the proper individual lifetime  $d_{\text{lab}}/(\beta\gamma)$  of all charginos contained in a signal sample with a generated lifetime of  $c\tau^{\text{gen}} = 50 \text{ cm}$  reweighted to a lifetime of  $c\tau^{\text{target}} = 10 \text{ cm}$ . Fitting an exponential curve  $a \cdot \exp \left[ \frac{1}{c\tau} ct_i \right]$  yields  $c\tau = 1./\text{Slope} = 10 \text{ cm}$ .

production for wino-like charginos and neutralinos are listed [77, 78]. The cross section does not depend on the lifetime of the chargino.

Table III.4.2: Simulated signal mass points with corresponding cross sections at NLO-NLL (NLO: next-to-leading order, NLL: next-to-leading logarithmic) accuracy for wino-like charginos [77, 78].

$m_{\tilde{\chi}_1^\pm}$ [GeV]	$\sigma_{\tilde{\chi}_1^\pm \tilde{\chi}_1^\mp}$ [pb]	$\sigma_{\tilde{\chi}_1^0 \tilde{\chi}_1^\mp}$ [pb]
100	5.8234	11.5132
200	0.37924	0.77661
300	0.06751	0.14176
400	0.01751	0.03758
500	0.00553	0.01205
600	0.00196	0.00431

## III.5 Event selection

### III.5.1 Datasets and triggers

The analysis is performed on pp collision data recorded in the year 2012 by the CMS experiment at a centre-of-mass energy of  $\sqrt{s} = 8$  TeV. In total an integrated luminosity of  $19.7 \text{ fb}^{-1}$  was recorded in 2012.

As outlined in Section III.2, the detection of chargino tracks is a challenging task already on trigger level. Direct triggering of events containing chargino-like tracks is not possible because in 2012 there was no dedicated track trigger available. Furthermore, there is no intrinsic missing transverse energy in the event if the chargino is not reconstructed as a PF particle, e.g. when it decays inside the tracker. Therefore, this analysis uses initial state radiation for the detection of chargino events. If ISR occurs, it is possible to trigger on a high- $p_T$  jet ( $p_T^{\text{1st jet}}$ ) and missing transverse momentum ( $\cancel{E}_T$ ).

For this purpose, several triggers are utilised in this analysis. An event is selected, if at least one of the three triggers in Table III.5.1 fired. The HLTMonoCentralPFJet80\_PF

Table III.5.1:  $\cancel{E}_T$  and  $\cancel{E}_T + \text{jet}$  triggers used in this analysis together with the corresponding recorded integrated luminosity during the time when they were in place.

Trigger	Integrated luminosity [ $\text{fb}^{-1}$ ]
HLTMonoCentralPFJet80_PFMETnoMu95_NHEF0p95	5.3
HLTMonoCentralPFJet80_PFMETnoMu105_NHEF0p95	14.4
HLT_MET120_HBHENoiseCleaned	19.7

1431 METnoMu95\_NHEF0p95 and HLTMonoCentralPFJet80\_PFMETnoMu105\_NHEF0p95 trig-  
 1432 gers both rely on the L1 ETM40 trigger which requires the missing energy to be larger  
 1433 than 40 GeV. On HLT level, they further require at least one particle-flow jet within  
 1434 the pseudorapidity range of  $|\eta| < 2.6$  with  $p_T > 80$  GeV and the PF missing trans-  
 1435 verse momentum (not taking into account the  $p_T$  of muons) to be larger than 95 GeV  
 1436 or 105 GeV, respectively. Finally, no more than 95% of the jet energy must be carried  
 1437 by neutral hadrons. The HLTMonoCentralPFJet80\_PFMETnoMu95\_NHEF0p95 trigger  
 1438 was active during Run A and Run B in 2012 data taking, whereas HLTMonoCentralPF-  
 1439 Jet80\_PFMETnoMu105\_NHEF0p95 was in place during Run C and Run D in 2012.

1440 The HLT\_MET120\_HBHENoiseCleaned trigger is based on the L1 trigger ETM36. On  
 1441 HLT level, the trigger requires that the missing energy measured from calorimeter energy  
 1442 deposits is larger than 120 GeV. The HBHENoise-filter reduces background from electronic  
 1443 noise in the HCAL.

Table III.5.2: MET data samples used in the search with the contained integrated luminosity.

Dataset	Integrated luminosity [ $\text{fb}^{-1}$ ]
/MET/Run2012A-22Jan2013-v1/RECO	0.876
/MET/Run2012B-22Jan2013-v1/RECO	4.412
/MET/Run2012C-22Jan2013-v1/RECO	7.055
/METParked/Run2012D-22Jan2013-v1/RECO	7.354

The events that were selected by the described triggers are available in the MET datasets listed in Table III.5.2. Again, because of the size of the datasets ( $\sim 150$  TB in total), a reduction of the size is achieved by selecting only events where one of the used triggers fires and that contains at least one jet with a minimum  $p_T$  of 50 GeV.

## III.5.2 Selection of signal candidate events

In order to suppress events originating from Standard Model processes such as QCD-multijet events,  $W + \text{jets}$ , etc., a selection favouring signal-like tracks is applied. The signal candidate selection closely follows the selection required in the disappearing track search [79, 80]. It relies on event-based and track-based variables as described in the following two sections.

### III.5.2.1 Event-based selection

First, a selection on the quality of the primary vertex is applied in order to suppress cosmic events and noise from the beam halo. This selection includes requirements on the position of the vertex with respect to the beam axes and the number of degrees of freedom of the vertex [81]

- ❖ The vertex must have at least four degrees of freedom:  $vtx$  with  $\geq 4$  d.o.f.
- ❖ The position of the vertex along the beam line must be within 24 cm with respect to the nominal interaction point:  $|dz| \leq 24$  cm.
- ❖ The position in the transverse direction must be within 2 cm with respect to the nominal interaction point:  $|d0| \leq 2$  cm.

To maximise the signal acceptance, the trigger related selection cuts are chosen close to the trigger thresholds (see Section III.5.1). In Fig. III.5.1, the distributions of  $\cancel{E}_T$  and the transverse momentum of the leading jet,  $p_T^{1^{\text{st}} \text{ jet}}$ , are shown for different signal models. The leading jet has to be centrally produced,  $|\eta_{1^{\text{st}} \text{ jet}}| < 2.4$ , and to fulfil the following criteria:

- Charged hadron energy fraction ( $\text{CHF}_{1^{\text{st}} \text{ jet}}$ )  $> 0.2$
- Charged electromagnetic energy fraction ( $\text{CEF}_{1^{\text{st}} \text{ jet}}$ )  $< 0.5$
- Neutral hadron energy fraction ( $\text{NHF}_{1^{\text{st}} \text{ jet}}$ )  $< 0.7$
- Neutral electromagnetic energy fraction ( $\text{NEF}_{1^{\text{st}} \text{ jet}}$ )  $< 0.7$ .

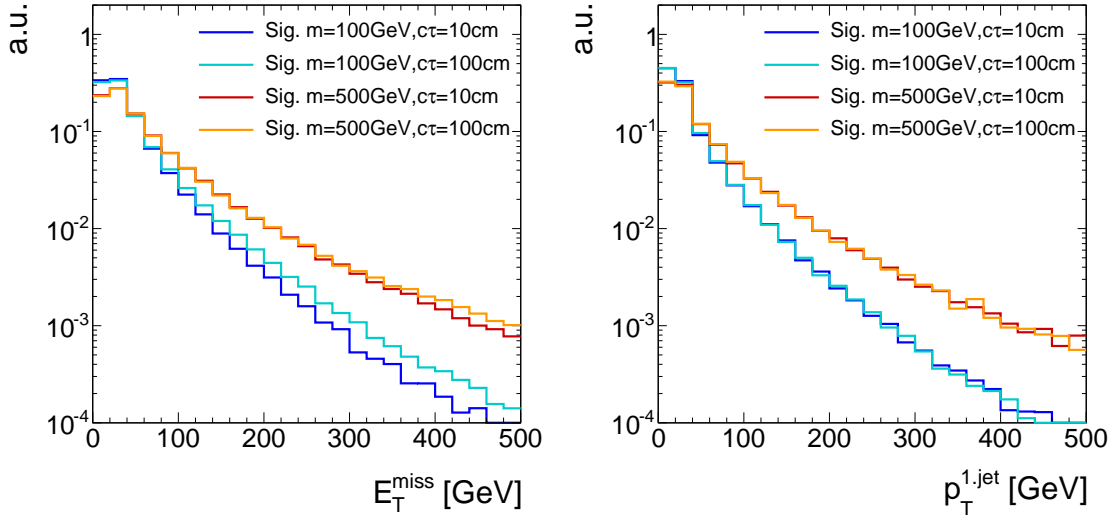


Figure III.5.1: Normalised distributions of the missing transverse momentum (left) and the transverse momentum of the leading jet (right) for four different signal models.

These additional jet quality criteria ensure that noise from cosmic and beam halo muons and high- $p_T$  photons and electrons is suppressed [82].

The trigger efficiency as a function of  $\cancel{E}_T$  and  $p_T^{1st\,jet}$  was determined within [83] with a single-muon reference sample. The trigger paths become fully efficient for  $p_T^{1st\,jet} \gtrsim 110$  GeV and  $\cancel{E}_T \gtrsim 220$  GeV [82]. However, it can be seen in Fig. III.5.1 that for a selection of  $\cancel{E}_T > 220$  GeV more than 99% of the signal events are rejected.

In order to achieve a reasonable signal acceptance, this search imposes, therefore, a trigger selection closer to the intrinsic trigger thresholds. The trigger selection is as follows:

- ❖ There is at least one jet within  $|\eta| < 2.4$  with transverse momentum larger than 110 GeV which fulfils the above mentioned jet noise cleaning criteria:  $p_T^{1st\,jet} > 110$  GeV.
- ❖ The missing transverse momentum must be larger than 100 GeV:  $\cancel{E}_T > 100$  GeV

These requirements result in an efficiency of 100% for the trigger requirements on the jet  $p_T$  and an efficiency of  $\sim 5 - 20\%$  for the trigger requirement on  $\cancel{E}_T$ , at the  $\cancel{E}_T$  thresholds [82]. Throughout the following sections, these trigger related requirements will be referred to as “trigger selection”.

Because of the huge cross section, QCD-multijet events are frequently produced at the LHC. Due to jet energy mismeasurements, they can also contribute to data samples recorded with MET triggers. Therefore, special requirements are enforced in order to suppress events emerging from QCD-multijet processes. QCD-multijet events can be

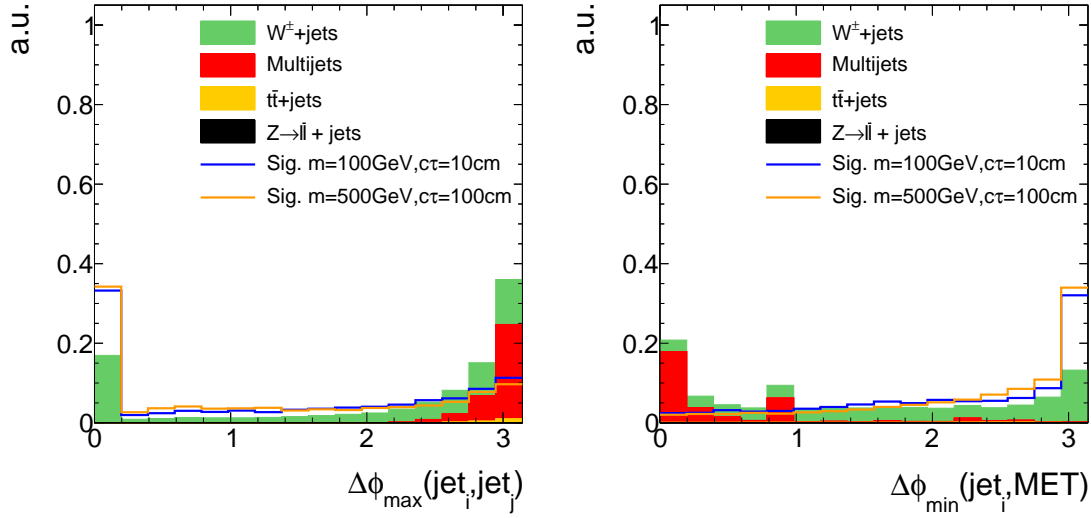


Figure III.5.2: Maximum  $\Delta\phi$  between any of two jets (left) and the minimum  $\Delta\phi$  between the  $\cancel{E}_T$  vector and any of the two leading jets (right) normalised to unit area after trigger selection. Only jets with  $p_T > 20$  GeV and  $|\eta| < 4.5$  are considered.

characterised by topologies where two jets are almost back-to back. Additionally, in QCD-multijet events the missing energy is usually aligned with one of the leading jets in the event. Figure III.5.2 shows the maximum  $\Delta\phi$  of any of two jets ( $p_T > 20$  GeV,  $|\eta| < 4.5$ ) and the minimum  $\Delta\phi$  between the  $\cancel{E}_T$  vector and any of the two leading jets for the SM background and two different signal datasets.

The following two requirements are sufficient to suppress QCD-multijet events efficiently:

- ❖  $\Delta\phi$  between any of two jets (with  $p_T > 20$  GeV and  $|\eta| < 4.5$ ) in the event must be smaller than 2.5.
- ❖  $\Delta\phi$  between any of the two leading jets (with  $p_T > 20$  GeV and  $|\eta| < 4.5$ ) and the  $\cancel{E}_T$  must be larger than 0.5.

### III.5.2.2 Candidate track selection

After the reduction of background processes with event-based variables, a track-based selection is carried out. To get an optimised selection for possible chargino tracks several signal candidate track characteristics are exploited.

First, a selection of high-quality tracks is enforced:

- ❖ The track must be classified as “high purity” as defined in [70].

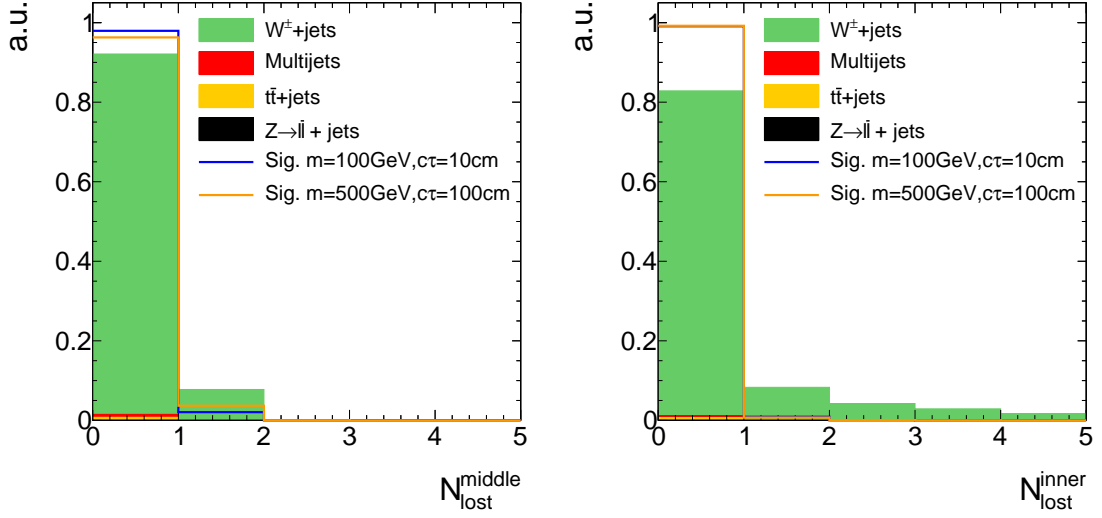


Figure III.5.3: Normalised number of missing middle (left) and inner (right) hits of background and signal tracks after trigger selection and QCD suppression cuts.

- ❖ The track is required to have no missing middle or inner hits:  $N_{\text{miss}}^{\text{middle/inner}} = 0$
- ❖ The radial and longitudinal distance of the track to the primary vertex must be small:  $|d0| < 0.02 \text{ cm}$ ,  $|dz| < 0.5 \text{ cm}$ .

In Figs. III.5.3 and III.5.4, the power of the latter two quality selection cuts is shown.

Furthermore, a first kinematic preselection is applied:

- ❖ Only tracks in the central region are considered :  $|\eta| < 2.1$ .
- ❖ Only tracks with a minimum transverse momentum of 20 GeV are considered:  
 $p_T > 20 \text{ GeV}$ .

In order to suppress background tracks emerging from SM processes, an electron, muon and tau veto is applied. This rejects tracks that are close to a reconstructed electron, muon or tau. Additionally, the candidate track must not be close to a jet ( $p_T > 20 \text{ GeV}$  and  $|\eta| < 4.5$ ):

- ❖ The track must not be within a cone of  $\Delta R < 0.15$  to a reconstructed standalone, tracker or global muon with a transverse momentum larger than 10 GeV (see Section ?? for details on the different muon definitions).



- ❖ The track must not be within a cone of  $\Delta R < 0.15$  to a reconstructed electron with a transverse momentum larger than 10 GeV (see Section ?? for details on the electron reconstruction).
- ❖ The track must not be within a cone of  $\Delta R < 0.15$  to a reconstructed tau with  $p_T > 20$  GeV and  $|\eta| < 2.3$  (see Section ?? for details on the tau reconstruction). Some loose isolation requirements are enforced to protect the tau reconstruction from jet contamination.
- ❖ The track must not be within a cone of  $\Delta R < 0.5$  to a reconstructed jet ( $p_T > 20$  GeV and  $|\eta| < 4.5$ ).

These lepton and jet veto selection requirements are highly suppressing the background emerging from real lepton/jet production like in  $W$ +jets events. The discrimination power of the lepton and jet vetos is shown in Fig. III.5.5 where the minimum  $\Delta R$  between the candidate track and a reconstructed electron, muon, tau or jet is shown.

Unfortunately, the lepton veto selection cuts are less effective in some of the detector directions. For example, the reconstruction of an electron easily fails in the direction of

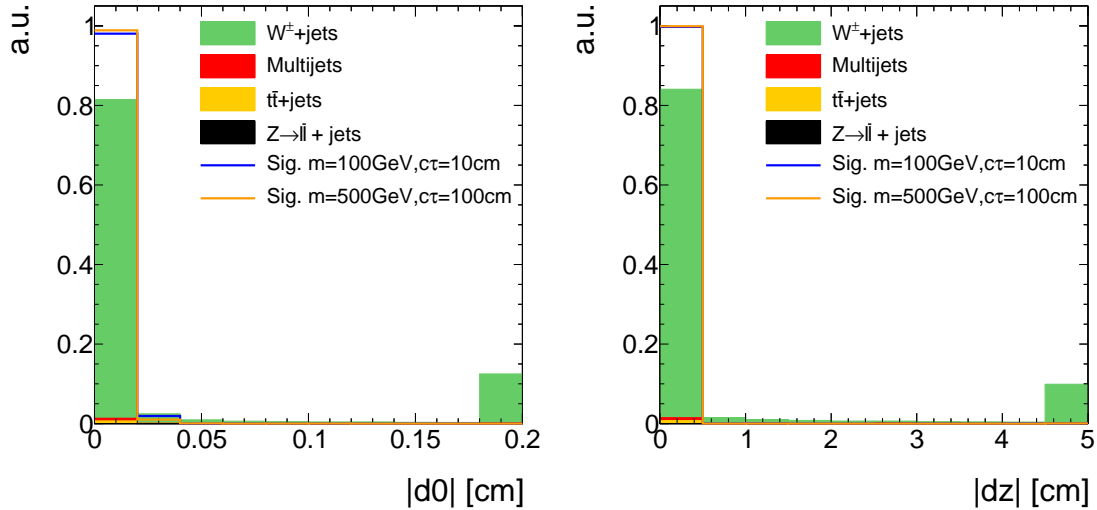


Figure III.5.4: Absolute value of the radial (left) and longitudinal (right) distance between the track and the primary vertex after trigger selection and QCD-multijet suppression cuts. All events with a candidate track with a radial (longitudinal) distance larger than 0.2 cm (5 cm) are contained in the last bin.

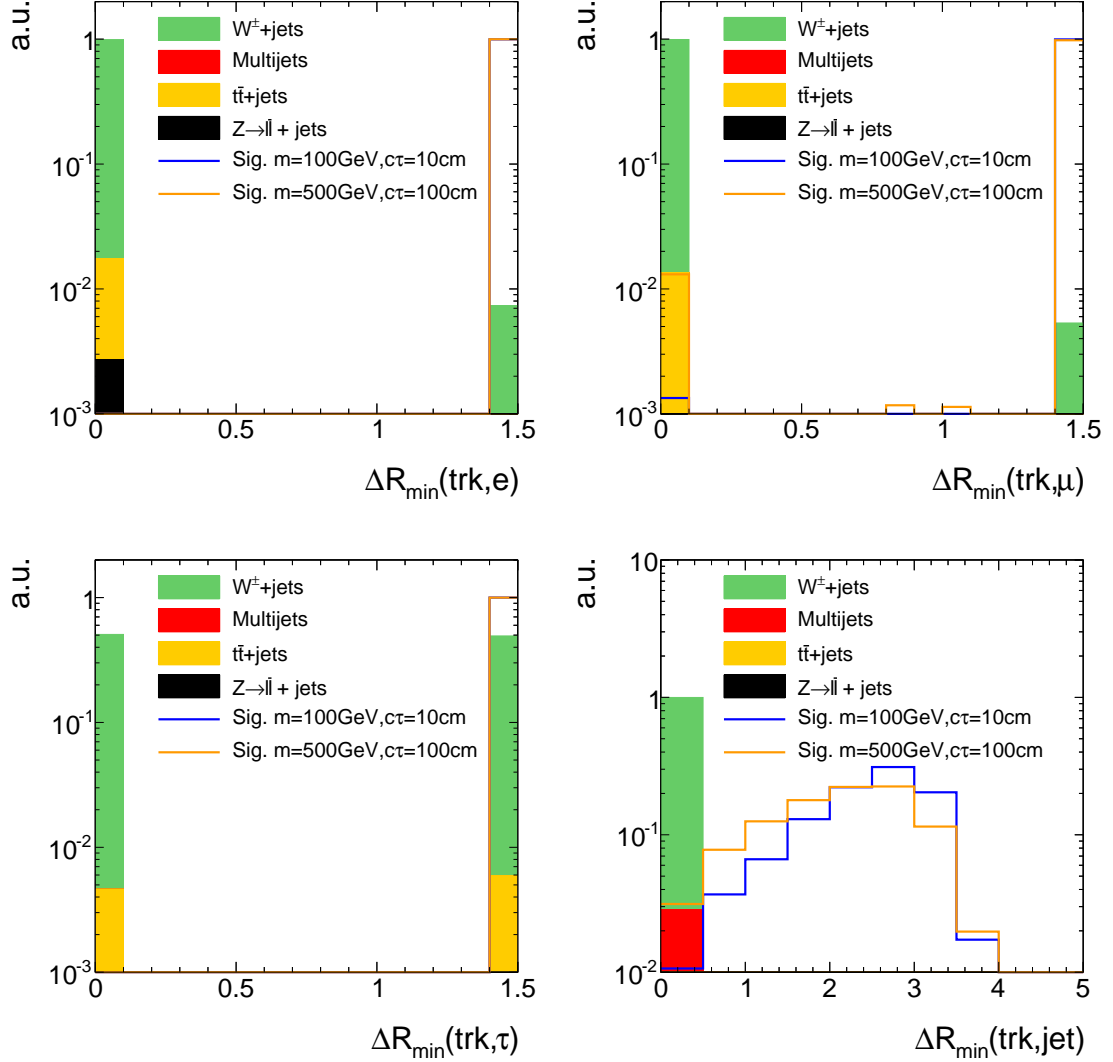


Figure III.5.5: The minimum  $\Delta R$  between the candidate track and a reconstructed electron (top left), muon (top right), tau (bottom left) or jet (bottom right) after the event-based selection and the high-quality, kinematic and lepton/jet veto selection of the candidate track selection but without the one shown in the corresponding plot (“N-1 plot”). The last bin contains all events where the candidate track has a  $\Delta R_{\min}$  larger than 1.5 or 5.0 to the next lepton or jet respectively. Events with no respective lepton or jet are also contained in the last bin.

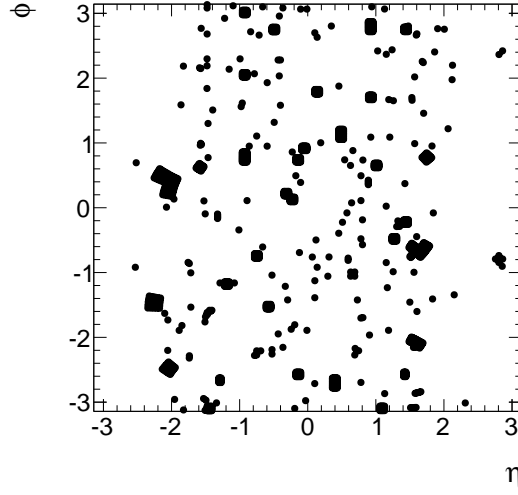


Figure III.5.6: Visualisation of dead and noisy ECAL cells in the detector's  $\phi - \eta$  plane according to [79,80]. The radius of the dots correspond to  $\Delta R = 0.05$ .

a dead ECAL cell. This reduces the discrimination power of the electron veto. For this reason, tracks that point towards dead or noisy ECAL cells are rejected. A general list of dead and noisy ECAL cells is provided centrally by the CMS collaboration. Further dead cells were identified within a study in [79,80] resulting in a total number of 1234 dead or noisy ECAL channels. These are illustrated in Fig. III.5.6 showing a map of all ECAL channels not considered in the search.

Additionally, tracks that point towards intermodule gaps of ECAL cells or to the ECAL barrel endcap gap at  $1.42 < |\eta| < 1.65$  are rejected. A list of the ECAL intermodule gaps, which is supplied centrally by CMS, is given in Table III.5.3.

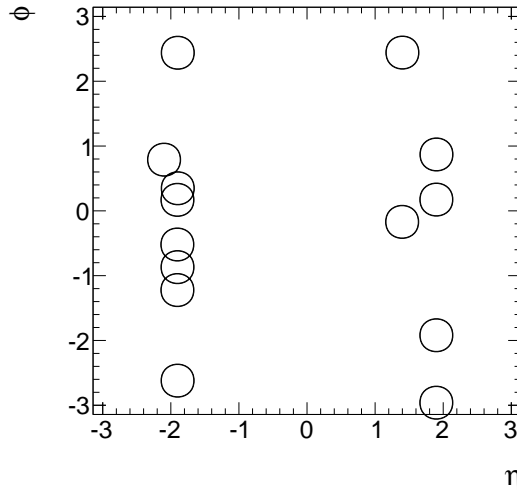
The muon reconstruction is less efficient for muons in detector regions with bad cathode strip chambers (CSC). These bad chambers are also identified centrally by the CMS collaboration and their  $\eta$  and  $\phi$  values are visualised in Fig. III.5.7. Thus, also tracks pointing towards these regions within a distance of  $\Delta R < 0.25$  are rejected.

To summarise, tracks pointing towards detector regions, that are not working properly or where the lepton reconstruction efficiencies are reduced, are vetoed as follows:

- ❖ Veto tracks within a cone of  $\Delta R < 0.05$  to a dead or noisy ECAL cell (visualised in Fig. III.5.6).
- ❖ Veto tracks that point towards the direction of the ECAL intermodule gap listed in Table III.5.3.
- ❖ Veto tracks that point towards a bad CSC within  $\Delta R < 0.25$  (visualised in Fig. III.5.7).

Table III.5.3: Intermodule ECAL gaps.

$\eta$ -ranges
$-1.14018 < \eta < -1.1439$
$-0.791884 < \eta < -0.796051$
$-0.44356 < \eta < -0.447911$
$0.00238527 < \eta < -0.00330793$
$0.446183 < \eta < 0.441949$
$0.793955 < \eta < 0.789963$
$1.14164 < \eta < 1.13812$

Figure III.5.7: Visualisation of the excluded region by the bad cathode strip chamber veto in the detector's  $\phi - \eta$ .

- ❖ Veto tracks that point towards the region between ECAL barrel and endcap at  $1.42 < |\eta| < 1.65$

Finally, two further characteristics of chargino tracks are exploited. As the chargino is produced in a very clean environment (no further particles around the chargino is expected), the isolation of the track can discriminate signal against background events.

Furthermore, for charginos decaying inside the tracker there is no associated energy deposition in the calorimeters in the direction of the track. This is a very pronounced characteristics of signal tracks.

The resulting selection cuts are as follows

- ❖ No further substantial track activity is allowed in a cone of  $\Delta R < 0.3$  around the candidate track:  $\sum_{\Delta R < 0.3} p_T^{\text{trk}}/p_T^{\text{cand}} - 1 < 0.1$
- ❖ No large calorimeter energy deposits (ECAL+HCAL) in a cone of  $\Delta R < 0.5$  around the track:  $E_{\text{calo}}^{\Delta R < 0.5} < 5 \text{ GeV}$ .

The discrimination power of these two variables is shown in Fig. III.5.8.

As emphasised before, this analysis aims at being sensitive especially on shorter lifetimes. Still, in order to allow for charginos decaying at any layer of the tracker, no explicit selection cut on the number of missing outer hits is required.

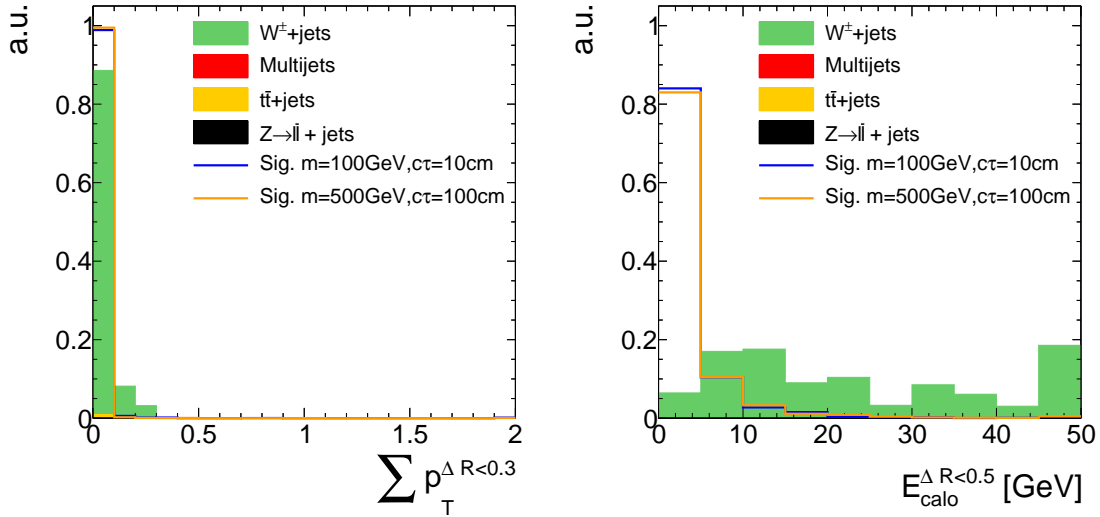


Figure III.5.8: Track isolation (left) and calorimeter energy deposits (right) of the candidate track after the full previous selection. All events with a track isolation or a calorimeter energy deposit larger than the range shown in the figures are contained in the last bin.

1582 Events are selected if they at least contain one track fulfilling all candidate track selection  
1583 requirements. An overview over the full analysis preselection is given in Table III.5.4.  
1584 The event yields after the selections of each of the categories from Table III.5.4 are listed  
1585 in Table III.5.5 for the simulated background samples, some exemplary simulated signal  
1586 models and for observed data. Detailed event yield tables can be found in Appendix ??.

1587

Table III.5.4: Summary and categorisation of the analysis selection.

Trigger	HLTMonoCentralPFJet80_PFMETnoMu95_NHEF0p95 HLTMonoCentralPFJet80_PFMETnoMu105_NHEF0p95 HLT_MET120_HBHENoiseCleaned	
Event-based selection	Trigger selection	$p_T^{1^{\text{st}} \text{jet}} > 110 \text{ GeV}$ with $ \eta_{1^{\text{st}} \text{jet}}  < 2.4$ , $\text{CHF}_{1^{\text{st}} \text{jet}} > 0.2$ , $\text{CEF}_{1^{\text{st}} \text{jet}} < 0.5$ , $\text{NHF}_{1^{\text{st}} \text{jet}} < 0.7$ , $\text{NEF}_{1^{\text{st}} \text{jet}} < 0.7$ $\cancel{E}_T > 100 \text{ GeV}$
	QCD suppression	$\Delta\phi_{\text{max}}(\text{jet}_i, \text{jet}_j) < 2.7$ for all jets with $p_T > 20 \text{ GeV}$ , $ \eta  < 4.5$ $\Delta\phi_{\text{max}}(\text{jet}_i, \cancel{E}_T) > 0.5$ for two leading jets
Candidate track selection	$\geq 1$ track that fulfils the following criteria:	
	Good quality selection	high-purity as defined in [70] $N_{\text{miss}}^{\text{middle/inner}} = 0$ $ d0  < 0.02 \text{ cm}$ $ dz  < 0.5 \text{ cm}$
	Kinematic selection	$ \eta  < 2.1$ $p_T > 20 \text{ GeV}$
	Lepton/jet veto	No muon within $\Delta R < 0.15$ No electron within $\Delta R < 0.15$ No tau within $\Delta R < 0.15$ No jet within $\Delta R < 0.5$ No dead/noisy ECAL cell within $\Delta R < 0.05$ Not within an ECAL intermodule gap Not within $1.42 <  \eta  < 1.65$ Not within $\Delta R < 0.25$ to a bad CSC
	Isolation selection	$\sum_{\Delta R < 0.3} p_T^{\text{trk}} / p_T^{\text{cand}} - 1 < 0.1$ $E_{\text{calo}}^{\Delta R < 0.5} < 5 \text{ GeV}$

Table III.5.5: Event yields in simulation and observed data after the selections of each of the categories from Table III.5.4

Selection	Simulated background samples				Simulated signal samples				Data
	$W + \text{jets}$	$t\bar{t} + \text{jets}$	$Z \rightarrow \ell\bar{\ell}$	Multijet	$m=100\text{GeV}$ $c\tau=10\text{ cm}$	$m=100\text{GeV}$ $c\tau=100\text{ cm}$	$m=500\text{GeV}$ $c\tau=10\text{ cm}$	$m=500\text{GeV}$ $c\tau=100\text{ cm}$	MET data
After skim	$9.16 \cdot 10^7$	$1.04 \cdot 10^6$	$2.21 \cdot 10^7$	$1.38 \cdot 10^{11}$	$3.41 \cdot 10^5$	$3.41 \cdot 10^5$	$3.46 \cdot 10^2$	$3.46 \cdot 10^2$	$1.07 \cdot 10^7$
Event-based selection:									
Trigger	$4.31 \cdot 10^6$	$1.15 \cdot 10^5$	$4.23 \cdot 10^3$	$4.32 \cdot 10^6$	$1.55 \cdot 10^4$	$1.49 \cdot 10^4$	$4.62 \cdot 10^1$	$4.62 \cdot 10^1$	$1.07 \cdot 10^7$
Trigger selection	$1.89 \cdot 10^6$	$5.31 \cdot 10^4$	$6.26 \cdot 10^2$	$9.63 \cdot 10^5$	$1.09 \cdot 10^4$	$9.83 \cdot 10^3$	$3.63 \cdot 10^1$	$3.57 \cdot 10^1$	$3.94 \cdot 10^6$
QCD suppression	$1.11 \cdot 10^6$	$6.76 \cdot 10^3$	$1.32 \cdot 10^2$	$9.55 \cdot 10^3$	$7.90 \cdot 10^3$	$6.98 \cdot 10^3$	$2.76 \cdot 10^1$	$2.71 \cdot 10^1$	$1.38 \cdot 10^6$
Track-based selection:									
Good quality selection	$1.07 \cdot 10^6$	$6.63 \cdot 10^3$	$1.32 \cdot 10^2$	$9.55 \cdot 10^3$	$2.80 \cdot 10^3$	$5.38 \cdot 10^3$	$5.07 \cdot 10^0$	$2.00 \cdot 10^1$	$1.30 \cdot 10^6$
Kinematic selection	$8.14 \cdot 10^5$	$5.63 \cdot 10^3$	$1.32 \cdot 10^2$	$5.48 \cdot 10^3$	$2.54 \cdot 10^3$	$4.93 \cdot 10^3$	$4.73 \cdot 10^0$	$1.89 \cdot 10^1$	$9.51 \cdot 10^5$
Lepton/jet veto	$5.02 \cdot 10^2$	$5.88 \cdot 10^0$	$0 \cdot 10^0$	$0 \cdot 10^0$	$1.99 \cdot 10^3$	$3.67 \cdot 10^3$	$3.83 \cdot 10^0$	$1.50 \cdot 10^1$	$6.16 \cdot 10^2$
Isolation selection	$3.19 \cdot 10^1$	$0.67 \cdot 0 \cdot 10^0$	$0 \cdot 10^0$	$0 \cdot 10^0$	$1.67 \cdot 10^3$	$3.04 \cdot 10^3$	$3.39 \cdot 10^0$	$1.26 \cdot 10^1$	$1.19 \cdot 10^2$



Given the presented signal candidate selection, two variables remain that are highly discriminating: The transverse momentum  $p_T$  and the energy release per path length  $dE/dx$  of the candidate track. In this analysis, the Asymmetric Smirnov discriminator  $I_{as}$  is used to enhance the discriminating power of  $dE/dx$ . See Section III.3.3 for the definition and a detailed explanation of  $I_{as}$ .

In Fig. III.5.9, the distribution of the remaining two variables are shown after the selection of signal candidate events. These variables are used to optimise the sensitivity of the search. The optimisation process will be explained in Section III.7. However, before the optimisation can be accomplished, a characterisation and estimation of the background is needed. This topic will be discussed in the following chapter.

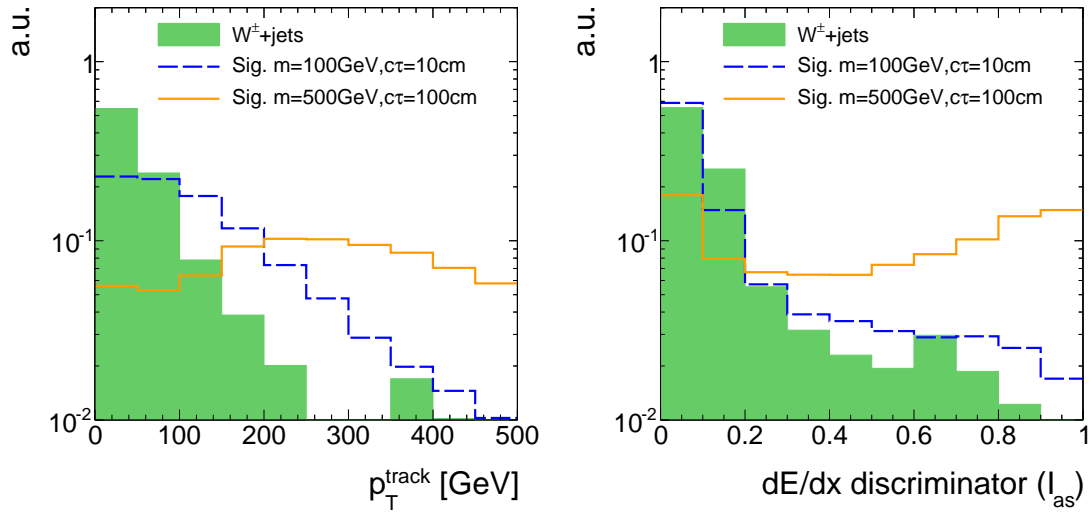


Figure III.5.9: Candidate track  $p_T$  (left) and  $I_{as}$  (right) after the full signal candidate selection for signal and  $W + \text{jets}$  events. Because of the low statistical precision of the  $W + \text{jets}$  sample, the trigger selection is not applied.

## III.6 Characterisation and estimation of the Standard Model backgrounds

After the application of the signal candidate selection, explained in the previous chapter, the background arising from Standard Model processes is dramatically reduced. Only two events in the simulated  $W + \text{jets}$  sample remain. One of these originates from an

unreconstructed muon, the other one from an unreconstructed electron, both passing the lepton vetoes. This implies, that the electron, muon, and tau vetoes cannot reject all leptons because some are not properly reconstructed. Due to the limited size of the simulated  $W + \text{jets}$  dataset (15 times smaller than the number of events expected from  $W + \text{jets}$  processes during 2012 data taking), it is not possible to rely on a full simulation-based estimation of the leptonic background. The underlying mechanism that a lepton can pass the lepton veto and the corresponding methods to estimate the leptonic background will be explained in detail in Section III.6.2.

Furthermore, there is the possibility that a track is reconstructed out of a set of hits that do not originate from only one single particle. Such tracks are called “fake tracks”. Background tracks arising from a combination of unrelated hits will be explained in the following Section III.6.1. It should be noted that the fake background is contributing through all SM processes, not only via  $W + \text{jets}$ . Still, as the characteristics of fake tracks are independent of the underlying process, this background can also be studied on simulation using  $W + \text{jets}$  events only.

There is no contribution of jets to the background, because jets are efficiently suppressed by the jet veto and the track isolation requirement of the signal candidate selection (see Table III.5.4).

The reader will recognise, that the importance of the two contributions to the background, the fake and leptonic background, is very different to this search. It will be seen, that the leptonic background is of negligible size.

However, both background are estimated in a similar approach. First, an inclusive background estimation (without the use of  $dE/dx$  information) is estimated. Afterwards, the efficiency of a  $dE/dx$  selection for the fake and leptonic background is determined.

Finally, the final signal regions are determined within an optimisation procedure. This optimisation is carried out in the track variables  $p_T$  and  $dE/dx$  (see Chapter III.7) to ensure an ideal selection for the search for short and highly ionising tracks.

### III.6.1 Fake background

Fake tracks are tracks that are reconstructed out of the tracker hits of more than one particle. The rate at which this false reconstruction occurs is highly restrained by the quality cuts on  $\chi^2$  and the vertex compatibility of the track reconstruction algorithm. Details on the reconstruction algorithm of tracks at CMS can be found in Section ??.

Reconstructed tracks that are fake tracks consist in general only out of a few hits. This can be seen in Fig. III.6.1, where the normalised distribution of the number of hits from fake tracks in simulated  $W + \text{jets}$  events is depicted. There are almost no fakes with more than seven hits. In simulation, fake tracks are defined as tracks that cannot be matched to a generator-level particle within a distance of  $\Delta R < 0.01$ .

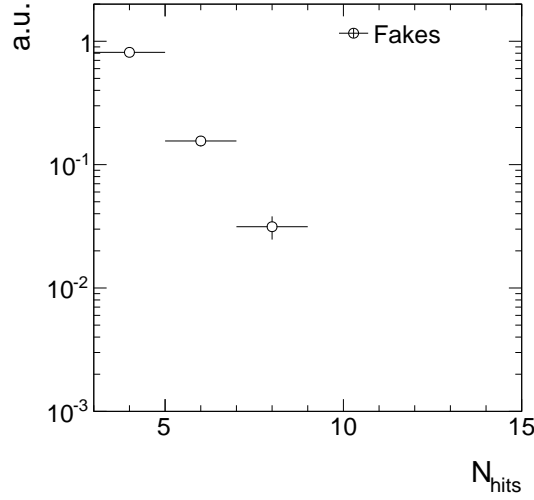


Figure III.6.1: Normalised distribution of the number of hits for fake tracks in the simulated  $W + \text{jets}$  sample. To increase the statistical precision, only the candidate track selection from Table III.5.4 is applied.

Fakes are efficiently suppressed by the requirements of no missing middle or inner hits and the compatibility with the primary vertex. Unfortunately, wrongly reconstructed tracks which pass these criteria, do also easily pass the  $E_{\text{calo}}^{\Delta R < 0.5} < 5 \text{ GeV}$  requirement with high efficiency, as fake tracks cannot be correlated to energy deposits in the calorimeters.

Fake tracks are mainly caused by the wrong combination of pileup tracks and electronic noise. This leads to the fact, that the occurrence of fake tracks across various background processes is stable, as will be seen later.

In this analysis, the estimation of the fake background is split into two parts. First, the background is determined inclusively in  $dE/dx$ . Second, the  $dE/dx$  ( $I_{\text{as}}$ ) distribution is estimated with the help of a fake enriched control region. This second step is needed to enable an optimisation in  $dE/dx$  (see Section III.7).

### III.6.1.1 Inclusive fake background estimation

The inclusive background estimation closely follows the background estimation method done in [79, 80]. It aims at determining the probability of having a fake track in an event that passes the full signal candidate selection (Table III.5.4) plus a potential additional  $p_T$  selection cut that is determined in an optimisation procedure (Section III.7). This probability will be called the fake rate  $\rho_{\text{fake}}$ . Within [79, 80], it was checked that the fake rate is constant for different processes. Thus, it is possible to determine  $\rho_{\text{fake}}$  with the help of one SM process and then generalise it to all SM background processes.

The inclusive fake background is estimated with the help of  $Z \rightarrow \mu\bar{\mu}$  and  $Z \rightarrow e\bar{e}$

events from data.  $Z \rightarrow \ell\bar{\ell}$  events can be selected with high purity by requiring two well reconstructed muons or electrons that are opposite in charge and for which the invariant mass is around the  $Z$ -boson mass of  $\sim 90$  GeV. As these events do not contain further leptons from the hard interaction (processes with a further lepton are negligible), any additional track is either a constituent of an ISR jet, a soft particle from pileup events or is a fake, reconstructed out of a combination of hits from several soft particles. Since the candidate track selection requires a track with a  $p_T > 20$  GeV that is no lepton or jet, it suppresses ISR jets and soft tracks from the underlying event. Thus, applying the track-based signal candidate selection on  $Z \rightarrow \ell\bar{\ell}$  events selects fake tracks with high purity.

The selection of two well reconstructed muons and electrons is done with the single-muon and single-electron datasets listed in Table III.6.1. These datasets contain at least one muon or one electron in every event. For the  $Z \rightarrow \mu\bar{\mu}$  selection, an event is required to have two muons with  $p_T > 25$  GeV and  $|\eta| < 2.4$ . To suppress background from cosmic muons, the distance from the primary vertex must be less than  $|d_0| < 0.2$  cm in radial and  $|dz| < 0.5$  cm in longitudinal direction. In order to suppress background arising from jets that fake muons, various quality criteria are applied: it is required that there is at least one hit in the muon detector that is considered in the global muon fit, and that at least two measurements are from different muon detector stations. Concerning the track of the muon in the silicon tracker system, at least six hits in the full tracker system of which at

Table III.6.1: Datasets used for the determination of the fake rate.

Dataset	Integrated luminosity [ $\text{fb}^{-1}$ ]
/SingleMu/Run2012A-22Jan2013-v1/AOD	0.876
/SingleMu/Run2012B-22Jan2013-v1/AOD	4.405
/SingleMu/Run2012C-22Jan2013-v1/AOD	7.040
/SingleMu/Run2012D-22Jan2013-v1/AOD	7.369
/SingleElectron/Run2012A-22Jan2013-v1/AOD	0.876
/SingleElectron/Run2012B-22Jan2013-v1/AOD	4.412
/SingleElectron/Run2012C-22Jan2013-v1/AOD	7.050
/SingleElectron/Run2012D-22Jan2013-v1/AOD	7.368

least one pixel hit is required. An isolation criterion is applied that requires the sum of transverse momenta of all particle-flow particles in a cone of  $\Delta R < 0.4$  around the muon to be less than 12% of the muon  $p_T$ . Finally, the muons are required to be opposite in charge and to have an invariant mass between 80 to 100 GeV. The  $Z \rightarrow \mu\bar{\mu} + \text{fake track}$  selection is summarised in Table III.6.2.

In order to select  $Z \rightarrow e\bar{e}$  events in data, the two electrons are required to have  $p_T > 25 \text{ GeV}$ ,  $|\eta| < 2.5$  and no missing hits in the inner layers of the tracker. Furthermore, the electrons need to pass a conversion veto as described in [84] in order to reduce background arising from photon conversions. An isolation requirement similar to the muon isolation criterion is applied with an increased threshold of 15%. The electron identi-

Table III.6.2: Event selection cuts for the  $Z \rightarrow \mu\bar{\mu} + \text{fake}$  control sample to estimate the inclusive fake background.

Event-based selection	<p>Two global muons with <math>p_T &gt; 25 \text{ GeV}</math></p> <p><math> \eta  &lt; 2.4</math></p> <p><math>\sum_{\Delta R &lt; 0.4} p_T^{\text{PF particle}} / p_T(\mu) &lt; 0.12</math></p> <p><math>\frac{\chi^2}{ndof} \Big _{\text{global track}} &lt; 10</math></p> <p><math> d0  &lt; 0.2 \text{ cm}</math></p> <p><math> dz  &lt; 0.5 \text{ cm}</math></p> <p><math>\geq 1</math> hit in the muon detector considered in global fit</p> <p><math>\geq 2</math> hits in different muon stations</p> <p><math>\geq 1</math> hit in the pixel detector</p> <p><math>\geq 6</math> hits in the tracker system</p> <p>Muons opposite in charge</p> <p><math>80 \text{ GeV} &lt; M_{\text{inv}}(\mu_1, \mu_2) &lt; 100 \text{ GeV}</math></p>
Candidate track selection	<p>Good quality selection</p> <p>Kinematic selection</p> <p>Lepton/jet veto</p> <p>Isolation selection</p>

cation is further based on a multivariate technique developed within [85] that exploits electron characteristics concerning the track quality, the ECAL cluster shapes, and the combination of the measurements in the tracker and in the ECAL. Again, the two electrons must be opposite in charge and their invariant mass must be between 80 – 100 GeV. A summary of the  $Z \rightarrow e\bar{e} + \text{fake track}$  event selection can be found in Table III.6.3.

When applying a  $Z \rightarrow \ell\bar{\ell}$  selection plus the candidate track selection, the selected tracks are mostly fakes. Whether this is indeed the case can be tested on simulated  $Z \rightarrow \ell\bar{\ell}$  events. As can be seen in Fig. III.6.2, a reasonable purity in fake tracks can be achieved by applying the candidate track selection on top of the  $Z \rightarrow \ell\bar{\ell}$  selection. In simulated  $Z \rightarrow \mu\bar{\mu}$  events, a purity of 88% is achieved, whereas in simulated  $Z \rightarrow e\bar{e}$  events a purity of 92% of fake tracks is achieved.

As already mentioned, the fake rate is defined as the probability that an event contains a fake track that fulfils the candidate track selection. Thus, for the  $Z \rightarrow \ell\bar{\ell}$  datasets it is defined as the number of events passing the full selection described in Table III.6.2 (Table III.6.3) divided by the number of events that pass only the event-based selection

Table III.6.3: Event selection cuts for the  $Z \rightarrow e\bar{e} + \text{fake control sample}$  to estimate the inclusive fake background.

Event-based selection	Two Electrons with	$p_T > 25 \text{ GeV}$
		$ \eta  < 2.5$
Event-based selection		$\sum_{\Delta R < 0.4} p_T^{\text{PF particle}} / p_T(e) < 0.15$
		pass conversion veto [84]
		no missing inner tracker hits
		good MVA electron as defined in [85]
	Electrons opposite in charge	
	$80 \text{ GeV} < M_{\text{inv}}(e_1, e_2) < 100 \text{ GeV}$	
Candidate track selection	Good quality selection	
	Kinematic selection	
	Lepton/jet veto	
	Isolation selection	

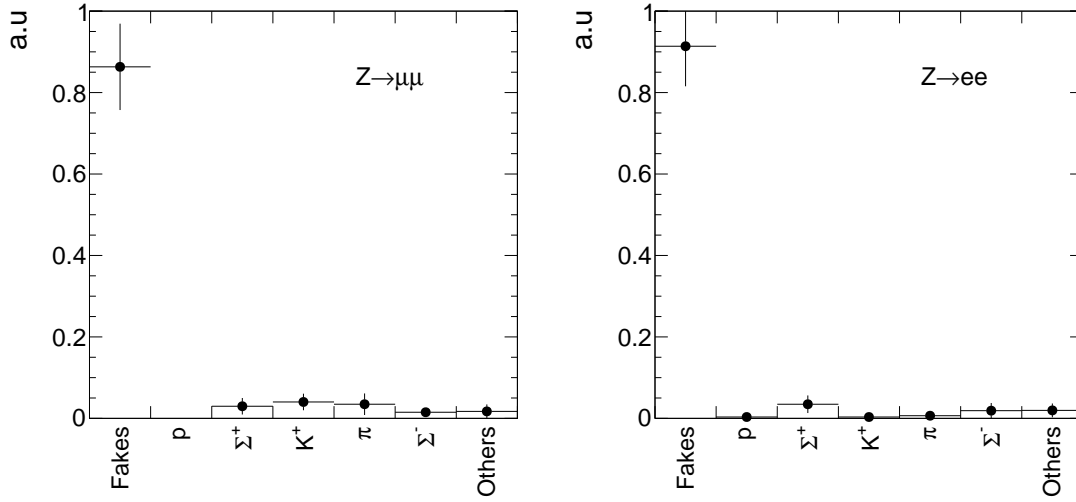


Figure III.6.2: Corresponding generator-level particles of all tracks within  $Z \rightarrow \ell\bar{\ell} + \text{fake}$  that were selected according to the candidate track selection. The full selection for tracks in  $Z \rightarrow \mu\bar{\mu}$  events (left) is given in Table III.6.2. The full selection for tracks in  $Z \rightarrow e\bar{e}$  events (right) is given in Table III.6.3. “Fake” means that no corresponding generator-level particle is found.

1706 in Table III.6.2 (Table III.6.3)

$$\rho_{\text{fake}} = \frac{N_{Z \rightarrow \ell\bar{\ell}}^{\text{cand trk selection}}}{N_{Z \rightarrow \ell\bar{\ell}}}$$

1707 Fake rates are determined independently for the  $Z \rightarrow \mu\bar{\mu} + \text{fake}$  and  $Z \rightarrow e\bar{e} + \text{fake}$  event  
 1708 selection and then averaged to obtain the final fake rate. The fake rate with the candidate  
 1709 track selection given in Table III.5.4 is  $(6.86 \pm 0.25) \cdot 10^{-5}$ . This is not the final result  
 1710 as the optimisation in  $p_T$  will add an additional  $p_T$  selection cut to the candidate track  
 1711 selection.

1712 As mentioned before, it was checked within [79, 80] that the fake rate is constant for  
 1713 different Standard Model processes. This is shown in Fig. III.6.3 where the fake rate is  
 1714 depicted for the most important SM processes. Since the fake rate is constant for different  
 1715 SM processes, the fake rate determined on the  $Z \rightarrow \ell\bar{\ell}$  dataset can be generalised for all  
 1716 SM background possibly contributing to this search. Thus, the inclusive fake background  
 1717 can be estimated by multiplying the fake rate with the number of events selected from the  
 1718 MET dataset (Table III.5.2) by applying the event-based signal candidate requirements  
 1719 from Table III.5.4

$$N_{\text{bkg}}^{\text{fake, inclusive in } I_{\text{as}}} = \rho_{\text{fake}} \cdot N_{\text{event-based selection}}^{\text{MET}}$$

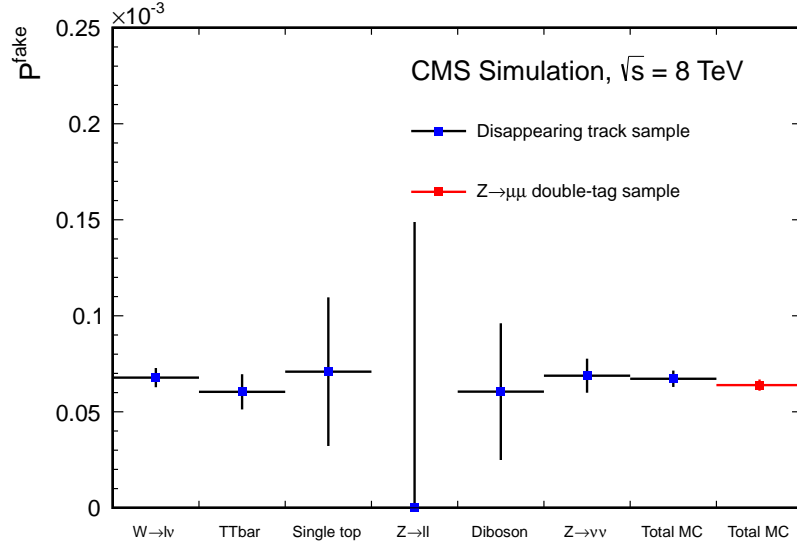


Figure III.6.3: Fake track rate estimated in [79, 80] for tracks with four hits. Taken from [80]

Given the number of events after the event-based selection of  $N_{\text{event-based selection}}^{\text{MET}} = 1.38 \cdot 10^6$  and the fake rate cited above, the inclusive fake background can be estimated to  $94.7 \pm 3.4$  for the candidate track selection.

It should be noted again that the inclusive fake background estimation will be only inclusive in  $I_{\text{as}}$  not in  $p_T$ . That means that after the definition of the signal region,  $N_{\text{bkg}}^{\text{fake, inclusive in } I_{\text{as}}}$  is determined with the additional optimal  $p_T$  selection.

Possible differences between the fake rate in  $Z \rightarrow \ell\bar{\ell}$  events and other SM processes are estimated on simulated events and taken into account as a systematic uncertainty (see Section III.6.4.1).

### III.6.1.2 $dE/dx$ shape of fake background

The information about the energy release per path length for fake tracks should not be taken from simulated samples as the simulation of  $dE/dx$  is not reliable (cf. Fig. III.3.8). Within this analysis the Asymmetric Smirnov discriminator  $I_{\text{as}}$  is used to discriminate signal against background with respect to  $dE/dx$  (see Section III.3.3). In order to estimate the  $I_{\text{as}}$  shape of fake tracks, a control region  $\text{CR}_{I_{\text{as}}}^{\text{fake}}$  is defined that is enriched with fakes and shows the same  $I_{\text{as}}$  distribution as fake tracks in the signal region.

To enrich fake tracks, it is possible to invert the selection cuts on the number of missing middle and inner hits, i.e. requiring at least one missing inner or middle hit ( $N_{\text{miss}}^{\text{inner}} + N_{\text{miss}}^{\text{middle}} > 0$ ). Figure III.6.4 shows the distribution of the number of missing



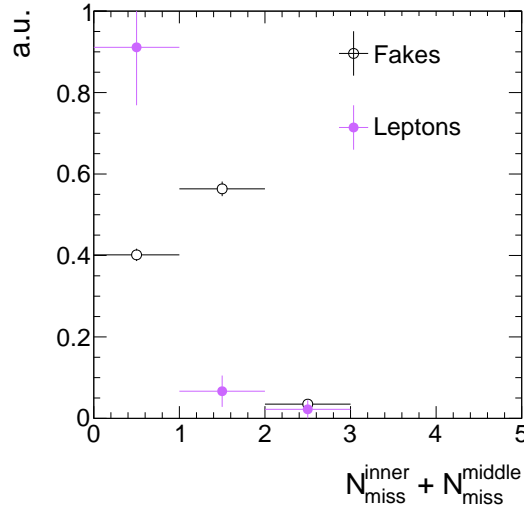


Figure III.6.4: Normalised number of missing inner plus missing middle hits for fake and leptonic tracks for the full candidate track selection with the selection requirements on  $N_{\text{miss}}^{\text{inner}}$  and  $N_{\text{miss}}^{\text{middle}}$  removed. Trigger selection and QCD suppression cuts were removed to enhance the statistical precision.

inner plus missing middle hits for fake and leptonic tracks in simulated  $W + \text{jets}$  events. It can be seen that this selection is enriched by fakes. The resulting purity of fakes in  $\text{CR}_{I_{\text{as}}}^{\text{fake}}$  is about 98% (see Fig. III.6.5).

Additionally, it must be checked whether the  $I_{\text{as}}$  shape in  $\text{CR}_{I_{\text{as}}}^{\text{fake}}$  is nearly equal to the  $I_{\text{as}}$  shape in the signal region. As the exact definition of the signal region will be addressed during optimisation, this test is done for various  $p_{\text{T}}$  selection cuts.

The comparison of the  $I_{\text{as}}$  shape of fake tracks can only be done on simulation. Thus, simulated  $W + \text{jets}$  events are used to select fake tracks in both regions. A comparison of the shape for the candidate track selection and the  $\text{CR}_{I_{\text{as}}}^{\text{fake}}$  is shown in Fig. III.6.5.

The  $I_{\text{as}}$  shape is almost identical in the signal and in the control region which makes the definition of the control region perfectly suited for estimating the  $I_{\text{as}}$  shape from  $\text{CR}_{I_{\text{as}}}^{\text{fake}}$  in data. The remaining shape differences are taken into account as a systematic uncertainty (discussed in Section III.6.4.2).

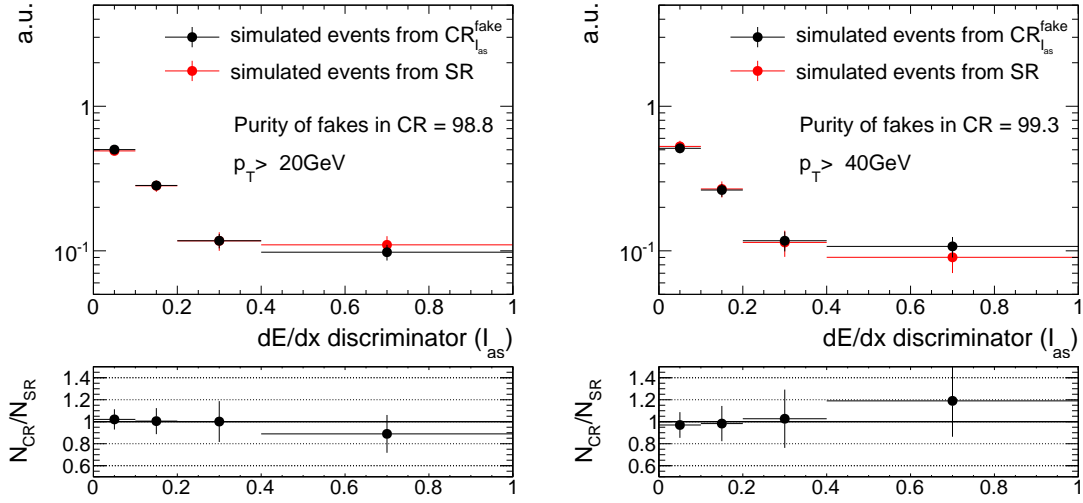


Figure III.6.5: Comparison of the  $I_{\text{as}}$  shape between  $\text{CR}_{I_{\text{as}}}^{\text{fake}}$  and the signal region for two different track  $p_T$  selections of  $p_T > 20$  GeV (left) and  $p_T > 40$  GeV (right). To enhance the statistical precision only the track-based selection is applied.

## III.6.2 Leptonic background

The leptonic background of the here presented search is caused by non-reconstructed leptons that circumvent the lepton veto selection. However, at least non-reconstructed electrons or taus should in principle deposit enough energy in the calorimeters such that they can still be vetoed by the calorimeter isolation requirement  $E_{\text{calo}}^{\Delta R < 0.5} < 5$  GeV. As muons don't deposit much energy in the calorimeters, this reasoning does not apply to them. In the following, the sources of the three different leptonic backgrounds are characterised.

### Electrons

To reject unreconstructed electrons, all tracks pointing to a dead or noisy ECAL cell, to an ECAL intermodule gap, or to the region between ECAL barrel and endcap at  $1.42 < |\eta| < 1.65$  are vetoed, as described in Section III.5.2. By this selection, almost all electrons are efficiently rejected.

However, there is still the possibility that an electron fails reconstruction and pass the signal candidate selection. This can happen either, if an electron do bremsstrahlung and the direction of the electron if significantly changed. Thus, the energy deposits in the ECAL can possibly not be matched to the original electron. Alternatively, there is also the possibility that an electron track is pointing towards a non-working ECAL cell, that is not included in the dead and noisy ECAL cell veto.

This possibility can be seen in the single event in the  $W + \text{jets}$  sample that pass the full

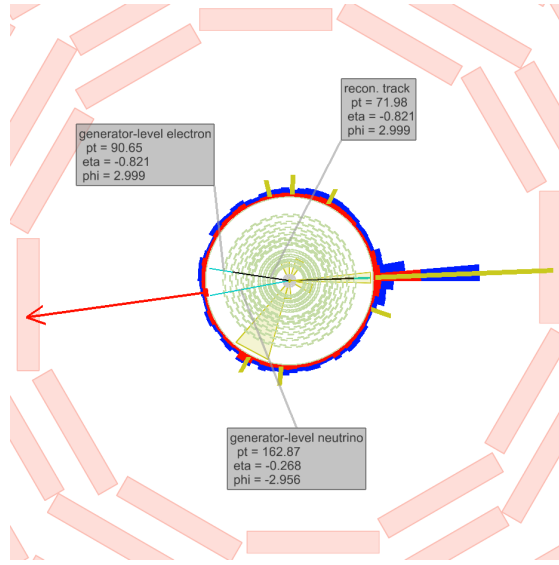


Figure III.6.6: Visualisation of a  $W \rightarrow e\nu_e$  event contributing to the SM background. In light blue, generator-level particles including  $e$  and  $\nu_e$  of the  $W$ -boson decay are shown. Black lines represent reconstructed tracks and the red arrow indicates the missing transverse energy in the event.

signal candidate selection and where the candidate track can be matched to a generator-level electron. This event is visualised in Fig. III.6.6. The neutrino, only weakly interacting does not show any signature in the detector, whereas the electron ( $p_T \simeq 90$  GeV) leaves a track with  $p_T \simeq 70$  GeV in the tracker. Only little ECAL energy deposits in the direction of the electron are visible. This is caused by the fact that one of the corresponding ECAL crystals is not working properly and thus no energy deposition can be recorded. An ISR jet ( $p_T \simeq 230$  GeV) causes the  $\cancel{E}_T$  in the event.

## Taus

Taus that decay hadronically are contributing to the leptonic background through the decay of a tau lepton to one charged pion  $\tau \rightarrow \pi^\pm \nu_\tau$ . Other hadronic decay modes of the tau lepton are suppressed by the track isolation criterion. Taus can fail reconstruction if they don't deposit energy in the HCAL or ECAL. Unreconstructed taus can therefore also easily bypass the calorimeter isolation criterion. Because of nuclear interactions in the tracker, pions often result in short reconstructed tracks that can easily be highly mismeasured in  $p_T$ . Thus, taus can contribute to the background even if imposing a tight selection in the transverse momentum.

Such an event is shown in Fig. III.6.7. The transverse momentum of the generator-level pion is only  $p_T \sim 10$  GeV, but because the reconstructed track is very short, it leads to a

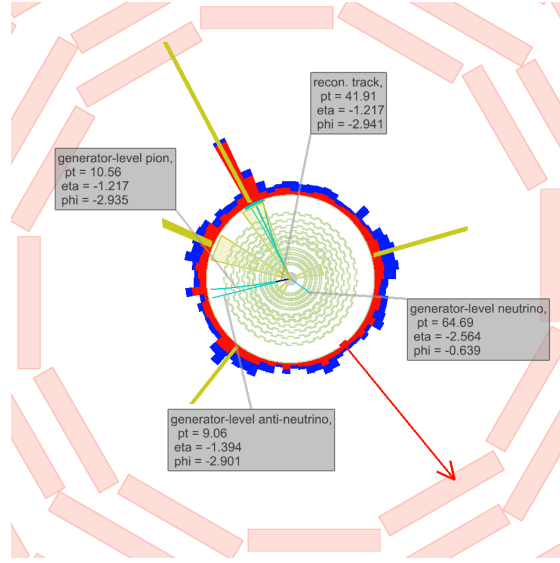


Figure III.6.7: Visualisation of a  $W^+ \rightarrow \tau^+ \nu_\tau \rightarrow \pi^+ \bar{\nu}_\tau \nu_\tau$  event contributing to the SM background. In light blue, the generator-level particles including  $\pi^+$ ,  $\bar{\nu}_\tau$  and  $\nu_\tau$  are shown. The black line represents the reconstructed pion track and the red arrow indicates the missing transverse energy in the event.

high mismeasurement of the track  $p_T$  of  $\sim 40$  GeV. The shortness of the track is caused by nuclear interactions of the pion. As no corresponding ECAL or HCAL energy deposits are measured, the reconstruction of the pion fails. The ISR jet causes the  $\cancel{E}_T$  in the event.

## Muons

Muons can fail reconstruction if they point towards a bad cathode strip chamber. This is taken into account in the candidate track selection. However, some of the muons still fail reconstruction if they fall within the gap between stations 0 and 1 of the drift tube system at  $|\eta| = 0.25$ . The muon reconstruction efficiency drops from around 99% to a value of around 94%, as shown in [79,80]. This possibility is illustrated in a simulated event shown in Fig. III.6.8. There, the muon is pointing to the  $\eta$ -region between stations 0 and 1 of the DT system. No signal in the muon chambers is visible. Therefore the muon could not be reconstructed.

In [79,80] events are rejected if the track is pointing in a region of  $0.15 < |\eta| < 0.35$ . In this search, this cut was omitted to maximise signal acceptance. Due to the additional selection in  $I_{as}$ , muons can be efficiently suppressed. E.g. in the event shown in Fig. III.6.8, the muon has an  $I_{as}$  value of about 0.007.

All of the three lepton types behave like MIPs. Thus, they loose much less energy

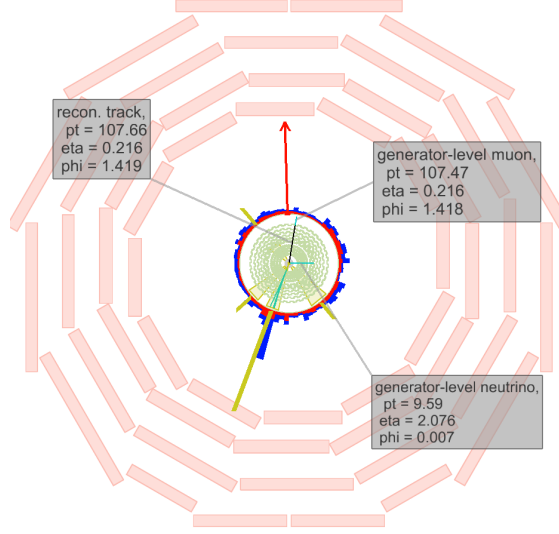


Figure III.6.8: Visualisation of an  $W \rightarrow \mu\nu_\mu$  event contributing to the SM background. In light blue, the generator-level particles including  $\mu$  and  $\nu_\mu$  of the  $W$  decay are shown.

than hypothetical new heavy particles and can therefore be further discriminated by their ionisation loss in the tracker system.

To have the possibility to make an optimisation in the two main discriminating variables  $p_T$  and  $I_{as}$ , the background estimation methods are designed to work for all different  $p_T$  and  $I_{as}$  selection cuts.

As for the fakes, the leptonic background estimation is splitted into two parts. First, the estimation of the inclusive background without  $I_{as}$  information. Second, the estimation of the  $I_{as}$  shape for all three leptonic background sources.

### III.6.2.1 Inclusive leptonic background estimation

The inclusive (without  $dE/dx$  information) lepton background estimation method is similar to the background estimation method used in [79,80].

In order to estimate the number of events in the signal region originating from leptons that pass the lepton veto, information from simulated events is used. With the help of simulated  $W + \text{jets}$  events, the ratio  $\rho_{MC}^{\text{lep}_i}$  between the number of events in the signal region with the selected track matched to a generator-level lepton  $N_{SR}^{\text{trk matched to lepton}_i}$  and the number of events in a control region  $N_{CR}^{\text{lepton}_i \text{ veto inverted}}$  with a inverted lepton veto is

determined. For muons, this lead to the following expression

$$\rho_{\text{MC}}^{\mu} = \frac{N_{\text{SR,MC}}^{\text{trk matched to } \mu}}{N_{\text{CR,MC}}^{\mu \text{ veto inverted}}}.$$

Since for electrons and taus the reconstruction efficiency is highly correlated with the  $E_{\text{calo}}^{\Delta R < 0.5}$  selection requirement, the  $E_{\text{calo}}^{\Delta R < 0.5}$  requirement is additionally removed in the control regions for these two lepton types

$$\rho_{\text{MC}}^{e,\tau} = \frac{N_{\text{SR,MC}}^{\text{trk matched to } e,\tau}}{N_{\text{CR,MC}}^{e,\tau \text{ veto inverted, } E_{\text{calo}}^{\Delta R < 0.5} < 5 \text{ GeV}}}.$$

In order to estimate the inclusive background for all three lepton types, the scale factor  $\rho_{\text{MC}}^{\text{lep}_i}$  is applied to the number of events in the lepton veto inverted control region measured in data. Also in data the control region for electrons and taus is defined with the  $E_{\text{calo}}^{\Delta R < 0.5}$  requirement removed. Thus, the inclusive number of predicted background events can be estimated with

$$N_{\text{predicted}}^{\mu, \text{ inclusive in } I_{\text{as}}} = \rho_{\text{MC}}^{\mu} \cdot N_{\text{CR,data}}^{\mu \text{ veto inverted}}.$$

for muons, and

$$N_{\text{predicted}}^{e,\tau, \text{ inclusive in } I_{\text{as}}} = \rho_{\text{MC}}^{e,\tau} \cdot N_{\text{CR,data}}^{e,\tau \text{ veto inverted, } E_{\text{calo}}^{\Delta R < 0.5} < 5 \text{ GeV}}.$$

for electrons and taus.

This method relies on the simulation of the lepton reconstruction efficiencies which is known to be reasonably accurate [86–88]. For electrons and taus the simulation of the calorimeter isolation is utilised as well. Possible discrepancies between simulation and data are taken into account as a systematic uncertainty via a comparison of the lepton reconstruction efficiencies in data and simulation in  $Z \rightarrow \ell\bar{\ell}$  events (see Section III.6.4.3).

To reduce the statistical uncertainty, the scale factor is calculated without applying the QCD suppression cuts. After the signal candidate selection described in Section III.5.2, only one event remains in the simulated  $W$  + jets sample where the candidate track can be matched to an electron. There are five events with a track candidate that can be matched to a muon, and no selected events have tracks that can be matched to a pion from a tau decay. The statistical uncertainties are calculated as the 68% upper and lower limits on the inclusive background with the Neyman procedure [18, 89]. Table III.6.4 gives the result for the prediction of the inclusive leptonic background for the signal candidate selection from Section III.5.2.

Table III.6.4: Scale factor  $\rho_{\text{MC}}^{\text{lep}_i}$ , number of events in the data control region  $N_{\text{CR,data}}$  and the resulting inclusive estimation  $N_{\text{predicted}}$  after the candidate track selection.

	$\rho_{\text{MC}}^{\text{lep}_i}$	$N_{\text{CR,data}}^{\text{veto inverted}}$	$N_{\text{predicted}}^{\text{inclusive in } I_{\text{as}}}$
electrons	$1.25^{+1.70}_{-0.77} \cdot 10^{-4}$	60067	$7.49^{+10.19}_{-4.63}$
muons	$2.17^{+1.65}_{-0.93} \cdot 10^{-4}$	76664	$16.64^{+12.64}_{-7.12}$
taus	$< 2.13 \cdot 10^{-2}$	445	$< 9.46$

### III.6.2.2 dE/dx shape of leptonic background

In order to get information about the  $I_{\text{as}}$  (see Section III.3.3) shape in the signal region of electrons, muons and taus, a control region should be found where the shape of the observable is at least similar to that in the signal region. The most natural control region, being the lepton veto inverted control region, cannot be used because the variable  $I_{\text{as}}$  differs between the signal and the control region, as can be seen in Fig. III.6.9. The discrepancies reach factors up to an order of magnitude.

Various other control regions were tested and could not be used because of too large  $I_{\text{as}}$  shape differences to the signal region.

As no suitable control region is known where the  $I_{\text{as}}$  shape of the leptons is at least similar to the shape in the signal region, it is decided to use the  $I_{\text{as}}$  information from

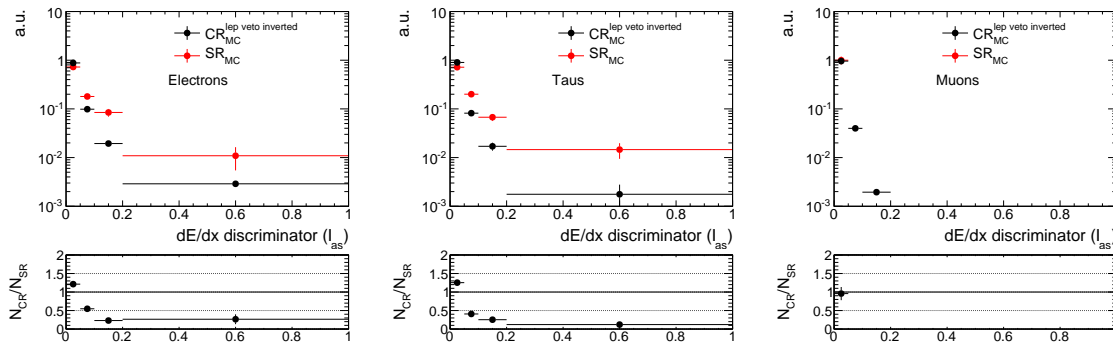


Figure III.6.9: Normalised  $I_{\text{as}}$  distribution for electrons (left), pions from the tau decay (middle) and muons (right) in the signal region (red) and the lepton veto inverted control region (black).

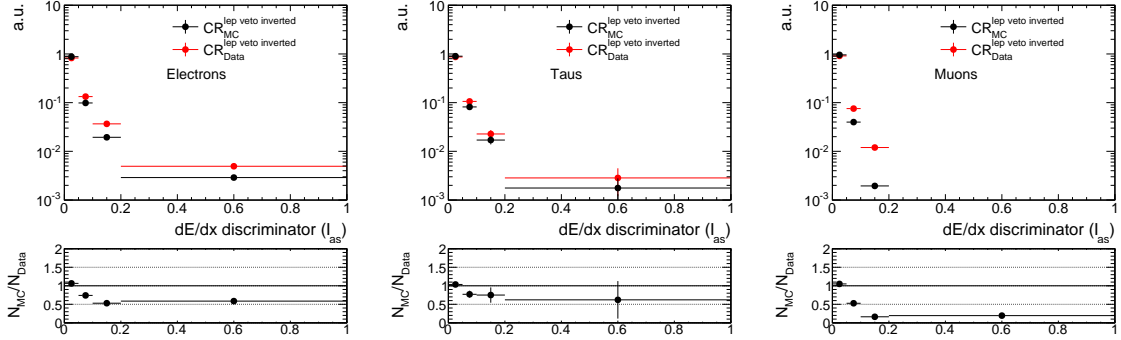


Figure III.6.10: Normalised  $I_{as}$  distribution for electrons (left), pions from the tau decay (middle) and muons (right) in the lepton veto inverted control region from simulated (black) and real (red) events.

simulation. This introduces a large bias since  $dE/dx$  (and therefore  $I_{as}$ ) is not simulated well. However, the corresponding bias is still smaller than the differences of the  $I_{as}$  shape between the signal and a control region: compare Fig. III.6.9 and Fig. III.6.10.

In order to take into account the bias when using  $I_{as}$  from simulation, a systematic uncertainty is estimated that addresses simulation-data differences of the  $I_{as}$  distributions. This systematic uncertainty is discussed in Section III.6.4.4.

### III.6.3 Background estimation validation

The background estimation methods are exhaustively validated in signal depleted control regions. Various control regions are used for validation. For each control region it has been verified that the signal contamination is less than the statistical uncertainty of the background prediction. For some of the models the expected number of events exceeds this limit. However, these models are already ruled out by the search for disappearing tracks [55] (see Appendix ??).

First, to validate the estimation method of the leptonic background, a leptonic control region is defined by selecting only tracks with a minimum number of seven hits in the tracker. This reduces the fake contribution to a negligible level (cf. Fig. III.6.1). Additionally in order to minimise signal contamination, the calorimeter isolation requirement is inverted to  $E_{calo}^{\Delta R < 0.5} > 10 \text{ GeV}$ . This requirement ensures no overlap to the signal region.

The validation test for the control region with  $E_{calo}^{\Delta R < 0.5} > 10 \text{ GeV}$  and  $N_{hits} > 6$  is shown in Table III.6.5. The predicted number of events by the leptonic background estimation is compatible with the observed data yield.

The fake background can only be estimated within the low calorimeter isolation region



Table III.6.5: Validation test of leptonic background estimation. Left:  $E_{\text{calo}}^{\Delta R < 0.5} > 10 \text{ GeV}$  and  $N_{\text{hits}} > 6$ . Right:  $E_{\text{calo}}^{\Delta R < 0.5} > 10 \text{ GeV}$ ,  $N_{\text{hits}} > 6$  and  $I_{\text{as}} > 0.2$ . Only statistical uncertainties are included.

	Predicted Yield	Data Yield		Predicted Yield	Data Yield
Total bkg	$131.70^{+26.30}_{-18.42}$	156	Total bkg	$0.0^{+0.50}_{-0.0}$	1
Electrons	$14.67^{+11.16}_{-6.29}$		Electrons	$0.0^{+0.07}_{-0.0}$	
Muons	$7.99^{+10.90}_{-5.00}$		Muons	$0.0^{+0.32}_{-0.0}$	
Taus	$109.04^{+21.18}_{-16.58}$		Taus	$0.0^{+0.38}_{-0.0}$	

( $E_{\text{calo}}^{\Delta R < 0.5} < 10 \text{ GeV}$ ) to ensure high fake purity. To be able to validate the method in the high calorimeter isolation region ( $E_{\text{calo}}^{\Delta R < 0.5} > 10 \text{ GeV}$ ), a translation factor from the low to the high calorimeter isolation region for the number of fake tracks is determined in the fake enriched control region  $\text{CR}_{I_{\text{as}}}^{\text{fake}}$  defined in Section III.6.4.2. In this control region, the ratio of  $N_{E_{\text{calo}}^{\Delta R < 0.5} > 10 \text{ GeV}} / N_{E_{\text{calo}}^{\Delta R < 0.5} < 10 \text{ GeV}}$  is estimated and taken as a multiplicative factor to the number of events predicted from the  $E_{\text{calo}}^{\Delta R < 0.5} < 10 \text{ GeV}$  region. In Table III.6.6, two different validation tests are shown, once an inclusive validation in  $I_{\text{as}}$  and once with an  $I_{\text{as}}$  selection of 0.2. Again, the predicted background events is in agreement with the number of observed events.

The whole validation is done for different selections in  $p_{\text{T}}$  and  $I_{\text{as}}$ . All validation tests show good agreement. Results of a variety of validation tests with different  $p_{\text{T}}$  and  $I_{\text{as}}$  selections can be found in Appendix ??.

Still, systematic uncertainties need to be estimated. The sources of systematic uncertainties and how they are estimated will be explained in the following section.

### III.6.4 Systematic uncertainties

Systematic uncertainties on the background estimation include:

- the uncertainty on the fake rate  $\rho_{\text{fake}}$ ;
- the uncertainty on the  $I_{\text{as}}$  shape of fake tracks predicted from a control region;
- the uncertainty on the leptonic scale factor  $\rho_{\text{MC}}^{\text{lep}_i}$  determined with simulated events;
- the uncertainty on the  $I_{\text{as}}$  shape of the leptonic background.

### III.6.4.1 Uncertainty on the fake rate

The fake rate  $\rho_{\text{fake}}$  is determined with the help of observed  $Z \rightarrow \ell\bar{\ell}$  events. To estimate the uncertainty on this fake rate caused by differences in the fake rate between different underlying processes, a comparison between the fake rate in simulated  $Z \rightarrow \ell\bar{\ell} + \text{jets}$  and simulated  $W + \text{jets}$  events is done. The fake rate in the  $Z \rightarrow \ell\bar{\ell} + \text{fake track control}$  samples (see Tables III.6.2 and III.6.3) and the fake rate in the signal candidate selection from Table III.5.4 in  $W + \text{jets}$  events are compared.

Unfortunately, the statistical precision of the simulated  $W + \text{jets}$  dataset is limited. Thus, the estimation of the systematic uncertainty is mainly driven by statistical uncertainties. In order to enhance the statistical precision of the estimation, the selection requirements on  $\cancel{E}_T$  and  $p_T^{1^{\text{st jet}}}$  are loosened and the QCD suppression requirements are removed. These variables are not expected to be correlated with the fake rate and thus should not affect it. That this is indeed the case, can be seen in Table III.6.7.

The systematic uncertainty is estimated as the largest difference from one of the ratio  $\rho_{\text{fake}}^{W+\text{jets}}/\rho_{\text{fake}}^{Z \rightarrow \ell\bar{\ell}}$  and its statistical uncertainty. For the candidate track selection, this is estimated to  $\rho_{\text{fake}}^{W+\text{jets}}/\rho_{\text{fake}}^{Z \rightarrow \ell\bar{\ell}} = 0.96 \pm 0.16$  leading to a systematic uncertainty on the fake rate of 20%.

### III.6.4.2 Uncertainty on the dE/dx shape of fake tracks

The systematic uncertainty on the shape of the  $I_{\text{as}}$  distribution takes into account the differences between the  $I_{\text{as}}$  shape in the fake control region  $\text{CR}_{I_{\text{as}}}^{\text{fake}}$  and in the signal region. For the estimation, information from simulated  $W + \text{jets}$  events is used. A comparison

Table III.6.6: Validation test of fake and leptonic background estimation methods. Left:  $E_{\text{calo}}^{\Delta R < 0.5} > 10 \text{ GeV}$ . Right:  $E_{\text{calo}}^{\Delta R < 0.5} > 10 \text{ GeV}$  and  $I_{\text{as}} > 0.2$ . Only statistical uncertainties are included.

	Predicted Yield	Data Yield		Predicted Yield	Data Yield
Total bkg	$309.00^{+33.46}_{-26.62}$	324	Total bkg	$14.80^{+2.92}_{-2.85}$	16
Electrons	$59.92^{+16.11}_{-11.85}$		Electrons	$0.75^{+0.36}_{-0.25}$	
Muons	$8.04^{+10.97}_{-5.03}$		Muons	$0.00^{+0.32}_{-0.00}$	
Taus	$173.06^{+24.62}_{-20.23}$		Taus	$2.33^{+0.74}_{-0.55}$	
Fakes	$67.98^{+11.57}_{-11.57}$		Fakes	$11.72^{+2.79}_{-2.79}$	

Table III.6.7: Fake rates in simulated  $W + \text{jets}$  and  $Z \rightarrow \ell\bar{\ell} + \text{jets}$  events for different event-based selections of the  $W + \text{jets}$  sample. The track-based selection is the candidate track selection from Table III.5.4.

$W + \text{jets}$ selection	$\rho_{\text{fake}}^{W+\text{jets}}$	$\rho_{\text{fake}}^{Z \rightarrow \ell\bar{\ell}}$
$\cancel{E}_T > 100 \text{ GeV}, p_T^{1\text{st jet}} > 110 \text{ GeV}$	$(3.16^{+4.26}_{-1.94}) \cdot 10^{-5}$	$(3.17 \pm 0.21) \cdot 10^{-5}$
$\cancel{E}_T > 0 \text{ GeV}, p_T^{1\text{st jet}} > 70 \text{ GeV}$	$(3.03 \pm 0.68) \cdot 10^{-5}$	$(3.17 \pm 0.21) \cdot 10^{-5}$
$\cancel{E}_T > 0 \text{ GeV}, p_T^{1\text{st jet}} > 70 \text{ GeV}$ , no QCD cuts	$(3.05 \pm 0.44) \cdot 10^{-5}$	$(3.17 \pm 0.21) \cdot 10^{-5}$

between the simulated  $I_{\text{as}}$  shape in the signal and in the control region can be seen in Fig. III.6.11. To enhance the statistical precision only track-based selection cuts are applied.

The largest deviation from one of the ratio of the number of events in the signal region and the control region with its 1-sigma statistical uncertainty is taken as systematic uncertainty. For a signal region definition with  $p_T > 20 \text{ GeV}$  and  $I_{\text{as}} > 0.2$  this corresponds to an uncertainty of around 21% and for a definition with  $p_T > 40 \text{ GeV}$  and  $I_{\text{as}} > 0.2$  of around 25%.

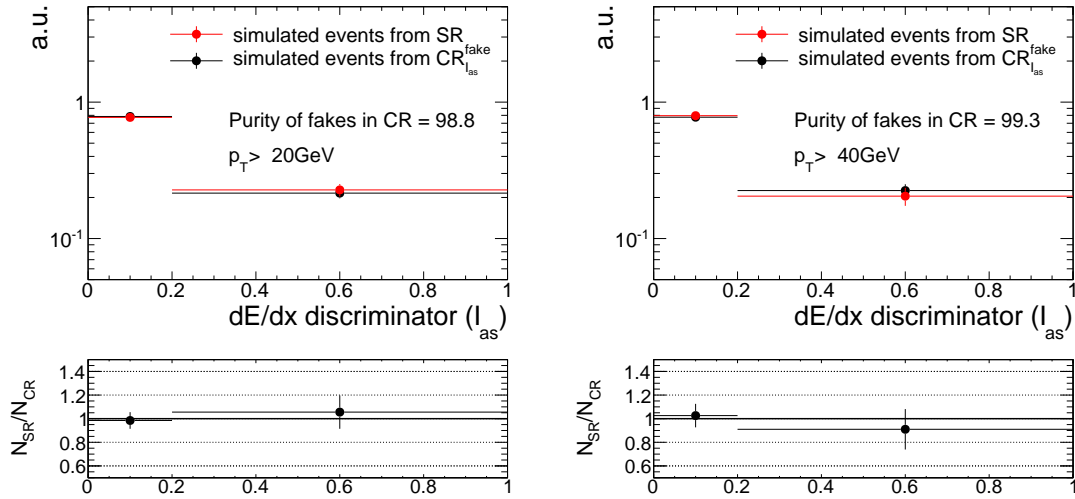


Figure III.6.11: Normalised distributions of the  $I_{\text{as}}$  shape of fake tracks in the signal and control region of simulated  $W + \text{jets}$  events with a  $p_T$  selection of 20 GeV (left) and a 40 GeV (right).

### III.6.4.3 Uncertainty on the leptonic scale factor

The leptonic scale factor  $\rho_{\text{MC}}^{\text{lep}_i}$  is estimated on simulated  $W$ +jets events. The corresponding systematic uncertainty that addresses the use of information from simulation is derived by a “tag-and-probe” method conducted on real data and simulated events.

For this method a selection of  $Z \rightarrow \ell\bar{\ell}$  events is done with one “tagged” well reconstructed lepton and one “probed” candidate track. To ensure a selection of  $Z \rightarrow \ell\bar{\ell}$  events, a selection on the invariant mass of the reconstructed lepton and the candidate track is applied with  $80 \text{ GeV} < M_{\text{inv}}(\text{lepton, cand. trk}) < 100 \text{ GeV}$  for muons and electrons. For taus, a muon from a  $\tau \rightarrow \mu\nu\nu$  decay is selected with  $40 \text{ GeV} < M_{\text{inv}}(\mu, \text{cand. trk}) < 75 \text{ GeV}$  and  $m_T(\mu, \cancel{E}_T) < 40 \text{ GeV}$  [79, 80]. Furthermore, the candidate track and the lepton are required to be opposite in charge. In order to reduce the contamination of fakes in the “tag-and-probe” samples an additional selection on the number of hits of  $N_{\text{hits}} > 5$  is required.

The “tag-and-probe” selection is done for each lepton type separately. In order to determine the leptonic scale factors, the number of events is once estimated for the candidate track selection including the corresponding lepton veto which gives the number of events in the “tag-and-probe” signal region  $N_{\text{SR}}^{\text{T\&P}}$ , and once inverting the lepton veto selection requirement which gives the number of events in the “tag-and-probe” lepton inverted control region  $N_{\text{CR, lepton veto inverted}}^{\text{T\&P}}$ . As for the determination of the tau and electron scale factor with simulated  $W$  + jets events, no requirement on the calorimeter isolation is applied in the lepton veto inverted control region for taus and electrons. This leads to the following expression of the lepton scale factor for muons

$$\rho^{\mu} = \frac{N_{\text{SR}}^{\text{T\&P}\mu}}{N_{\text{CR, } \mu \text{ veto inverted}}^{\text{T\&P}}}.$$

and for electrons and taus

$$\rho^{e,\tau} = \frac{N_{\text{SR}}^{\text{T\&P}e,\tau}}{N_{\text{CR, } e,\tau \text{ veto inverted}}^{\text{T\&P}}}.$$

The selection requirements for the three tag-and-probe samples are listed in Tables ??, ?? and ?? in Appendix ??.

The leptonic scale factors are calculated using simulated  $Z \rightarrow \ell\bar{\ell}$  events and real data from the single-muon and single-electron samples listed in Table III.6.1. The largest difference from unity of the ratio  $\rho_{\text{MC}}^{\text{lep}_i}/\rho_{\text{Data}}^{\text{lep}_i}$  and its statistical uncertainty is taken as systematic uncertainty. This results for the signal candidate selection in an uncertainty of 69% for the electron, 39% for the muon and 79 % for the tau scale factor.

#### III.6.4.4 Uncertainty on the leptonic $dE/dx$ shape

The uncertainty on lepton  $I_{as}$  shape is estimated by a comparison of the  $I_{as}$  shape in data and simulation in the lepton veto inverted control region. Figure III.6.12 shows the leptonic  $I_{as}$  distributions for all three lepton types in the lepton veto inverted control region in data and simulation. The largest difference from one of the ratio (and its statistical uncertainty) of the number of events in the control region in data and simulation is taken as systematic uncertainty. This leads for example to uncertainties between 37% – 81% for the signal candidate selection plus a selection requirement of  $I_{as} > 0.2$ .

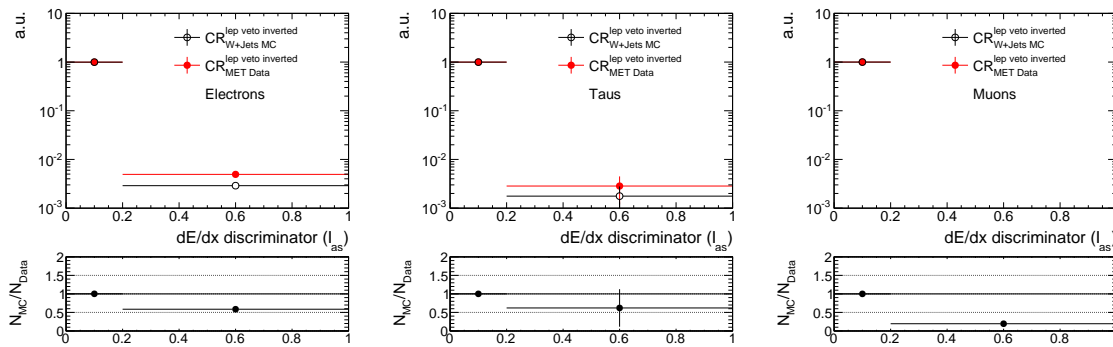


Figure III.6.12: Normalised distributions of the lepton  $I_{as}$  distributions in the lepton veto inverted control region for data (red) and simulation (black) for all three lepton types. The event-based selection requirements and the calorimeter isolation requirement are removed to enhance the statistical precision.

### III.7 Optimisation of the search sensitivity

Finally, having all background estimation methods in place, an optimisation procedure is conducted in order to increase the search sensitivity with respect to different signal models as introduced in Section III.4.2. The optimisation is done in the most sensitive variables,  $p_T$  and  $I_{as}$  (see Section III.3.3 for a definition and explanation of the Asymmetric Smirnov discriminator  $I_{as}$ ). A potential additional discriminating variable is the number of missing outer hits  $N_{lost}^{outer}$  in the tracker system. This variable is, however, not considered in this analysis because the discriminating potential for this search is limited, as shown in Appendix ??.

SUSY models with different chargino lifetimes and masses are characterised by different

1981  $p_T$  and  $I_{as}$  distributions as well as different theoretical cross sections. Therefore, the usual  
 1982 search optimisation strategy that maximises  $N_S/\Delta B$  ( $N_S$  = number of signal events of  
 1983 model  $S$ ,  $\Delta B$  = background uncertainty) implies a potential fine-tuning on the specific  
 1984 SUSY cross sections. In order to keep the search as general as possible, a cross section  
 1985 independent optimisation is performed. This is achieved by a minimisation of the cross  
 1986 section for which a  $5\sigma$ -discovery ( $\kappa = 5$ ) of the corresponding signal model is expected,  
 1987 i. e. finding the optimal selection cuts for  $p_T$  and  $I_{as}$  for which the lowest possible cross  
 1988 section,  $\sigma_{\min}$ , can be discovered

$$\kappa = \frac{\alpha_{\min} \cdot N_S(\text{mass}, c\tau, p_T^{\text{cut}}, I_{as}^{\text{cut}})}{\Delta B(p_T^{\text{cut}}, I_{as}^{\text{cut}})} = 5. \quad \text{with } \alpha_{\min} = \frac{\sigma_{\min}}{\sigma_S}. \quad (\text{III.7.1})$$

1989 The number of expected events  $N_S$  of the signal model  $S$  depends on the  $p_T$  and  $I_{as}$  se-  
 1990 lection cut as well as the mass and the lifetime of the chargino. The uncertainty on the  
 1991 background  $\Delta B$  is dependent on the  $p_T$  and  $I_{as}$  cut, and takes into account the full system-  
 1992 atic uncertainty as well as the statistical uncertainty on the background prediction which is  
 1993 defined as the 68% one sided upper limit of a Poisson distribution with  $\mu = N_B$  estimated  
 1994 with the Neyman construction [18, 89]. The systematic uncertainty on the background  
 1995 prediction includes systematic uncertainties as described in Section III.6.4, and statistical  
 1996 uncertainties arising from limited statistical precision of the control regions and simulated  
 1997 samples used in the background estimation. The factor  $\alpha_{\min}$  that is minimised is the ratio  
 1998 of the minimum cross section  $\sigma_{\min}$  divided by the nominal cross section  $\sigma_S$  of the signal  
 1999 model  $S$ .

2000

2001 As this analysis focuses on short tracks, rather low lifetimes are considered in the opti-  
 2002 misation procedure:  $c\tau = 1$  cm, 10 cm, 50 cm. These lifetimes are further suitable as they  
 2003 lie at the edge of the sensitivity of the search for disappearing tracks [55]. To cover the full  
 2004 mass space, the optimisation is done for masses between 100 GeV and 500 GeV in steps of  
 2005 100 GeV.

2006 The corresponding results are shown in Table III.7.1. It can be seen that the optimal  
 2007 selection is highly dependent on the signal models. The best sensitivity for low masses  
 2008 ( $\leq 200$  GeV) is mainly achieved by soft selection cuts in  $p_T$  between 20 to 30 GeV, while  
 2009 models with higher chargino masses require tighter  $p_T$  selections of around 50 GeV. The  
 2010 optimal  $I_{as}$  selection is mostly dependent on the mass of the chargino. For low masses  
 2011 and low lifetimes a soft selection in  $I_{as} > 0.05$  is preferred. Since for longer lifetimes more  
 2012 charginos are able to reach the tracking system, a tighter selection in  $I_{as}$  of 0.3 is prefer-  
 2013 able. Additionally, signal models with longer chargino lifetimes have a more pronounced  
 2014 right tail in the  $I_{as}$  distribution (cf. Fig. III.3.9 (right)). For high masses the highest  
 2015 search sensitivity is always achieved by a high  $I_{as}$  selection cut of 0.3.

Table III.7.1: Optimal  $p_T$  and  $I_{\text{as}}$  selection cuts and the corresponding minimum cross section  $\sigma_{\text{min}}$  that can be discovered with  $5\sigma$  significance for different signal models. For some signal samples, an optimisation result is not available due to the limited size of these samples.

Mass [GeV ]	Lifetime [cm ]	Optimal $p_T$ cut	Optimal $I_{\text{as}}$ cut	$\sigma_{\text{min}}$
100	1	30	0.05	61.596
200	1	20	0.05	43.414
300	1	n/a	n/a	n/a
400	1	n/a	n/a	n/a
500	1	n/a	n/a	n/a
100	10	30	0.05	1.531
200	10	30	0.30	0.561
300	10	30	0.30	0.354
400	10	30	0.30	0.238
500	10	50	0.30	0.201
100	50	50	0.30	0.435
200	50	50	0.30	0.110
300	50	50	0.30	0.063
400	50	50	0.30	0.045
500	50	50	0.30	0.037

2016

2017 In order to visualise the mass and  $c\tau$  dependence of the optimal  $p_T$  and  $I_{\text{as}}$  selection, the  
2018 optimisation results for two very different lifetimes (5 cm and 50 cm) and masses (100 GeV  
2019 and 500 GeV) are shown in Fig. III.7.1, where the minimum cross section that is possi-  
2020 ble to discover is shown in the  $p_T - I_{\text{as}}$  plane. For the visualisation, general systematic  
2021 uncertainties on the leptonic and the fake background of 100% and 20% respectively are  
2022 imposed. Uncertainties arising from limited statistical precision of the samples used for  
2023 the background estimation are propagated consistently into formula III.7.1. Similar to the  
2024 full optimisation, it can be seen that for low masses and low lifetimes, the highest search

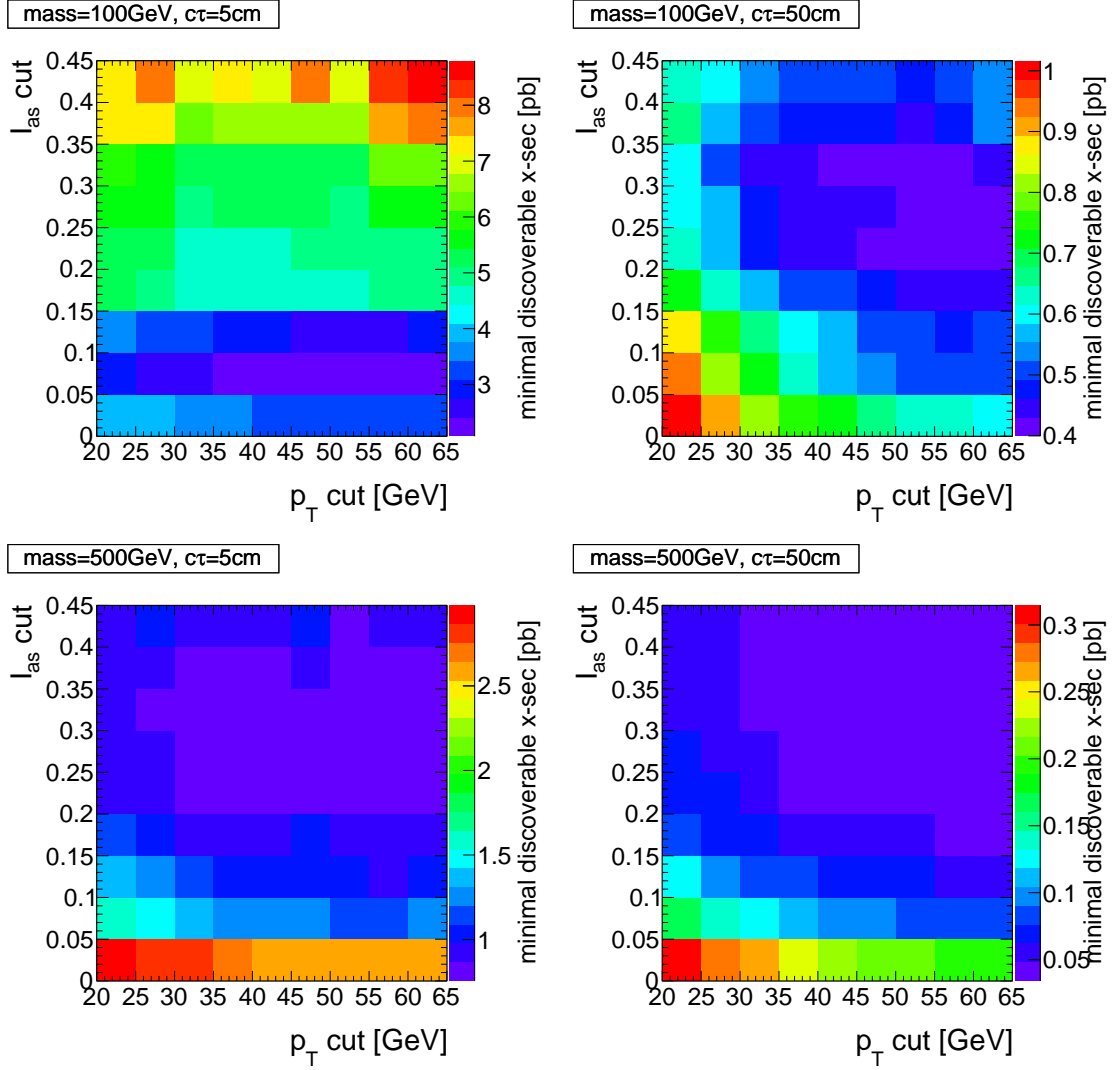


Figure III.7.1: Minimum possible cross section that can be discovered with  $5\sigma$  significance as a function of minimum  $p_T$  and  $I_{as}$  requirements for four different signal models. The systematic uncertainties are taken to be 20% and 100% for the fake and the leptonic background respectively. The uncertainty on the background arising from the limited size of the used samples are propagated consistently to the search optimisation. In Table ?? of Appendix ??, the corresponding histograms of the background yield, the background uncertainty and the signal yield for the four signal models can be found.



sensitivity is achieved by imposing rather soft selection cuts on  $I_{\text{as}}$  and  $p_{\text{T}}$ . Optimising for higher lifetime pushes the optimal selection in  $p_{\text{T}}$  and  $I_{\text{as}}$  to larger values, where signal models with higher masses prefer even tighter  $I_{\text{as}}$  selection cuts than the corresponding lower mass signal model. It can also be seen, that for low lifetimes, the  $p_{\text{T}}$  dependence of the search sensitivity is less pronounced than for long lifetimes.

Based on the optimisation, four different exclusive signal regions are defined in order to achieve an optimal coverage over a wide mass space and a high sensitivity for different lifetimes:

- 1.)  $30 \text{ GeV} < p_{\text{T}} < 50 \text{ GeV}$  and  $0.05 < I_{\text{as}} < 0.3$
- 2.)  $p_{\text{T}} > 50 \text{ GeV}$  and  $0.05 < I_{\text{as}} < 0.3$
- 3.)  $30 \text{ GeV} < p_{\text{T}} < 50 \text{ GeV}$  and  $I_{\text{as}} > 0.3$
- 4.)  $p_{\text{T}} > 50 \text{ GeV}$  and  $I_{\text{as}} > 0.3$ .

## III.8 Results

After developing the methods of the background estimation for all different background sources and their corresponding systematic uncertainties (all explained in Section III.6), the search is performed in four exclusive signal regions with  $19.7 \text{ fb}^{-1}$  of data collected at a centre-of-mass energy of  $\sqrt{s} = 8 \text{ TeV}$  at the CMS experiment. The predicted numbers of events for the fake and the leptonic background in the four signal regions are listed in Table III.8.1. It can be seen, that fake tracks are by far the dominant background to this search. The leptonic background contributes only in one signal region to the total background with a share of about 10%.

Finally, the comparison between the predicted number of events and the number of observed events is shown in Fig. III.8.1. The results are compatible with the Standard Model background within  $1\sigma$  uncertainties in all four signal regions. No excess above the SM prediction is observed in either of the four signal regions. Thus, no evidence for physics beyond the Standard Model could be found.

Therefore, in the following section these results will be used to constrain the parameter space of supersymmetric models with almost mass degenerate charginos and neutralinos.

Additionally, the corresponding numbers of predicted and observed events can be found in Table III.8.2.

Table III.8.1: Background prediction in the four exclusive signal regions for the fake and the leptonic background.

Signal region		Fake Bkg	Leptonic Bkg
$p_T$	$I_{as}$		
30-50 GeV	0.05-0.30	$19.11^{+2.61}_{-2.61} \text{ (stat)} \pm 9.35 \text{ (sys)}$	$0.00^{+2.58}_{-0.00} \text{ (stat)} \pm 0.00 \text{ (sys)}$
50- $\infty$ GeV	0.05-0.30	$22.21^{+3.60}_{-3.60} \text{ (stat)} \pm 8.78 \text{ (sys)}$	$2.17^{+2.99}_{-1.34} \text{ (stat)} \pm 1.65 \text{ (sys)}$
30-50 GeV	0.30-1.00	$2.49^{+0.85}_{-0.85} \text{ (stat)} \pm 1.98 \text{ (sys)}$	$0.00^{+0.22}_{-0.00} \text{ (stat)} \pm 0.00 \text{ (sys)}$
50- $\infty$ GeV	0.30-1.00	$2.52^{+1.14}_{-1.14} \text{ (stat)} \pm 1.27 \text{ (sys)}$	$0.04^{+0.30}_{-0.03} \text{ (stat)} \pm 0.03 \text{ (sys)}$

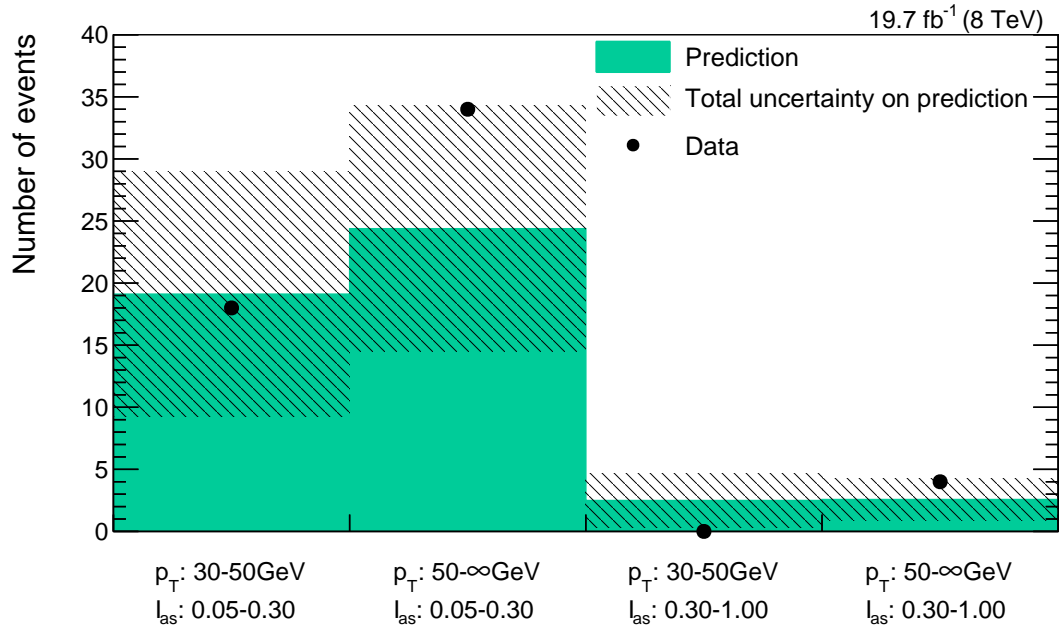


Figure III.8.1: Number of predicted (green area) and observed (black dots) events for the four different signal regions. The hashed area represents the total uncertainty on the background prediction.

Table III.8.2: Number of predicted and observed events for the four different signal regions.

Signal region		Fake Bkg	Leptonic Bkg
$p_T$	$I_{as}$		
30-50 GeV	0.05-0.30	$19.11^{+3.67}_{-2.61} \text{ (stat)} \pm 9.35 \text{ (sys)}$	18
50- $\infty$ GeV	0.05-0.30	$24.38^{+4.68}_{-3.84} \text{ (stat)} \pm 8.93 \text{ (sys)}$	34
30-50 GeV	0.30-1.00	$2.49^{+0.87}_{-0.85} \text{ (stat)} \pm 1.98 \text{ (sys)}$	0
50- $\infty$ GeV	0.30-1.00	$2.57^{+1.18}_{-1.14} \text{ (stat)} \pm 1.27 \text{ (sys)}$	4

## III.9 Interpretation

In order to interpret the result of the search in the context of supersymmetric models with almost mass degenerate charginos and neutralinos, sources of systematic uncertainties on the number of selected signal events must be identified and quantified. The interpretation will then be done with statistical methods that allow for the exclusion of parts of the supersymmetric parameter space on a 95% confidence level. The signal models used for this interpretation are listed in Section III.4.2.

### III.9.1 Systematic uncertainties of simulated signal samples

The systematic uncertainties on the number of signal events in the four signal regions are caused by uncertainties in the generation and simulation of signal events and the integrated luminosity of the considered data.

All systematic uncertainties are estimated for each signal model (cf. Section III.4.2) and each search bin separately. In the following, the sources of systematic uncertainties are discussed and the range of the corresponding uncertainty is given.

## Theoretical cross section

The theoretical cross sections of  $\tilde{\chi}_1^\pm \tilde{\chi}_1^\mp$  and  $\tilde{\chi}_1^\pm \tilde{\chi}_1^0$  production at a centre-of-mass energy of 8 TeV are taken from [77, 78]. The corresponding theoretical uncertainties range between 4.5 – 12.1%.

## Luminosity

The integrated luminosity recorded at CMS during the year 2012 is measured by counting of pixel clusters during the crossing of two bunches (zero-bias event). A detailed explanation of this method and the corresponding total uncertainty of 2.6% can be found in [90].

## Simulation of initial state radiation

Initial state radiation (ISR) affects the transverse momentum distribution of the 2-particle system,  $p_T (p_1^\mu + p_2^\mu)$ , in a 2-body decay. Differences between data and simulation of ISR are taken into account by reweighting the simulated events, such that the simulated transverse momentum distribution matches the measured distribution in data. The weights and associated systematic uncertainties are determined in [91] by comparing simulated and observed  $p_T$  distributions of  $Z$  and  $t\bar{t}$  events. These weights are applied to the simulated  $\tilde{\chi}_1^\pm \tilde{\chi}_1^\mp$  and  $\tilde{\chi}_1^\pm \tilde{\chi}_1^0$  events. To account for the systematic uncertainties on the reweighting procedure, the event weights are varied up and down by up to 25% according to [91] depending on the transverse momentum of the  $\chi_1 \chi_2$  system. The resulting uncertainty on the ISR simulation is between 9.2 – 12.6%.

## Simulation of the trigger efficiency

The HLTMonoCentralPFJet80\_PFMETnoMu105\_NHEF0p95 trigger with the higher MET threshold of 105 GeV active in Run C and Run D during 2012 was not available in the simulated signal samples. It is therefore emulated using HLT trigger information. More details on the emulation of this trigger can be found in Appendix ??.

The trigger uncertainty is assessed by comparing data-simulation differences of the trigger efficiency. This uncertainty has been quantified within [79, 80] by comparing simulated and measured trigger turn-on curves and determining weights for simulated events such that simulated and observed turn-on curves are compatible. These event weights are applied on the simulated signal samples in this analysis and lead to changes in the signal prediction of 1.9 to 4.4%, which are taken as systematic uncertainties.

### Jet energy scale

The transverse momentum of all jets is corrected for non-uniformities in the energy response as a function of the jet  $\eta$  and  $p_T$  and for data-simulation differences [43]. The uncertainty on the jet energy scale (JES) is neatly described and quantified in [43]. It arises from uncertainties on the measured jet response in data including jet fragmentation, jet flavor composition, etc.. The JES correction is applied as a multiplicative factor on each jet's transverse momentum contained in an event. The corresponding systematic uncertainty is assessed by an up- and downward variation of the correction factor within  $1\sigma$ . The resulting uncertainties are of minor importance and range between  $0.4 - 3.1\%$ .

### Jet energy resolution

The jet energy resolution (JER) is smaller in simulation than in measured data (see Part ??). In order to take these differences into account, the simulated jet energy response is smeared to match the measured response. The systematic uncertainty on the smearing factors is estimated in [43, 44]. It covers the uncertainty on JER in data, including the JES uncertainty, uncertainties arising from out-of-cone showering etc. [43, 44]. The resulting uncertainty on the signal efficiency in this study is between  $0.1 - 2.0\%$  and therefore almost negligible.

### Simulation of the parton distribution functions

The parton distribution function (PDF) used for the simulation of proton-proton collisions is provided by the CTEQ group [92] (see Section ?? for more information about PDFs). In [92], a detailed description of the determination of a parton distribution function and its uncertainties is given. Practically, the estimation of the PDF uncertainty is done by the application of 44 different sets of event weights which take into account 22 different sources of uncertainties [93, 94] (up and down variations lead to a factor of 2). The sources correspond inter alia to uncertainties in the single distributions of gluons, up/down-quarks, etc, with the gluon distribution being by far the largest source of uncertainty. The resulting uncertainties on the signal efficiency for this search are between  $2.6 - 6.8\%$ .

### Pileup reweighting

The distribution of the number of primary vertices in simulation is reweighted to match the measured distribution in data. The distribution of the number of primary vertices in data is estimated by the luminosity of each bunch-crossing times the proton-proton inelastic cross section which is  $69.4\text{ mb}$  [95]. The uncertainty on the number of interactions thus consists of the uncertainty on the luminosity and the uncertainty on the cross section. To

cover both sources, a variation of the inelastic cross section by plus/minus 5% is done according to the recommendation by [96].

For most of the signal models and signal regions, the signal efficiency is only affected by less than 1% by the pileup reweighting uncertainty. If the statistical precision of the signal prediction in a specific search bin is low, the uncertainty can become significantly larger. However, the search sensitivity is always driven by search bins with high signal content so that large values of this uncertainty have no effect on the overall search sensitivity.

### Simulation of the calorimeter isolation

The uncertainty on the simulation of the calorimeter isolation  $E_{\text{calo}}^{\Delta R < 0.5}$  is estimated by comparing simulated and measured selection efficiencies of  $E_{\text{calo}}^{\Delta R < 0.5} < 5 \text{ GeV}$  in the fake enriched control sample  $\text{CR}_{I_{\text{as}}}^{\text{fake}}$ . The fake enriched control region is well suited for this estimation, because fake tracks are not correlated to the energy deposits in the calorimeters. The selection efficiency in data is higher than in simulation in both  $p_{\text{T}}$  bins of  $30 - 50 \text{ GeV}$  and  $50 - \infty \text{ GeV}$ . This difference between data and simulation is taken as systematic uncertainty, resulting in uncertainties of 12.1% and 3.0%.

### Simulation of missing middle/inner hits

The uncertainty on the simulation of the number of missing inner and middle hits is assessed by comparing the probability in simulation and data of passing the selection requirements of  $N_{\text{miss}}^{\text{middle/inner}} = 0$  of a candidate track in the muon-veto inverted control region. This control region is particularly suitable because muons are not expected to have intrinsic sources of missing hits, as e.g. pions or electrons have. Pions can interact nuclearly with the tracker material and electrons can have sizable radiative losses, such that both can change direction or don't deposit energy in a tracker layer. For muons, on the other hand, sources of missing inner and middle hits are mainly algorithmic [79, 80], making them very similar to the algorithmic sources of missing inner/middle hits for chargino tracks.

The uncertainty is estimated as the observed difference of the cut selection efficiency of  $N_{\text{miss}}^{\text{middle/inner}} = 0$  in data and simulation. The selection efficiency is always higher in simulation, resulting in systematic uncertainties of around 3.5% for the simulation of  $N_{\text{miss}}^{\text{inner}} = 0$  and around 2.2% for  $N_{\text{miss}}^{\text{middle}} = 0$ . The uncertainties are of very similar size in the signal regions with different  $p_{\text{T}}$ . No  $I_{\text{as}}$  dependence is considered.

### Simulation of $I_{\text{as}}$

An uncertainty on the simulation of  $I_{\text{as}}$  needs to be estimated in order to account for possible data-simulation differences for highly ionising particles. The estimation of the

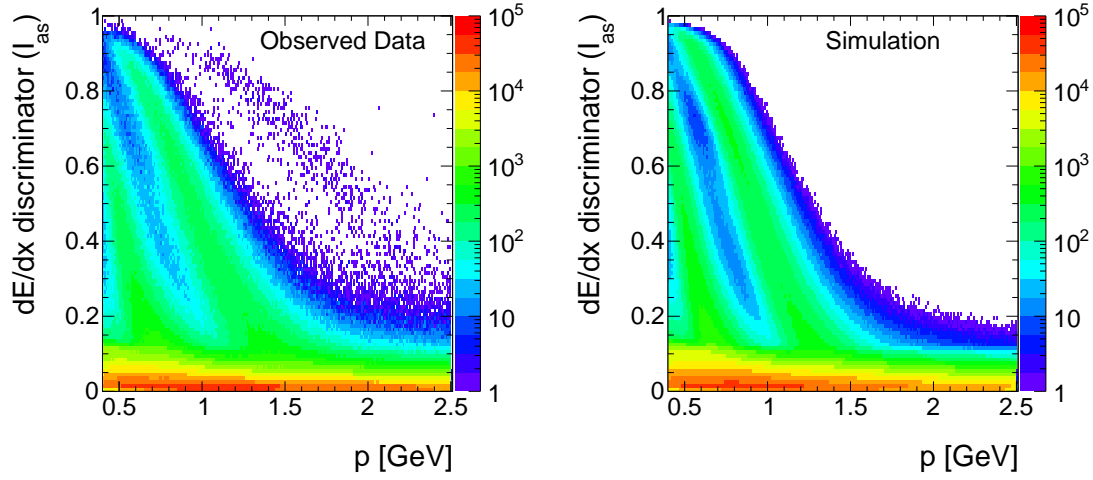


Figure III.9.1:  $I_{\text{as}}$  versus momentum for good quality tracks with at least eight hits in observed data (left) and simulation (right).

$I_{\text{as}}$  uncertainty is done following the methodology in [56, 97]. The  $I_{\text{as}}$  uncertainty can be assessed by comparing data and simulation differences of slow protons. Slow protons are highly ionising and can thus be used to determine the uncertainty in the high  $I_{\text{as}}$  region.

In order to select slow protons, high quality tracks with a momentum smaller than 2.5 GeV are selected. The  $I_{\text{as}}$  versus momentum distribution for the selected tracks is shown in Fig. III.9.1. The kaon and proton line are visible in both datasets. The deuteron line is only visible in data, as deuteron's are not simulated. Two different slices in the momentum are extracted where the proton line is contained:  $p$  between 0.80 – 0.85 GeV and 0.95 – 1.00 GeV. A Gaussian function is fitted to the proton peak and the maximum difference of the mean of the fitted Gaussian between simulation and observed data is taken as systematic uncertainty. The  $I_{\text{as}}$  distribution for the two momentum ranges with the Gaussian fit is depicted in Fig. III.9.2. The systematic uncertainty is estimated to a value of 6%.

### Simulation of the track reconstruction efficiency

One final source of uncertainty is the simulation of the track reconstruction efficiency. Possible differences of the reconstruction efficiency in simulation and data can lead to a different signal acceptance. Differences in the track reconstruction efficiency are especially expected for short tracks. Therefore, a worst case estimation is done, comparing the track reconstruction efficiency in data and simulation for tracks with only three hits.

In simulation and observed data, well reconstructed muon tracks are selected and all hits after the third hit are removed. Afterwards the full track reconstruction is performed

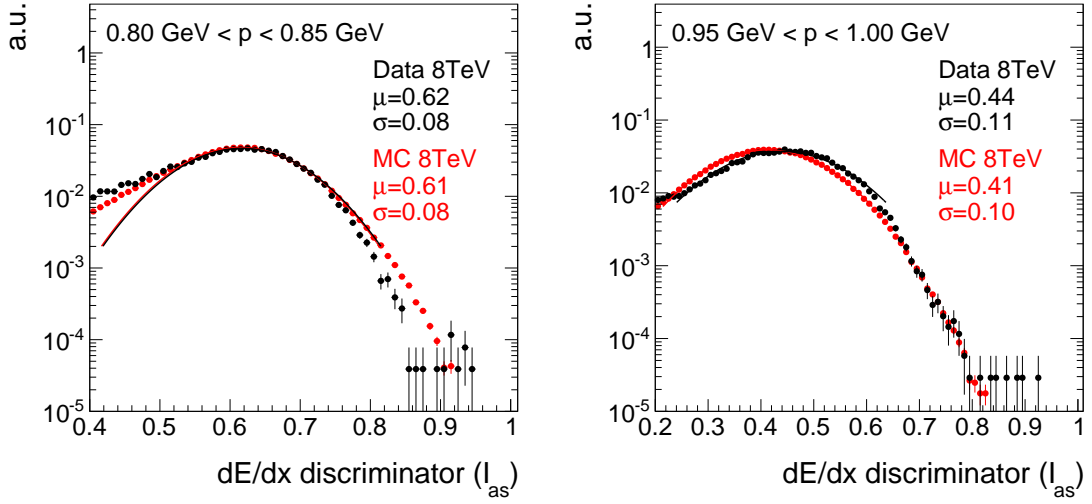


Figure III.9.2:  $I_{\text{as}}$  distribution for slow protons in simulation and observed data for a momentum range of 0.80–0.85 GeV (left) and 0.95–1.00 GeV (left). For the momentum range of 0.80 – 0.85 GeV, the proton line is contained between  $I_{\text{as}}$  values of 0.4 – 0.8, whereas for the momentum range of 0.95 – 1.00 GeV, the proton line  $I_{\text{as}}$  lies between 0.2 – 0.6.

again. The relative difference of this track reconstruction efficiency in data and simulation is taken as systematic uncertainty. The track reconstruction efficiency is higher in simulation than in data and results in uncertainties between 4.6 – 6.0%.

### Summary of systematic uncertainties on the simulated signal samples

All systematic uncertainties are estimated for all simulated signal samples and in each of the four signal regions. An overview of the range of the uncertainties is given in Table III.9.1.

In order to avoid an overestimation of the systematic uncertainties due to limited sizes of the samples (especially for low lifetimes like 1 cm), the corresponding signal sample with longer lifetime (100 cm) is used instead for determining the systematic uncertainty. This is possible for uncertainty sources, where the size is not affected by the lifetime of the chargino, including ISR, trigger efficiency, JES, JER, and PDF uncertainties.

It can be seen, that major uncertainties are the simulation of the initial state radiation, of the calorimeter isolation, and of  $I_{\text{as}}$ . The high maximum value of the pileup uncertainty is caused by limited statistical precision.

The systematic uncertainties on the simulated signal samples are considered as fully correlated among the four signal regions.



Table III.9.1: Ranges of systematic uncertainties on the simulated signal samples. Min and Max correspond to variations between different signal samples and search bins.

Uncertainty	Min [%]	Max [%]
Theoretical x-section	4.5	12.1
Luminosity	2.6	2.6
Simulation of ISR	9.2	12.6
Simulation of trigger efficiency	1.9	4.4
JES	0.4	3.1
JER	0.1	2.0
Simulation of PDF	2.6	6.8
Pileup reweighting	0.0	16.0
Simulation of calorimeter isolation	3.0	12.1
Simulation of missing middle hits	2.2	2.2
Simulation of missing inner hits	3.3	3.7
Simulation of $I_{\text{as}}$	6.0	6.0
Simulation of track reconstruction efficiency	4.6	6.0

### III.9.2 Statistical Methods/ Limit setting

This section is a small interlude to briefly introduce the methods and techniques that are used to exclude theoretical models with the results of this search. For a detailed and pedagogical introduction to the methods, the reader is referred to [98].

In this analysis, the exclusion of the underlying theoretical model is achieved with the  $\text{CL}_s$  method [99–101]. A model is considered as excluded at a 95% confidence level if  $\text{CL}_s$  is smaller than 5%. The  $\text{CL}_s$  method was developed for the Higgs searches at LEP in order not to overestimate the exclusion power of a result if an under-fluctuation of the background expectation occurs.  $\text{CL}_s$  is defined as the confidence level of the background plus signal hypothesis divided by the confidence level of the background only hypothesis

$$\text{CL}_s = \frac{\text{CL}_{s+b}}{\text{CL}_b}.$$

The confidence level CL is defined as the probability of obtaining less than or equal the number of observed events  $P(n \leq n_{\text{obs}})$  for a given background (or background+signal) hypothesis. For Poissonian statistics it leads to the following expressions for  $\text{CL}_{s+b}$  and  $\text{CL}_b$  for one signal region

$$\begin{aligned}\text{CL}_{s+b} &= \text{Poisson}(n \leq n_{\text{obs}} | \lambda = b + \mu \cdot s), \\ \text{CL}_b &= \text{Poisson}(n \leq n_{\text{obs}} | \lambda = b),\end{aligned}\tag{III.9.1}$$

where  $\lambda$  is the mean of the Poisson distribution and the signal strength  $\mu$  is the measure for the size of the signal cross section.

Systematic uncertainties are included by varying the background expectation  $b$  and the signal expectation  $\mu \cdot s$  according to a predefined probability density function (pdf). For one Gaussian distributed source of systematic uncertainty on the background, this leads to the following expressions for  $\text{CL}_{s+b}$  and  $\text{CL}_b$

$$\begin{aligned}\text{CL}_{s+b} &= \text{Poisson}(n \leq n_{\text{obs}} | \lambda = b \cdot (1 + \delta_b) + \mu \cdot s) \text{Gauss}(\delta_b | \text{mean} = 0, \sigma = \sigma_b), \\ \text{CL}_b &= \text{Poisson}(n \leq n_{\text{obs}} | \lambda = b \cdot (1 + \delta_b)) \text{Gauss}(\delta_b | \text{mean} = 0, \sigma = \sigma_b),\end{aligned}\tag{III.9.2}$$

These expressions can be generalised for more than one signal region and more than one systematic uncertainty [98]. In case of multiple signal regions, the distribution of the systematic uncertainties becomes a multi-dimensional probability density function that takes the covariance matrix of the systematic uncertainties in different signal regions into account.

In this analysis, the procedure for limit setting follows [102]. Instead of the number of observed events, the profile likelihood ratio

$$q(n, \mu) = -2 \ln \frac{\mathcal{L}(n | \mu, \hat{\delta}_b, \hat{\delta}_s)}{\mathcal{L}(n | \hat{\mu}, \hat{\delta}_b, \hat{\delta}_s)},\tag{III.9.3}$$

is used as the test statistics for determining  $\text{CL}_{s+b}$  and  $\text{CL}_b$  ( $\mu = 0$ ).  $\mathcal{L}$  refers to the likelihood function

$$\mathcal{L} = \text{Poisson}(n | \lambda = b \cdot (1 + \delta_b) + \mu \cdot s(1 + \delta_s)) p(\delta_b) p(\delta_s).\tag{III.9.4}$$

that already appeared in Eq. (III.9.1). The parameters  $\hat{\mu}$ ,  $\hat{\delta}_b$  and  $\hat{\delta}_s$  are fixed to the values that maximise the likelihood with respect to the observed data. Determining  $\text{CL}_{s+b}$  and  $\text{CL}_b$  requires knowing the probability distributions of  $q$  for the signal+background hypothesis (depending on  $\mu$ ) and the background-only hypothesis ( $\mu = 0$ ). These distributions are determined by toy pseudo data with fixed values for  $\delta_s$  and  $\delta_b$ . Finally, the signal strength  $\mu$  is adjusted until  $\text{CL}_s$ -calculated based on  $q$  - equals 0.05%. Signal models are

considered as excluded on a 95% confidence level, if the signal strength is larger than the one found by the limit setting procedure.

In this search, the systematic uncertainties on the background and the signal yields as well as the statistical uncertainty on the fake background are modelled with log-normal distributions, whereas the statistical uncertainties on the leptonic background are modelled using gamma distributions. A log-normal distribution is used instead of a normal distribution to ensure that the prediction cannot become negative. The gamma distribution is well suited for statistical uncertainties arising from very limited statistical precision in control regions or in simulated samples that are used for the background estimation [103].

Correlations between systematic uncertainties on the background expectation in different search bins are assumed as shown in Table III.9.2. The systematic uncertainties on the expected signal yields are considered fully correlated across search bins.

The exclusion limits are derived according to the above presented methodology using the *Combine* framework [103] which was developed for the Higgs searches at CMS.

Table III.9.2: Correlation of systematic and statistical uncertainties between the four different signal regions. Statistical uncertainties include uncertainties arising from the limited size of control regions and the simulated samples.

	Fakes	Taus	Electrons	Muons
Statistical uncertainty	0% correlated	100% for bins with same $I_{\text{as}}$	0% correlated	100% for bins with same $I_{\text{as}}$
Leptonic scale factor uncertainty	-	100% for bins with same $I_{\text{as}}$	100% for bins with same $I_{\text{as}}$	100% for bins with same $I_{\text{as}}$
Fake rate uncertainty	100% for bins with same $I_{\text{as}}$	-	-	-
$I_{\text{as}}$ uncertainty	0% correlated	100% for bins with same $p_{\text{T}}$	100% for bins with same $p_{\text{T}}$	100% for bins with same $p_{\text{T}}$

### III.9.3 Exclusion limits

The presented search for highly ionising, short tracks is interpreted in the context of SUSY models with almost mass degenerate wino-like charginos and neutralinos. As explained in the previous section, the exclusion is done with the help of the  $\text{CL}_s$  method. Two direct production channels are taken into account: chargino pair production and chargino neutralino production. The corresponding cross sections can be found in Table III.4.2.

In total, 37 different lifetimes from  $c\tau = 1 - 10000 \text{ cm}$  for each mass point (100 – 600 GeV in steps of 100 GeV) are considered. Four exemplary exclusion limits are shown in Fig. III.9.3, the full set of exclusion limits can be found in Appendix ??.

The upper 95% confidence level (CL) limit on the signal cross section is strongest for lifetimes between 10–100 cm. For lower lifetimes a sizable fraction of the charginos already decay before reaching the tracker. For longer lifetimes, the cross section upper limit gets weaker again because the charginos start to be reconstructed as muons and do not pass the muon veto. Also, the  $E_{\text{calo}}^{\Delta R < 0.5}$  requirement rejects these charginos with higher efficiency.

Due to the falling spectrum of the chargino production cross section, charginos with lower masses are more effectively excluded than charginos with higher masses. A 2-dimensional exclusion limit in the chargino lifetime-mass parameter space is shown in Fig. III.9.4.

Charginos with masses of 100 GeV can be excluded down to a lifetime of  $c\tau = 2 \text{ cm}$ . Charginos with a higher mass of 500 GeV are excluded for lifetimes between  $c\tau = 70 - 500 \text{ cm}$ .

Since the lifetime of a wino-like chargino is determined by the mass splitting between  $m_{\tilde{\chi}_1^\pm}$  and  $m_{\tilde{\chi}_1^0}$ , it is possible to express the lifetime of the chargino as a mass gap  $\Delta m_{\tilde{\chi}_1^\pm \tilde{\chi}_1^0}$  between the chargino and the lightest neutralino. The correspondence between lifetime and mass gap is taken from [104], where the decay width of  $\tilde{\chi}_1^\pm \rightarrow \tilde{\chi}_1^0 \pi^\pm$  is expressed in terms of chargino, neutralino, and pion mass. Thus, the mass gaps that are considered are bounded by the pion mass of  $\sim 140 \text{ MeV}$ . The corresponding 2d exclusion limit can be found in Fig. III.9.5. It can be seen that this search is sensitive to mass splittings between  $\sim 140 \text{ MeV} - 210 \text{ MeV}$ .

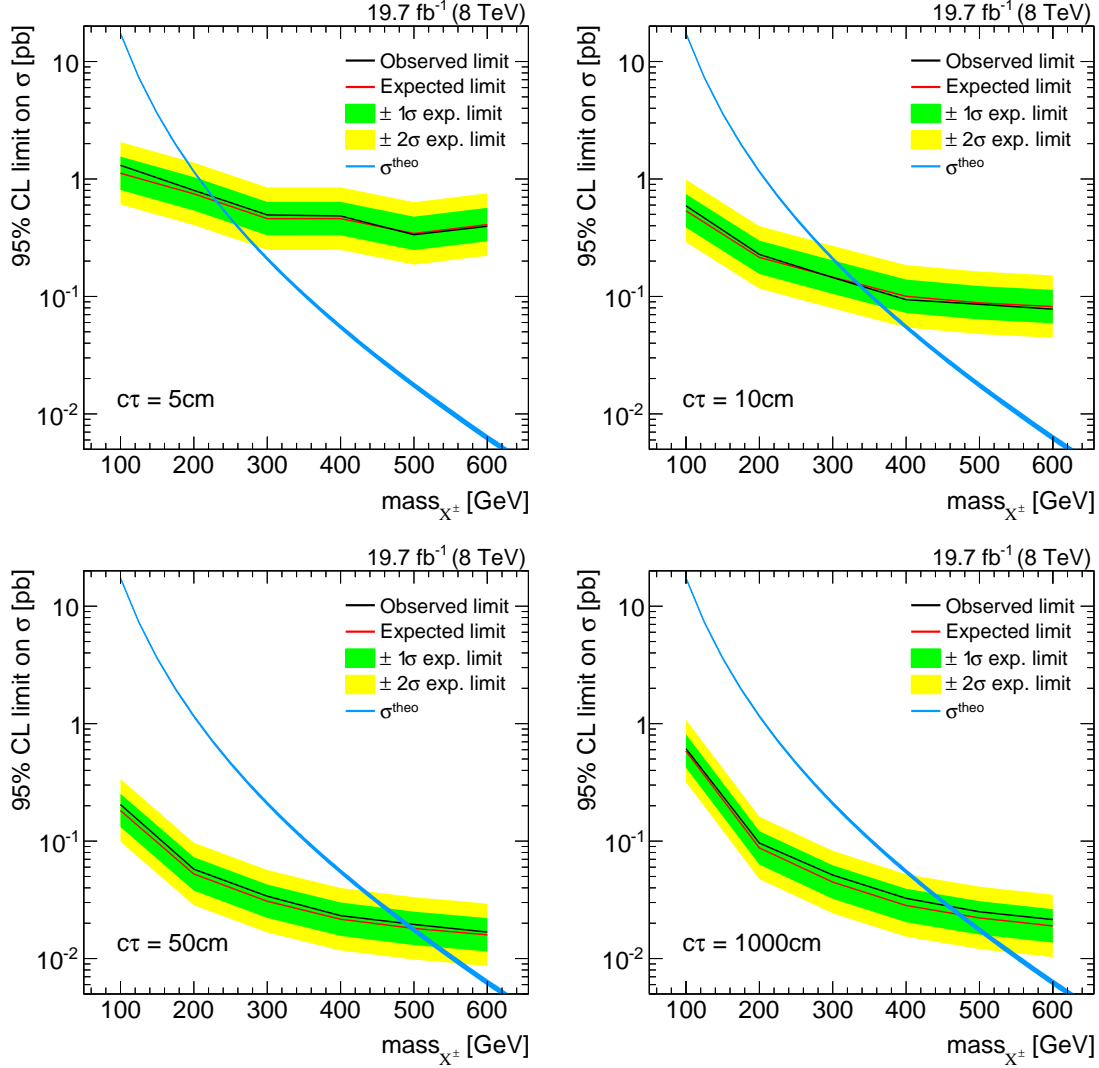


Figure III.9.3: Four different  $CL_s$  exclusion limits for charginos with mean lifetimes of 5 cm (top left), 10 cm (top right), 50 cm (bottom left), 1000 cm (bottom right). The red line depicts the expected 95% confidence level (CL) upper cross-section limit with the  $1\sigma$  (green band) and  $2\sigma$  (yellow band) intervals. The black line is the observed limit. The signal cross section is depicted as a blue line. SUSY models can be excluded at 95% CL if the signal cross section is at least as large as the 95% CL observed upper limit on the cross section.

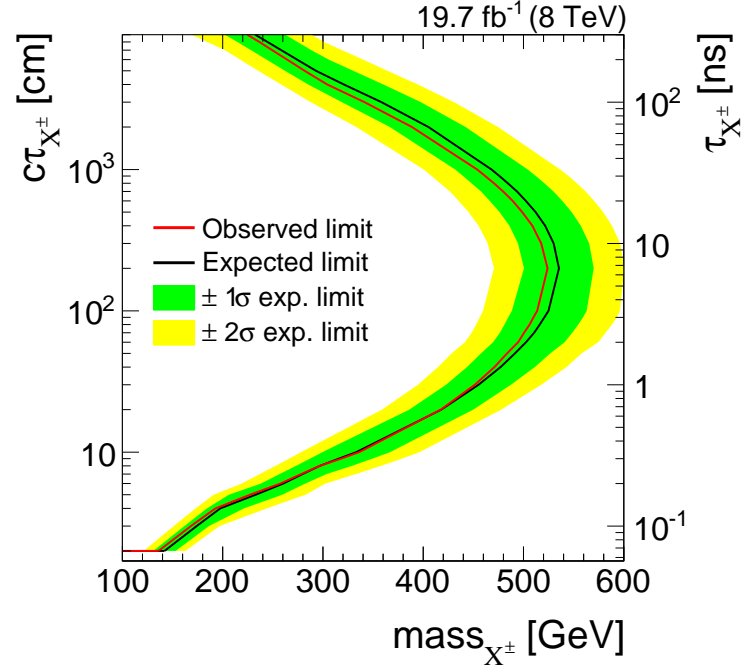


Figure III.9.4: Excluded regions in the mass versus lifetime space. All excluded models are located left of the contour line. The red line depicts the expected 95% CL upper cross-section limit with the 1- $\sigma$  (green band) and 2- $\sigma$  (yellow band) intervals. The black line is the observed limit.

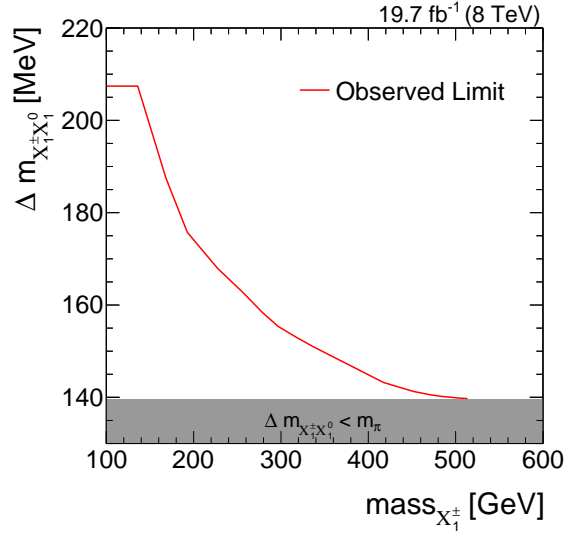


Figure III.9.5: Excluded parameter region at 95% CL for wino-like charginos and neutralinos depending on the chargino mass and the mass splitting between  $\tilde{\chi}_1^\pm$  and  $\tilde{\chi}_1^0$ ,  $\Delta m_{\tilde{\chi}_1^\pm \tilde{\chi}_1^0}$ . All SUSY models between the red line and the grey area are excluded.

### III.9.4 Comparison to the search for disappearing tracks

The presented exclusion limits confirm the exclusion from the search for disappearing tracks [55] with slight improvements in the low lifetime region. The comparison of the two searches is shown in Fig. III.9.6.

For charginos with a lifetime of  $\tau = 0.07 \text{ ns}$  ( $c\tau = 2.1 \text{ cm}$ ), the observed limit of this search improves the limits derived in [55] by  $\sim 35 \text{ GeV}$  in chargino mass, for a lifetime of  $\tau = 0.4 \text{ ns}$  ( $c\tau = 12.0 \text{ cm}$ ) by  $\sim 25 \text{ GeV}$ . For SUSY models with long chargino lifetimes the here presented search shows a higher exclusion power. The weaker exclusion for long lifetimes in [55] is caused by the additional selection cut on the number of missing outer hits,  $N_{\text{lost}}^{\text{outer}} \geq 3$ .

The confirmation of the excluded parameter space in [55] is especially interesting since the signal regions of the two searches are little correlated. The correlation between simulated signal events, that pass the selection from [55],  $N_A$ , and the selection used in this analysis,  $N_B$ , can be estimated by the event overlap  $\rho_{\text{corr}}$

$$\rho_{\text{corr}} = \frac{N_{A \cap B}}{N_{A \cup B}} = \frac{N_{A \cap B}}{N_A + N_B - N_{A \cap B}}.$$

In order to avoid an over- or underestimation of the event overlap, only the most sensitive signal region from this search is included in  $N_B$ . The degree of correlation is depicted in Fig. III.9.7 which shows the event overlap for signal models with chargino masses between

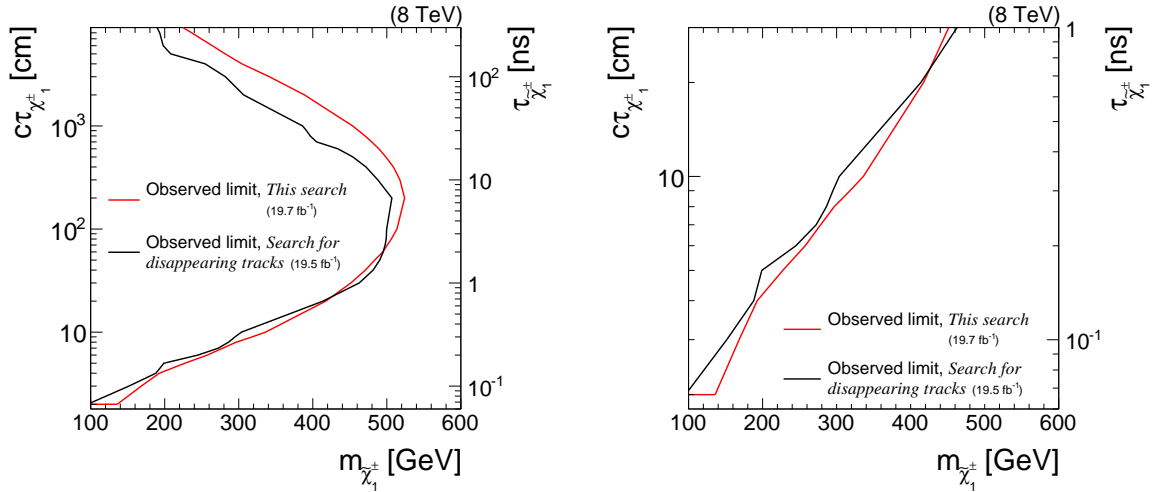


Figure III.9.6: Comparison of the excluded regions in the mass versus lifetime space in this analysis (red line) and the search for disappearing tracks [55] (black line). The right figure is a zoom on the low lifetime region. All SUSY models left of the lines are excluded.

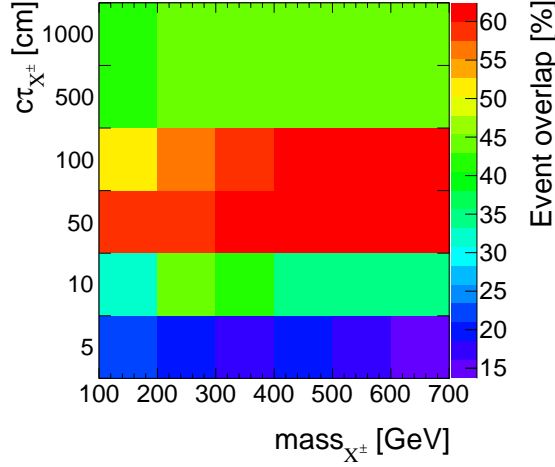


Figure III.9.7: The event overlap between simulated signal events, that pass the selection from [55] and the selection used in this analysis for different signal models. The correlation is determined using only the signal region with the highest sensitivity of this analysis.

2306 100 – 600 GeV and lifetimes between 5 cm – 1000 cm.

2307 It can be seen that the event overlap for intermediate lifetimes of around 100 cm is  
 2308 around 60% and decreases for shorter lifetimes to small overlaps of around 15 – 20%.  
 2309 Additionally, the two events that were observed in data by [55] in their signal region  
 2310 are not contained in any of the signal regions in the here presented analysis. Thus, this  
 2311 analysis constitutes an independent confirmation of the exclusion limits derived in [55].

## 2312 III.10 Conclusion and outlook

2313 The here presented search for highly ionising, short tracks is motivated by supersym-  
 2314 metric models with almost mass-degenerate wino-like charginos  $\tilde{\chi}_1^\pm$  and neutralinos  $\tilde{\chi}_1^0$ .  
 2315 Such scenarios can have interesting astrophysical implications [51] and occur naturally in  
 2316 Supersymmetry, if the wino mass parameter is smaller than the bino and higgsino mass  
 2317 parameters.

2318

2319 The presented analysis targets SUSY models with intermediate chargino lifetimes. This  
 2320 is achieved by searching for isolated, high  $p_T$  tracks that are highly ionising. No require-



ment on the number of tracker hits is enforced, thus, possibly very short tracks from early decaying charginos are included in this analysis.

It, thus, extends the search for disappearing tracks [55] by the inclusion of the variable  $dE/dx$  and the loosening of the requirement on the number of hits in the tracker ( $N_{\text{hits}} \geq 3$ ) that leads to a strong suppression of signal events for low chargino lifetimes (cf. Fig. III.2.7). It is thereby the first analysis at CMS that studies disappearing tracks with down to three hits.

In order to increase the search sensitivity with respect to shorter lifetimes, energy information from the pixel silicon tracker is taken into account. For this purpose, a dedicated pixel energy calibration was carried out within this thesis to ensure stable energy measurements over time and across pixel modules. This is thus the first time that an analysis at CMS makes use of energy information from the pixel tracker. By adding pixel energy information, the discrimination power of  $dE/dx$  is substantially increased (cf. Fig. III.3.10).

The Standard Model background is mainly estimated with data-based techniques. The main background to this search is arising from fake tracks, i. e. tracks that are reconstructed out of the tracker hits of more than one particle. Fake tracks are typically short and can have large values of  $I_{\text{as}}$ , thus showing a very signal-like signature in the detector. The background contribution by leptons that are passing the lepton veto is very small and in most of the signal regions almost negligible.

In the current analysis, the background is estimated at 19 – 24 events in the low  $I_{\text{as}}$  signal regions and 2.5 – 2.6 events in the high  $I_{\text{as}}$  regions. This background estimate is confronted with collision data recorded during the year 2012 at the CMS experiment at a centre-of-mass energy of 8 TeV. No evidence for physics beyond the Standard Model is found. Thus, the absence of any deviation from the Standard Model prediction is used to constrain the supersymmetric parameter space. Wino-like charginos are excluded down to lifetimes of  $c\tau = 2$  cm for  $m_{\tilde{\chi}_1^\pm} = 100$  GeV. For high mass scenarios of  $m_{\tilde{\chi}_1^\pm} = 500$  GeV, the excluded lifetime ranges between  $c\tau = 70 - 500$  cm. This confirms the parameter exclusion limits of the search for disappearing tracks [55]. Interestingly, the signal regions of the here presented search and the search from [55] show little overlap. Therefore, this analysis yields a complementary result with respect to the search for disappearing tracks [55]. In summary, the exclusion of SUSY models with respect to earlier searches could be independently confirmed and improvements in the exclusions of around 10 – 40 GeV in chargino mass in the low lifetime region are achieved.

While this analysis is able to exclude many SUSY models with intermediate lifetime charginos, there are several promising avenues for even enhancing the search sensitivity.

First, since the sensitivity of the current analysis is mainly limited by large systematic

uncertainties originating from low statistical precision in the simulated datasets, simulating more events could significantly improve the search sensitivity. This strategy is however technically challenging, since storage capacity limits were already reached within the current analysis. Still, reducing this systematic uncertainty will be one of the main tasks for future research.

Second, even though this search already features low background, a further background suppression is desirable. However, the impact on the search sensitivity will be limited because of the high relative Poisson error on low background predictions. For instance, a reduction of the number of background events by 50% from 2 to 1 reduces the signal yield required for a  $5\sigma$ -discovery by around 8%, whereas a 50% reduction of expected background events from 200 to 100 reduces the required signal yield by 26%.

Thus, in order to improve the here presented analysis, the focus should be on the other determinant of search sensitivity: the signal acceptance. First and foremost, it is important to lower the signal losses due to trigger requirements. For this purpose, a dedicated track trigger is indispensable and it is very promising that such a trigger is included in Run II trigger menus.

Furthermore, an implementation of a dedicated track reconstruction algorithm optimised for short tracks could increase the reconstruction efficiency of possible chargino tracks, which is currently  $\sim 20\text{--}40\%$  for chargino tracks with 3 – 4 hits. Additionally, a track reconstruction optimised for the reconstruction of soft particles that are not produced in the primary vertex could allow for a reconstruction of the Standard Model decay products of charginos, thereby enabling a better discrimination against Standard Model background.

In summary, the here presented analysis explored a new path for searching for long-lived charginos decaying early inside the detector. It is the first analysis that incorporates reconstructed tracks down to three hits. Furthermore, for the first time, ionisation losses are measured taking energy information from the pixel silicon tracker into account.

As argued, further improvements can allow for accessing new, unexplored SUSY models with long-lived charginos. Additionally, a search in collisions at a centre-of-mass energy of 13 TeV with increased cross sections makes the exploration of SUSY models with higher chargino masses possible. Since  $dE/dx$  is much more discriminating for high masses, the inclusion of  $dE/dx$  in this analysis will become even more powerful.

## Bibliography

- [1] M. Baak, M. Goebel, J. Haller et al., “The Electroweak Fit of the Standard Model after the Discovery of a New Boson at the LHC”, *Eur. Phys. J.* **C72** (2012) 2205, [arXiv:1209.2716](#). doi:10.1140/epjc/s10052-012-2205-9.
- [2] CMS Collaboration, “Observation of a new boson at a mass of 125 GeV with the CMS experiment at the LHC”, *Phys. Lett.* **B716** (2012) 30–61, [arXiv:1207.7235](#). doi:10.1016/j.physletb.2012.08.021.
- [3] ATLAS Collaboration, “Observation of a new particle in the search for the Standard Model Higgs boson with the ATLAS detector at the LHC”, *Phys. Lett.* **B716** (2012) 1–29, [arXiv:1207.7214](#). doi:10.1016/j.physletb.2012.08.020.
- [4] Peskin, Michael E. and Schroeder, Daniel V., “An Introduction To Quantum Field Theory”. Westview Press, 1995.
- [5] Ryder, L. H., “QUANTUM FIELD THEORY”. Cambridge University Press, 1996.
- [6] D. Griffiths, “Introduction to Elementary Particles”. Wiley, 2008.
- [7] P. W. Higgs, “Broken symmetries, massless particles and gauge fields”, *Phys. Lett.* **12** (1964) 132–133. doi:10.1016/0031-9163(64)91136-9.
- [8] P. W. Higgs, “Broken Symmetries and the Masses of Gauge Bosons”, *Phys. Rev. Lett.* **13** (1964) 508–509. doi:10.1103/PhysRevLett.13.508.
- [9] F. Englert and R. Brout, “Broken Symmetry and the Mass of Gauge Vector Mesons”, *Phys. Rev. Lett.* **13** (1964) 321–323. doi:10.1103/PhysRevLett.13.321.
- [10] G. S. Guralnik, C. R. Hagen, and T. W. B. Kibble, “Global Conservation Laws and Massless Particles”, *Phys. Rev. Lett.* **13** (1964) 585–587. doi:10.1103/PhysRevLett.13.585.
- [11] P. W. Higgs, “Spontaneous Symmetry Breakdown without Massless Bosons”, *Phys. Rev.* **145** (1966) 1156–1163. doi:10.1103/PhysRev.145.1156.
- [12] T. W. B. Kibble, “Symmetry breaking in nonAbelian gauge theories”, *Phys. Rev.* **155** (1967) 1554–1561. doi:10.1103/PhysRev.155.1554.

- [13] S. L. Glashow, “Partial Symmetries of Weak Interactions”, *Nucl. Phys.* **22** (1961) 579–588. doi:10.1016/0029-5582(61)90469-2.
- [14] S. Weinberg, “A Model of Leptons”, *Phys. Rev. Lett.* **19** (1967) 1264–1266. doi:10.1103/PhysRevLett.19.1264.
- [15] A. Salam, “Weak and Electromagnetic Interactions”, *Conf. Proc.* **C680519** (1968) 367–377.
- [16] UA1 Collaboration, “Experimental Observation of Isolated Large Transverse Energy Electrons with Associated Missing Energy at  $s^{1/2} = 540\text{-GeV}$ ”, *Phys. Lett.* **B122** (1983) 103–116. [611(1983)]. doi:10.1016/0370-2693(83)91177-2.
- [17] UA1 Collaboration, “Experimental Observation of Lepton Pairs of Invariant Mass Around  $95\text{-GeV}/c^2$  at the CERN SPS Collider”, *Phys. Lett.* **B126** (1983) 398–410. doi:10.1016/0370-2693(83)90188-0.
- [18] Particle Data Group Collaboration, “Review of Particle Physics”, *Chin. Phys.* **C38** (2014) 090001. doi:10.1088/1674-1137/38/9/090001.
- [19] ATLAS, CMS Collaboration, “Combined Measurement of the Higgs Boson Mass in  $pp$  Collisions at  $\sqrt{s} = 7$  and  $8\text{ TeV}$  with the ATLAS and CMS Experiments”, *Phys. Rev. Lett.* **114** (2015) 191803, arXiv:1503.07589. doi:10.1103/PhysRevLett.114.191803.
- [20] G. 't Hooft, C. Itzykson, A. Jaffe et al., “Recent Developments in Gauge Theories. Proceedings, Nato Advanced Study Institute, Cargese, France, August 26 - September 8, 1979”, *NATO Sci. Ser. B* **59** (1980) pp.1–438.
- [21] J. E. Gunn and B. A. Peterson, “On the Density of Neutral Hydrogen in Intergalactic Space”, *Astrophys. J.* **142** (1965) 1633. doi:10.1086/148444.
- [22] Planck Collaboration, “Planck 2015 results. XIII. Cosmological parameters”, arXiv:1502.01589.
- [23] Yu. A. Golfand and E. P. Likhtman, “Extension of the Algebra of Poincare Group Generators and Violation of p Invariance”, *JETP Lett.* **13** (1971) 323–326. [Pisma Zh. Eksp. Teor. Fiz.13,452(1971)].
- [24] R. Haag, J. T. Lopuszanski, and M. Sohnius, “All Possible Generators of Supersymmetries of the s Matrix”, *Nucl. Phys.* **B88** (1975) 257. doi:10.1016/0550-3213(75)90279-5.

- [25] M. Drees, “An Introduction to Supersymmetry”, in *Current topics in physics. Proceedings, Inauguration Conference of the Asia-Pacific Center for Theoretical Physics (APCTP), Seoul, Korea, June 4-10, 1996. Vol. 1, 2.* 1996.  
arXiv:hep-ph/9611409.
- [26] I. J. R. Aitchison, “Supersymmetry and the MSSM: An Elementary introduction”,  
arXiv:hep-ph/0505105.
- [27] M. Drees, R. Godbole, and P. Roy, “Theory and phenomenology of sparticles: An account of four-dimensional N=1 supersymmetry in high energy physics”. World Scientific, 2004.
- [28] U. Amaldi, W. de Boer, and H. Furstenau, “Comparison of grand unified theories with electroweak and strong coupling constants measured at LEP”, *Phys. Lett. B* **260** (1991) 447–455. doi:10.1016/0370-2693(91)91641-8.
- [29] MSSM Working Group Collaboration, A. Djouadi et al., “The Minimal supersymmetric standard model: Group summary report”, in *GDR (Groupement De Recherche) - Supersymetrie Montpellier, France, April 15-17, 1998.* 1998.  
arXiv:hep-ph/9901246.
- [30] CMS Collaboration, “Measurements of differential dijet cross section in proton-proton collisions at  $\sqrt{s} = 8$  TeV with the CMS detector”, *CMS Physics Analysis Summary CMS-PAS-SMP-14-002* (2014).
- [31] CMS Collaboration, “Measurement of the differential cross section for top quark pair production in pp collisions at  $\sqrt{s} = 8$  TeV”, *Eur. Phys. J. C* **75** (2015), no. 11, 542, arXiv:1505.04480. doi:10.1140/epjc/s10052-015-3709-x.
- [32] CMS Collaboration, “Search for new physics in the multijet and missing transverse momentum final state in proton-proton collisions at  $\sqrt{s} = 8$  TeV”, *JHEP* **06** (2014) 055, arXiv:1402.4770. doi:10.1007/JHEP06(2014)055.
- [33] CMS Collaboration, “Searches for Supersymmetry using the  $M_{T2}$  Variable in Hadronic Events Produced in pp Collisions at 8 TeV”, *JHEP* **05** (2015) 078, arXiv:1502.04358. doi:10.1007/JHEP05(2015)078.
- [34] CMS Collaboration, “Search for supersymmetry in hadronic final states with missing transverse energy using the variables  $\alpha_T$  and b-quark multiplicity in pp collisions at  $\sqrt{s} = 8$  TeV”, *Eur. Phys. J. C* **73** (2013), no. 9, 2568, arXiv:1303.2985. doi:10.1140/epjc/s10052-013-2568-6.

- [35] CMS Collaboration, “Determination of Jet Energy Calibration and Transverse Momentum Resolution in CMS”, *JINST* **6** (2011) P11002, [arXiv:1107.4277](#).  
[doi:10.1088/1748-0221/6/11/P11002](#).
- [36] CMS Collaboration, “Jet Energy Resolution in CMS at  $\sqrt{s}=7$  TeV”, *CMS Physics Analysis Summary CMS-PAS-JME-10-014* (2011).
- [37] CMS Collaboration, “Performance of Photon Reconstruction and Identification with the CMS Detector in Proton-Proton Collisions at  $\sqrt{s} = 8$  TeV”, *JINST* **10** (2015), no. 08, P08010, [arXiv:1502.02702](#).  
[doi:10.1088/1748-0221/10/08/P08010](#).
- [38] CMS Collaboration, “Particle-Flow Event Reconstruction in CMS and Performance for Jets, Taus, and MET”, *CMS Physics Analysis Summary CMS-PAS-PFT-09-001* (2009).
- [39] M. Cacciari, G. P. Salam, and G. Soyez, “The anti- $k_t$  jet clustering algorithm”, *JHEP* **04** (2008) 063, [arXiv:0802.1189](#). [doi:10.1088/1126-6708/2008/04/063](#).
- [40] N. Odell, “PF Jet ID Recommendation”.  
[https://indico.cern.ch/event/89919/contribution/0/attachments/1091238/1556772/PF\\_JET\\_ID\\_Recommendation.pdf](https://indico.cern.ch/event/89919/contribution/0/attachments/1091238/1556772/PF_JET_ID_Recommendation.pdf), April, 2010.
- [41] N. Saoulidou and E. Tziaferi, “Performance of the Particle-Flow jet identification criteria using proton-proton collisions at  $\sqrt{s} = 8$  TeV”, *CMS Analysis Note CMS-AN-14-227* (2014). Internal documentation.
- [42] M. Schröder, “Quality of jet measurements and impact on a search for new physics at CMS”. PhD thesis, Hamburg U., 2012.  
<http://www-library.desy.de/cgi-bin/showprep.pl?thesis12-042>.
- [43] CMS Collaboration, “Jet Energy Scale and Resolution in the CMS Experiment”, *CMS Physics Analysis Summary CMS-PAS-JME-13-004* (2015).
- [44] K. Goebel, “Probing supersymmetry based on precise jet measurements at the CMS experiment”. PhD thesis, U. Hamburg, Dept. Phys., 2015.  
<http://www-library.desy.de/cgi-bin/showprep.pl?thesis15-003>.
- [45] CDF, D0 Collaboration, T. Adams, “SUSY Searches at the Tevatron”, in *Hadron collider physics. Proceedings, 19th Symposium, HCP2008, Galena, USA, May 27-31, 2008*. 2008. [arXiv:0808.0728](#).
- [46] ALEPH, DELPHI, L3 and OPAL Collaborations, “Joint SUSY Working Group”.  
<http://lepsusy.web.cern.ch/lepsusy>. LEPSUSYWG (June 2004).

- [47] ATLAS Collaboration, “Search for squarks and gluinos with the ATLAS detector in final states with jets and missing transverse momentum using  $\sqrt{s} = 8$  TeV proton–proton collision data”, *JHEP* **09** (2014) 176, [arXiv:1405.7875](#).  
[doi:10.1007/JHEP09\(2014\)176](#).
- [48] M. Ibe, S. Matsumoto, S. Shirai et al., “Wino Dark Matter in light of the AMS-02 2015 Data”, *Phys. Rev.* **D91** (2015), no. 11, 111701, [arXiv:1504.05554](#).  
[doi:10.1103/PhysRevD.91.111701](#).
- [49] J. Hisano, S. Matsumoto, M. M. Nojiri et al., “Direct detection of the Wino and Higgsino-like neutralino dark matters at one-loop level”, *Phys. Rev.* **D71** (2005) 015007, [arXiv:hep-ph/0407168](#). [doi:10.1103/PhysRevD.71.015007](#).
- [50] T. Moroi and L. Randall, “Wino cold dark matter from anomaly mediated SUSY breaking”, *Nucl. Phys.* **B570** (2000) 455–472, [arXiv:hep-ph/9906527](#).  
[doi:10.1016/S0550-3213\(99\)00748-8](#).
- [51] T. Moroi, M. Nagai, and M. Takimoto, “Non-Thermal Production of Wino Dark Matter via the Decay of Long-Lived Particles”, *JHEP* **07** (2013) 066, [arXiv:1303.0948](#). [doi:10.1007/JHEP07\(2013\)066](#).
- [52] G. F. Giudice, M. A. Luty, H. Murayama et al., “Gaugino mass without singlets”, *JHEP* **12** (1998) 027, [arXiv:hep-ph/9810442](#).  
[doi:10.1088/1126-6708/1998/12/027](#).
- [53] L. Randall and R. Sundrum, “Out of this world supersymmetry breaking”, *Nucl. Phys.* **B557** (1999) 79–118, [arXiv:hep-th/9810155](#).  
[doi:10.1016/S0550-3213\(99\)00359-4](#).
- [54] A. Anandakrishnan, L. M. Carpenter, and S. Raby, “Degenerate gaugino mass region and mono-boson collider signatures”, *Phys. Rev.* **D90** (2014), no. 5, 055004, [arXiv:1407.1833](#). [doi:10.1103/PhysRevD.90.055004](#).
- [55] CMS Collaboration, “Search for disappearing tracks in proton-proton collisions at  $\sqrt{s} = 8$  TeV”, *JHEP* **01** (2015) 096, [arXiv:1411.6006](#).  
[doi:10.1007/JHEP01\(2015\)096](#).
- [56] CMS Collaboration, “Searches for long-lived charged particles in pp collisions at  $\sqrt{s}=7$  and 8 TeV”, *JHEP* **07** (2013) 122, [arXiv:1305.0491](#).  
[doi:10.1007/JHEP07\(2013\)122](#).
- [57] CMS Collaboration, “Phenomenological MSSM interpretation of the CMS 2011 5fb-1 results”, *CMS Physics Analysis Summary* **CMS-PAS-SUS-12-030** (2013).

- [58] CMS Collaboration, “Reinterpreting the results of the search for long-lived charged particles in the pMSSM and other BSM scenarios”, *CMS Physics Analysis Summary CMS-PAS-EXO-13-006* (2014).
- [59] CMS Collaboration, “Search for disappearing tracks in proton-proton collisions at  $\sqrt{s} = 8$  TeV”, *Public CMS Wiki* (2015).  
<https://twiki.cern.ch/twiki/bin/view/CMSPublic/PhysicsResultsEXO12034>, Topic revision: r9.
- [60] CMS Collaboration, “Search for heavy long-lived charged particles in  $pp$  collisions at  $\sqrt{s} = 7$  TeV”, *Phys. Lett. B* **713** (2012) 408–433, [arXiv:1205.0272](#).  
[doi:10.1016/j.physletb.2012.06.023](#).
- [61] CMS Collaboration, “Description and performance of track and primary-vertex reconstruction with the CMS tracker”, *JINST* **9** (2014), no. 10, P10009,  
[arXiv:1405.6569](#). [doi:10.1088/1748-0221/9/10/P10009](#).
- [62] H. Bethe, “Theory of the Passage of Fast Corpuscular Rays Through Matter”, *Annalen Phys.* **5** (1930) 325–400. [*Annalen Phys.* 397,325(1930)].  
[doi:10.1002/andp.19303970303](#).
- [63] “National Institute of Standards and Technology”.  
<http://physics.nist.gov/cgi-bin/Star/compos.pl?mode=text&matno=014>.  
Accessed: 2015-10-21.
- [64] L. Landau, “On the energy loss of fast particles by ionization”, *J. Phys.(USSR)* **8** (1944) 201–205.
- [65] H. Bichsel, “Straggling in Thin Silicon Detectors”, *Rev. Mod. Phys.* **60** (1988) 663–699. [doi:10.1103/RevModPhys.60.663](#).
- [66] L. Quertenmont, “Search for Heavy Stable Charged Particles with the CMS detector at the LHC”. PhD thesis, Louvain, U., 2010.  
<https://inspirehep.net/record/1088192/files/openfile.pdf>.
- [67] D. Kotlinski. personal communication.
- [68] T. W. Anderson, “On the Distribution of the Two-Sample Cramr-von Mises Criterion”, *The Annals of Mathematical Statistics* **33** (1962), no. 3, pp. 1148–1159.
- [69] F. James, “Statistical methods in experimental physics”. 2006.
- [70] CMS Collaboration, “Tracking and Vertexing Results from First Collisions”, *CMS Physics Analysis Summary CMS-PAS-TRK-10-001* (2010).



- [71] J. Alwall, R. Frederix, S. Frixione et al., “The automated computation of tree-level and next-to-leading order differential cross sections, and their matching to parton shower simulations”, *JHEP* **07** (2014) 079, [arXiv:1405.0301](#).  
[doi:10.1007/JHEP07\(2014\)079](#).
- [72] T. Sjostrand, S. Mrenna, and P. Z. Skands, “PYTHIA 6.4 Physics and Manual”, *JHEP* **05** (2006) 026, [arXiv:hep-ph/0603175](#).  
[doi:10.1088/1126-6708/2006/05/026](#).
- [73] GEANT4 Collaboration, “GEANT4: A Simulation toolkit”, *Nucl. Instrum. Meth.* **A506** (2003) 250–303. [doi:10.1016/S0168-9002\(03\)01368-8](#).
- [74] J. Allison et al., “Geant4 developments and applications”, *IEEE Trans. Nucl. Sci.* **53** (2006) 270. [doi:10.1109/TNS.2006.869826](#).
- [75] R. Gavin et al., “FEWZ 3.1: A User’s Guide”.  
[http://www.hep.anl.gov/fpetriello/FEWZManual\\_3.1.pdf](http://www.hep.anl.gov/fpetriello/FEWZManual_3.1.pdf). Accessed: 2015-10-27.
- [76] M. Czakon, P. Fiedler, and A. Mitov, “Total Top-Quark Pair-Production Cross Section at Hadron Colliders Through  $O(\frac{4}{3})$ ”, *Phys. Rev. Lett.* **110** (2013) 252004, [arXiv:1303.6254](#). [doi:10.1103/PhysRevLett.110.252004](#).
- [77] B. Fuks, M. Klasen, D. R. Lamprea et al., “Gaugino production in proton-proton collisions at a center-of-mass energy of 8 TeV”, *JHEP* **1210** (2012) 081, [arXiv:1207.2159](#). [doi:10.1007/JHEP10\(2012\)081](#).
- [78] B. Fuks, M. Klasen, D. R. Lamprea et al., “Precision predictions for electroweak superpartner production at hadron colliders with Resummino”, *Eur.Phys.J.* **C73** (2013) 2480, [arXiv:1304.0790](#). [doi:10.1140/epjc/s10052-013-2480-0](#).
- [79] J. D. Brinson, “A search for disappearing tracks in proton-proton collisions at  $\sqrt{s} = 8$  TeV”. PhD thesis, Ohio State U.  
<https://inspirehep.net/record/1381347/files/CERN-THESIS-2015-030.pdf>.
- [80] J. Brinson, C. Hill, and W. Wulsin, “Search for disappearing tracks”, *CMS Analysis Note CMS-AN-12-400* (2014). Internal documentation.
- [81] CMS Collaboration, “Tracking and Primary Vertex Results in First 7 TeV Collisions”, *CMS Physics Analysis Summary CMS-PAS-TRK-10-005* (2010).
- [82] A. Bhatti et. al., “Search for New Physics in the Monojet final state at CMS”, *CMS Analysis Note CMS-AN-12-421* (2012). Internal documentation.

- [83] CMS Collaboration, “Search for dark matter, extra dimensions, and unparticles in monojet events in protonproton collisions at  $\sqrt{s} = 8$  TeV”, *Eur. Phys. J.* **C75** (2015), no. 5, 235, [arXiv:1408.3583](#). doi:10.1140/epjc/s10052-015-3451-4.
- [84] CMS Collaboration, “Studies of Tracker Material”, *CMS Physics Analysis Summary CMS-PAS-TRK-10-003* (2010).
- [85] CMS Collaboration, “Measurement of Higgs boson production and properties in the WW decay channel with leptonic final states”, *JHEP* **01** (2014) 096, [arXiv:1312.1129](#). doi:10.1007/JHEP01(2014)096.
- [86] CMS Collaboration, “Performance of Electron Reconstruction and Selection with the CMS Detector in Proton-Proton Collisions at  $s = 8$  TeV”, *JINST* **10** (2015), no. 06, P06005, [arXiv:1502.02701](#). doi:10.1088/1748-0221/10/06/P06005.
- [87] CMS Collaboration, “Performance of CMS muon reconstruction in  $pp$  collision events at  $\sqrt{s} = 7$  TeV”, *JINST* **7** (2012) P10002, [arXiv:1206.4071](#). doi:10.1088/1748-0221/7/10/P10002.
- [88] CMS Collaboration, “Performance of tau-lepton reconstruction and identification in CMS”, *JINST* **7** (2012) P01001, [arXiv:1109.6034](#). doi:10.1088/1748-0221/7/01/P01001.
- [89] J. Neyman *Phil. Trans. Royal Soc. London, Series A* **236** (1937) 333–80. Reprinted in *A Selection of Early Statistical Papers on J. Neyman* (University of California Press, Berkeley, 1967).
- [90] CMS Collaboration, “CMS Luminosity Based on Pixel Cluster Counting - Summer 2013 Update”, *CMS Physics Analysis Summary CMS-PAS-LUM-13-001* (2013).
- [91] D. Barge et. al., “Hadronic Recoil Studies of Heavy Boosted Systems”, *CMS Analysis Note CMS-AN-13-059* (2013). Internal documentation.
- [92] J. Pumplin, D. R. Stump, J. Huston et al., “New generation of parton distributions with uncertainties from global QCD analysis”, *JHEP* **07** (2002) 012, [arXiv:hep-ph/0201195](#). doi:10.1088/1126-6708/2002/07/012.
- [93] M. Botje et al., “The PDF4LHC Working Group Interim Recommendations”, [arXiv:1101.0538](#).
- [94] A. Vicini, “Practical implementation of the PDF4LHC recipe”. [http://www.hep.ucl.ac.uk/pdf4lh/PDF4LHC\\_practical\\_guide.pdf](http://www.hep.ucl.ac.uk/pdf4lh/PDF4LHC_practical_guide.pdf). Accessed: 2015-11-27.

- [95] CMS Collaboration, “Pileup Reweighting Utilities”, *Internal CMS Wiki* (2012).  
<https://twiki.cern.ch/twiki/bin/viewauth/CMS/PileupMCReweightingUtilities>,  
Topic revision: r29.
- [96] CMS Collaboration, “Estimating Systematic Errors Due to Pileup Modeling”,  
*Internal CMS Wiki* (2013).  
<https://twiki.cern.ch/twiki/bin/view/CMS/PileupSystematicErrors>, Topic  
revision: r11.
- [97] L. Quertenmont et al., “Searches for Heavy Stable Charged Particles with  
Combined 2011 and 2012 Datasets”, *CMS Analysis Note CMS-AN-12-293*  
(2013). Internal documentation.
- [98] J. Ott, “Search for Resonant Top Quark Pair Production in the Muon+Jets  
Channel with the CMS Detector”. PhD thesis, Hamburg U., 2013.  
[https://inspirehep.net/record/1296889/files/TS2013\\_046.pdf](https://inspirehep.net/record/1296889/files/TS2013_046.pdf).
- [99] T. Junk, “Confidence level computation for combining searches with small  
statistics”, *Nucl. Instrum. Meth.* **A434** (1999) 435–443, [arXiv:hep-ex/9902006](https://arxiv.org/abs/hep-ex/9902006).  
[doi:10.1016/S0168-9002\(99\)00498-2](https://doi.org/10.1016/S0168-9002(99)00498-2).
- [100] A. L. Read, “Modified frequentist analysis of search results (The CL(s) method)”,  
in *Workshop on confidence limits, CERN, Geneva, Switzerland, 17-18 Jan 2000:*  
*Proceedings*. 2000.
- [101] A. L. Read, “Presentation of search results: The CL(s) technique”, *J. Phys.* **G28**  
(2002) 2693–2704. [11(2002)]. [doi:10.1088/0954-3899/28/10/313](https://doi.org/10.1088/0954-3899/28/10/313).
- [102] CMS and ATLAS Collaborations, “Procedure for the LHC Higgs boson search  
combination in summer 2011”, *Technical Report* (2011). CMS-NOTE-2011-005,  
ATL-PHYS-PUB-2011-011.
- [103] CMS Collaboration, “Documentation of the RooStats-based statistics tools for  
Higgs PAG”, *Internal CMS Wiki* (2015).  
<https://twiki.cern.ch/twiki/bin/viewauth/CMS/SWGuideHiggsAnalysisCombinedLimit>,  
Topic rev: r124.
- [104] C. H. Chen, M. Drees, and J. F. Gunion, “Addendum/erratum for ‘searching for  
invisible and almost invisible particles at  $e^+e^-$  colliders’ [hep-ph/9512230] and ‘a  
nonstandard string/SUSY scenario and its phenomenological implications’  
[hep-ph/9607421]”, [arXiv:hep-ph/9902309](https://arxiv.org/abs/hep-ph/9902309).



